PolyPublie
Polytechnique Montréal

POLYTECHNIQUE MONTRÉAL
UNIVERSITÉ D'INGÉNIERIE

| | |
|---|---|
| **Titre:** Title: | Implementations of optical coherence tomography |
| **Auteur:** Author: | Zhiqiang Xu |
| **Date:** | 2003 |
| **Type:** | Mémoire ou thèse / Dissertation or Thesis |
| **Référence:** Citation: | Xu, Z. (2003). Implementations of optical coherence tomography [Mémoire de maîtrise, École Polytechnique de Montréal]. PolyPublie. https://publications.polymtl.ca/7159/ |

**Document en libre accès dans PolyPublie**
Open Access document in PolyPublie

| | |
|---|---|
| **URL de PolyPublie:** PolyPublie URL: | https://publications.polymtl.ca/7159/ |
| **Directeurs de recherche:** Advisors: | Romain Maciejko |
| **Programme:** Program: | Non spécifié |

**Ce fichier a été téléchargé à partir de PolyPublie, le dépôt institutionnel de Polytechnique Montréal**
This file has been downloaded from PolyPublie, the institutional repository of Polytechnique Montréal

https://publications.polymtl.ca

In compliance with the
Canadian Privacy Legislation
some supporting forms
may have been removed from
this dissertation.

While these forms may be included
in the document page count,
their removal does not represent
any loss of content from the dissertation.

UNIVERSITÉ DE MONTRÉAL

# IMPLEMENTATIONS OF OPTICAL COHERENCE TOMOGRAPHY

ZHIQIANG XU

DÉPARTEMENT DE GÉNIE PHYSIQUE

ÉCOLE POLYTECHNIQUE DE MONTRÉAL

MÉMOIRE PRÉSENTÉ EN VUE DE L'OBTENTION

DU DIPLÔME DE MAÎTRISE ÈS SCIENCES APPLIQUÉES

(GÉNIE PHYSIQUE)

OCTOBRE 2003

© ZHIQIANG XU, 2003

National Library
of Canada

Acquisitions and
Bibliographic Services

395 Wellington Street
Ottawa ON K1A 0N4
Canada

Bibliothèque nationale
du Canada

Acquisisitons et
services bibliographiques

395, rue Wellington
Ottawa ON K1A 0N4
Canada

*Your file Votre référence*
*ISBN: 0-612-86437-5*
*Our file Notre référence*
*ISBN: 0-612-86437-5*

The author has granted a non-exclusive licence allowing the National Library of Canada to reproduce, loan, distribute or sell copies of this thesis in microform, paper or electronic formats.

The author retains ownership of the copyright in this thesis. Neither the thesis nor substantial extracts from it may be printed or otherwise reproduced without the author's permission.

L'auteur a accordé une licence non exclusive permettant à la Bibliothèque nationale du Canada de reproduire, prêter, distribuer ou vendre des copies de cette thèse sous la forme de microfiche/film, de reproduction sur papier ou sur format électronique.

L'auteur conserve la propriété du droit d'auteur qui protège cette thèse. Ni la thèse ni des extraits substantiels de celle-ci ne doivent être imprimés ou aturement reproduits sans son autorisation.

Canada

UNIVERSITÉ DE MONTRÉAL

ÉCOLE POLYTECHNIQUE DE MONTRÉAL

Ce mémoire intitulé :

IMPLEMENTATIONS OF OPTICAL

COHERENCE TOMOGRAPHY

présenté par : XU Zhiqiang

en vue de l'obtention du diplôme de : Maîtrise ès sciences appliquées

a été dûment accepté par le jury d'examen constitué de :

M. FAUCHER Guy, D. Sc., président

M. MACIEJKO Romain, Ph. D., membre et directeur de recherche

M. BERTRAND Michel, Ph. D., membre

To my parents

## ACKNOWLEDGEMENTS

This thesis could not have been completed without much help from many people. First, I wish to express my thanks and consideration to my thesis supervisor Professor Romain Maciejko. He accepted me as his student for my graduate studies at École Polytechnique. He also provided me with a very good project for my research in the Optoelectronic Laboratory. I want to say that without his patient advice and kind encouragement through the past three years, it would have not been possible for me to accomplish this much.

I also wish to give my thanks to Mr. Michel Lestrade, who wrote the data acquisition and scanning control program and gave me a great deal of help on computers and other apparatus. Mr. Lionel Carrion collaborated with me on the white LED tomography and we had many useful discussions that have helped me with the thesis. Mr. Souleymane Bah provided some samples. Mr. Jimmy Rheault, Mrs. Rodica Matei, and Mr. François Barrette helped me to assemble the components of my experimental setup.

It is a great pleasure to have the opportunity to study in such a wonderful environment and colleagues during the first four years since I came to Canada. It is a great country with great people.

Finally, I would like to say thanks to my parents, my wife and my son for their constant support and love.

# RÉSUMÉ

La tomographie en optique cohérente (TOC) est une technique d'imagerie qui a vu le jour assez récemment (il y a environ une dizaine d'années). Cette méthode non destructive basée sur les interférences d'une source faiblement cohérente permet d'obtenir des profils à haute résolution de structures enfouies dans des tissus biologiques ou dans des matériaux non biologiques. La TOC est particulièrement adaptée pour des applications de recherche ou de contrôle dans des processus de fabrication, ou encore dans des applications médicales (par exemple, la détection de maladies de l'oeil ou de la formation de tumeurs cancéreuses).

Jusqu'alors, la plupart des travaux de TOC ont été réalisés avec deux types de sources lumineuses faiblement cohérentes : d'une part, les lasers à impulsions ultra-brèves, et d'autre part, les semi-conducteurs émetteurs dans l'infrarouge. Dans un premier temps, un laser Titane Saphir femtoseconde déjà disponible au laboratoire a été préparé en vue d'expériences futures. Ce laser fonctionnant grâce à une technique de blocage de modes a été considérablement modifié à l'aide de calculs détaillés. Il génère présentement des impulsions très stables en énergie et facilement mises en route, d'une durée de 71 femtosecondes et d'une largeur spectrale à mi-hauteur de 46 nm. La longueur de cohérence d'un tel laser a été mesurée et est égale à 6.1 μm, ce qui en fait une source particulièrement adaptée pour des applications TOC. Cependant nous avons préféré travailler dans un premier temps avec des longueurs de cohérence plus grandes afin de faciliter les premiers réglages et la calibration de l'interféromètre. Une source à semi-conducteur large bande commercialisée par JDSU a donc été choisie comme solution intermédiaire pour les premières expériences de TOC.

Un interféromètre de Michelson a été construit et aligné avec cette source, et deux platines de translation linéaires contrôlées par ordinateur ont été utilisées pour le balayage longitudinal du miroir de référence et le balayage latéral de l'objet. Un programme pour l'acquisition de données, le traitement du signal et le contrôle simultané du balayage a été développé. Ce système a été essayé avec succès en utilisant un miroir pour objet. Les mesures donnent un rapport signal sur bruit de 41.3 dB ainsi qu'une longueur de cohérence de 32.3 μm. Un objectif de microscope ayant une ouverture numérique de 0.25 a été utilisé pour focaliser le faisceau sur l'échantillon. Ainsi la taille du spot, qui correspond à la résolution du système, est de 10 μm et la profondeur du balayage axial est de 850 μm. Quatre échantillons ont été étudiés et des images TOC ont été obtenues à partir de ce système.

Enfin, une nouvelle approche TOC a été proposée et un nouveau montage expérimental a été réalisé avec une LED blanche utilisée comme source. Il s'est avéré que cette source est beaucoup plus stable (aussi bien en intensité qu'en spectre) et qu'elle apporte également une meilleure résolution. De même, celle-ci possède une durée de vie beaucoup plus longue. Enfin il est plus facile de la contrôler. Les franges d'interférences obtenues révèlent un effet arc-en-ciel relié à la dispersion du système d'une part, et à l'état de polarisation de la lumière d'autre part. Ce problème a été résolu. Cinq échantillons ont été étudiés afin d'obtenir des profils TOC : une résolution axiale de 1.6 μm a été obtenue pour un échantillon de mica. Ce résultat est comparable aux meilleurs résultats publiés jusqu'ici.

## ABSTRACT

Optical Coherence Tomography (OCT) is a relatively recent imaging technology (approximately 10 years old) which allows high resolution, noninvasive cross-sectional tomographic imaging of internal structures in biological tissues and non-biological materials based on low-coherence interferometry. OCT is suitable for research, manufacturing, or clinical applications, i.e., the detection of some eye diseases and early cancer.

So far, most OCT implementations have been done with respect to two major options for the broadband sources, either an ultra-short pulse laser or an infrared semiconductor light emitter. As part of the OCT project, an existing Ti:Sapphire femtosecond pulse laser has been prepared for future experiments. The mode-locked Ti:Sapphire laser was redesigned substantially using detailed calculations and was eventually made to operate with 71 femtosecond pulses and a 46 nm FWHM bandwidth with a high stability and easy firing up. The coherence length of such a source was found to be about 6.1 μm but it was judged more appropriate to relax the bandwidth constraint for the preliminary interferometer setup and caliberation procedure and a commercial semiconductor broadband source from JDSU was chosen instead as an intermediate solution for the first OCT experiments.

A free-space Michelson interferometer was built and aligned with this source, and two computer-controlled linear positioners were employed for the longitudinal scanning of the reference mirror and the lateral scanning of the object. An in-house data acquisition and

scanning control program was developed for signal processing. The system was successfully tested using a mirror as the object. The signal-to-noise ratio was measured to be in the 41.3 dB range with a measured coherence length of 32.3 μm. A NA=0.25 microscope objective was employed to focus the beam onto the sample which lead to a spot size of about 10 μm (the lateral resolution of the system) and an axial scanning depth of 850 μm. Four objects have been scanned and the OCT images have been obtained with this setup.

A novel approach to OCT was proposed and a new experimental setup was built using a white LED as the light source. This source was found to be more stable (both in intensity and spectrum), to have a higher resolution, a much longer lasting time, and to be monitored more easily. The interference fringes showed a rainbow effect that was related to the dispersion of the system and the polarization state of the light beam. This problem has been resolved. Five objects have been scanned in order to obtain the OCT cross-sectional images, and an axial resolution of 1.6 μm has been achieved for a mica sample which compares favorably with the best results published so far.

# CONDENSÉ EN FRANÇAIS

Un système de tomographie en optique cohérence (TOC) se compose de trois parties principales: une source à bande large, un montage optique et un système électrique. Chacun d'eux a été analysé et optimisé dans cette thèse. À la différence de la plupart des travaux expérimentaux de la TOC effectués dans la région infrarouge proche, nous avons proposé pour la première fois une nouvelle réalisation expérimentale de la TOC avec d'excellents résultats dans la région visible du spectre. Des phénomènes expérimentaux tels que l'état de polarisation, la dispersion, les franges d'interférence et l'effet de filtre peuvent être facilement observés et étudiés à l'œil nu.

On sait que la résolution d'un système de TOC est déterminée par la longueur de cohérence de la source à large bande. Cette conclusion a été obtenue en analysant les propriétés d'interférence de beaucoup de sources lumineuses. Le lien entre le spectre de la source et l'interférogramme est une transformée de Fourier de sorte que sa longueur de cohérence est proportionnelle à la longueur d'onde centrale mais inversement proportionnelle à la largeur de bande. Beaucoup de sources analysées sont baséer sur cette idée.

Le compromis à faire entre la résolution latérale et la profondeur du balayage axial du système de TOC a été étudié. On constate que le choix de l'ouverture numérique (NA) de l'objectif du microscope à l'intérieur du chemin optique détermine la taille de la tache du faisceau sonde focalisé et sa profondeur de champ. On peut choisir la résolution latérale du système en changeant l'ouverture numérique de l'objectif du microscope. Cependant, la

résolution longitudinale du TOC est déterminée par la longueur de cohérence de la source et n'est pas vraiment reliée aux composants optiques du système.

Un laser à impulsions femtosecondes Ti:Saphir a été mis à niveau comme source alternative des expériences de TOC. L'astigmatisme induit dans la cavité laser par le cristal Ti:Saphir à angle de Brewster a été bien compensé et les caractéristiques de la lentille par effet Kerr et du blocage de modes ont été considérées quand la nouvelle cavité laser a été conçue. La dispersion de la vitesse de groupe dans la cavité a été estimée théoriquement. En choisissant soigneusement les paramètres des composants, la dispersion minimum à l'intérieur de la cavité a été obtenue. Une nouvelle méthode matricielle de simulation a été développée pour optimiser la cavité d'un laser Ti:Saphir à impulsions femtosecondes. Ainsi nous avons pu trouver la région de stabilité de la cavité et les positions des différents composants ont été corrigées pour un bon fonctionnement en modes bloqués et une mise en route du laser aisée.

Un système d'acquisition de données et de commande balayage a été développé comme partie électrique du système de TOC. Dans ce programme, beaucoup de fonctions peuvent être réglées, comme par exemple les vitesses, les pas, et les domaines du balayage longitudinal du miroir de référence et du balayage latéral de l'échantillon; les tracés et les affichages des données de modulation d'intensité fournis par le détecteur photoélectrique; le traitement des données à l'aide d'un filtre passe-bas et une transformée mathématique pour produire l'enveloppe des données d'entrée. Les signaux d'interférence enregistrés comprennent les positions, les intensités, et l'information sur la résolution des interfaces de l'échantillon. Les images finales en coupe peuvent être obtenues à partir des données

d'enveloppe d'une série de balayages. Une taille typique d'image comprend 50 × 5000 Pixels. La séparation entre deux tracés longitudinaux est déterminée par la résolution latérale du montage expérimental, c'est-à-dire par la taille de la tache focale du faisceau sonde.

Nous avons également conçu et testé un système de TOC basé sur une diode supraluminescente (SLD) à large spectre infrarouge disponible dans le commerce. Celle-ci a une longueur de cohérence de 32.3 μm. Nous avons montré que les états de polarisation des faisceaux qui interfèrent dans ce système n'ont qu'une influence limitée sur les signaux d'interférence reçus, et que ce système est particulièrement adapté pour l'étude d'échantillons ayant des structures d'une taille supérieure à 50 μm, comme, par exemple, les cellules végétales. La résolution axiale du système TOC a été de beaucoup améliorée en remplaçant la source SLD par une DEL blanche de longueur de cohérence beaucoup plus faible (inférieure à 2 μm). Comparativement à d'autres sources utilisées jusqu'ici en TOC, les premières études effectuées avec la source LED blanche à large spectre ont donné d'excellents résultats. Ces nouvelles sources jouissent de plusieurs avantages: elles possèdent un spectre très étendu dans le visible et sont très peu absorbées par les tissus, ce qui les rend particulièrement attrayantes pour des applications TOC à très haute résolution. De plus, celles-ci sont compactes et peu coûteuses, faciles à utiliser, ont une durée de vie assez élevée, et produisent un faisceau de lumière stable et de haute puissance. Les images en coupe de TOC produites par cette LED blanche source ont déjà atteint une résolution axiale de 1.6 μm, ce qui est très proche du meilleur résultat obtenu jusqu'ici (1.1 μm). Nous avons comparé les images en coupe d'un échantillon de mica obtenues avec ces deux sources: les coupes obtenues avec la DEL blanche présentent des structures beaucoup plus

résolues.

Un système de collimation à faibles pertes a été spécialement conçu pour la source étendue (DEL blanche). Grâce à ce système nous avons obtenu un faisceau parallèle et uniforme de bonne puissance pour l'étude des échantillons en TOC. L'influence des franges d'interférence induites par la focalisation de ce faisceau sur les échantillons a été corrigée par une compensation des chemins optiques entre le faisceau de référence et le faisceau sonde. Par conséquent, nous avons pu observer une figure d'interférence composée de plusieurs anneaux colorés d'ordre inférieur.

# TABLE OF CONTENTS

# LIST OF FIGURES

# LIST OF ABBREVIATIONS

| | |
|---|---|
| OCT | Optical Coherence Tomography |
| NA | Numerical Aperture |
| OCDR | Optical Coherence-Domain Reflectometry |
| OH | Oxyhydrogen |
| BS | Beamsplitter |
| SLD | Superluminescent Diode |
| FWHM | Full-Width at Half-Maximum |
| TV | Television |
| OC | Output Coupler |
| CW | Continuous Wave |
| GVD | Group Velocity Dispersion |
| TOD | Third-Order Dispersion |
| FT | Fourier Transformation |
| LED | Light-Emitting Diode |
| LIOB | Laser Induced Optical Breakdown |
| SHG | Second Harmonic Generation |

# CHAPTER 1

# INTRODUCTION

## 1.1 The principle of Optical Coherence Tomography

Optical coherence tomography (OCT) is a fundamentally new imaging technique. It performs micrometer-scale resolution imaging of biological tissue by measuring the echo time delay and intensity of backscattered or backreflected light from the sample. This method, being analogous to B-mode ultrasonic pulse-echo imaging that is widely used in clinical applications, is an extension of the low-coherence reflectometry technique. In low coherence reflectometry, the coherence property of the reflected light contains time-of–flight information that can be used to determine the longitudinal locations of reflective boundaries and backscattering sites in the sample. The OCT system performs a series of longitudinal scans at different lateral locations in order to create a two-dimensional map of reflection sites in the sample.

Therefore, a low-coherence light source, a Michelson interferometer and the beam scanning optics are the main components of a real OCT setup. Fig. 1.1 (a) shows a schematic diagram of an OCT setup. The incident broadband light source is directed onto a beamsplitter that splits this broadband light beam into a reference beam $E_R$ (t) and a sample beam $E_S$ (t). The reference beam $E_R$ (t) is blocked and reflected by a reference mirror in order to provide the reference position information. The sample beam $E_S$ (t) illuminates the biological specimen that needs to be imaged. The reflected sample and reference beams

interfere at the beamsplitter. Therefore, the output of the interferometer is the sum of the electromagnetic fields of these two reflected beams. If the lengths of the reference arm and the sample arm are $L_R$ and $L_S$, respectively, the optical path difference is then:

$$\Delta L = L_R - L_S, \tag{1-1}$$

And the intensity of the interference signal is [1]:

$$I_0(t) = \frac{E_R^2}{2} + \frac{E_S^2}{2} + E_R E_S \cos\left(2\frac{2\pi}{\lambda}\Delta L\right) \tag{1-2}$$

When the light source is coherent (a laser for example), the observed interferometer output will vary over a wide range of $\Delta L$. The variation of $\Delta L$ is carried out by translating the reference mirror along the optical axis of the reference arm. This is shown schematically in Fig.1.1 (b). However, if a low-coherence light is used, the interference signal can be observed only when the optical path lengths of the reference and sample arms are matched to within the coherence length of the source ($L_c$), as Fig.1.1 (c) shows. In this situation, the longitudinal scan is achieved during translating the reference mirror along the optical axis of the reference arm of the system until the path delay matched position is reached. The interferometric signal appears only within a very limited range determined by the coherence length of the light source $L_c$. By measuring the field autocorrelation of the light, the echo time delay and the magnitude of the reflected light can be determined. The former consists of the position information of the internal structures of the tissue sample, and the latter gives us their reflecting intensity. This information provides an axial image of the sample within this sample beam.

It is the coherence length of the low-coherence light $L_c$ that determines the resolution of the axial position. So far, axial resolutions of 1 μm have been obtained by means of an ultra-short pulse Ti: Sapphire laser which generates a pulse duration of 5 fs and bandwidths of over 300 nm [2].

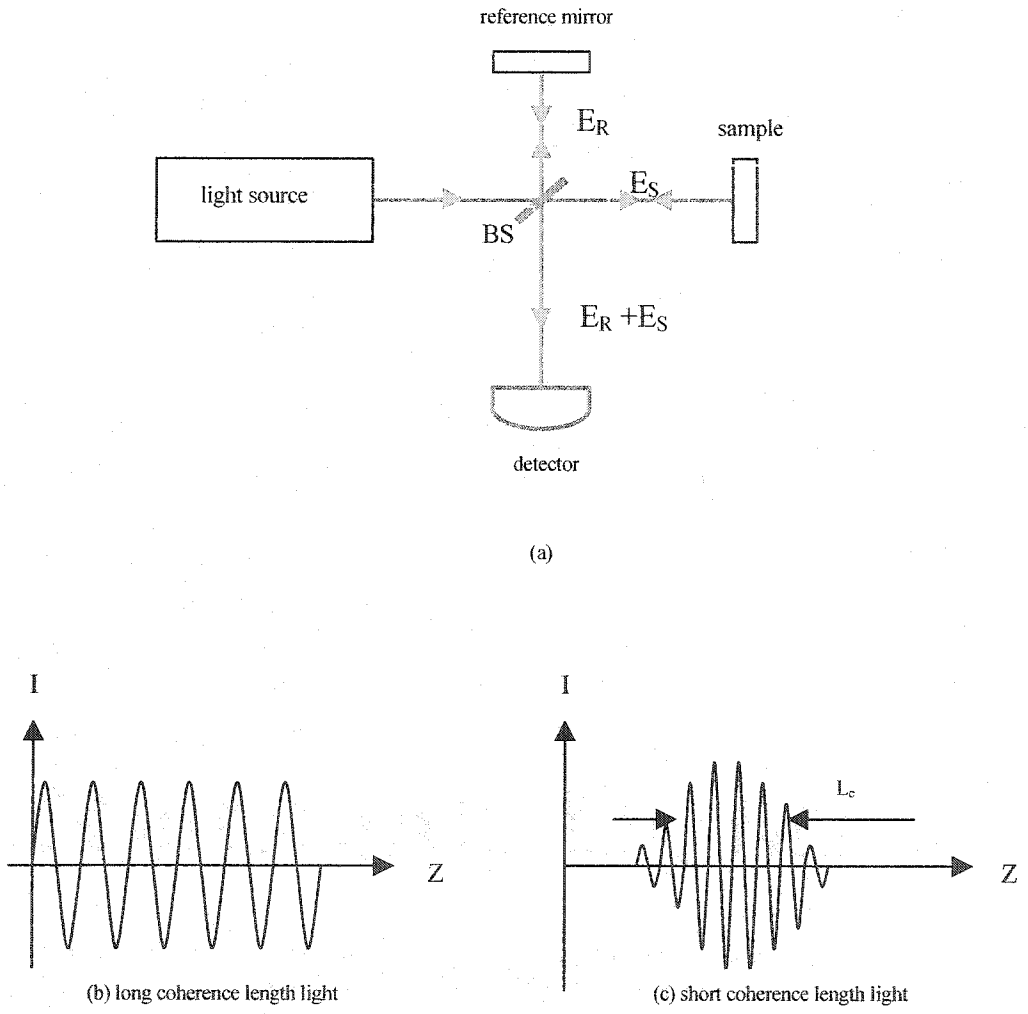


**Figure 1.1** A schematic diagram of a standard OCT setup

## 1.2 The coherence length of the light source

Unlike the conventional microscopy imaging systems whose axial resolution of the image depends on the beam-focusing conditions, OCT has only the coherence length of the light source $L_c$ to determine its axial resolution. Therefore, the coherence length of a light source becomes one of the most important parameters for estimating if the OCT system can perform high-resolution imaging.

In Fig. 1.1(a), the beamsplitter divides the broadband source field E into a reference field $E_R$ and sample field $E_S$. After being backreflected or backscattered from the various constituents of the sample, the modified sample field $E_S'$ interferes with the reference field $E_R$. The received intensity I can be expressed as [3-4]:

$$I = \left\langle |E|^2 \right\rangle = 0.5(I_R + I_S) + Re\left\{\left\langle E_R^*(t+\tau)E_S'(t)\right\rangle\right\} \qquad (1\text{-}3)$$

where $I_R$ and $I_S$ are the mean intensities of the reference and sample arms of the interferometer, respectively. Both of them contribute nothing to the interference properties of the system. The interference properties of the system are only affected by the second term in this equation, the interference term. The interference fringes that carry information about the tissue structure come from the interference term. The optical time delay $\tau$ is given by the position of the reference mirror.

The interference term contains information on how much the temporal and spatial characteristics of $E_S'$ and $E_R$ match. The amplitude of the interference signal generated

within the detector corresponds to the cross-correlation of the interference term:

$$Re\left\{\left\langle E_R^*(t+\tau)E_S'(t)\right\rangle\right\} = \left|G(\tau)\cos[2\pi\nu_0\tau + \varphi(\tau)]\right| \qquad (1\text{-}4)$$

where c is the speed of light, $\nu_0$ is the center frequency of the source, and $G(\tau)$ is the complex temporal-coherence function with argument $\phi(\tau)$ [2][3][4]:

$$G(\tau) = \int_0^\infty S(\nu)\exp(-j2\pi\tau)d\nu \qquad (1\text{-}5)$$

S ($\nu$) is the power spectral density of the source.

We assume that there is no spectral modulation in the reflectivity of both the sample and reference arms, and the light source has a Gaussian power spectral density given by

$$S(\nu) = \frac{2\sqrt{\ln 2/\pi}}{\Delta\nu}\exp\left[-4\ln 2\left(\frac{\nu-\nu_0}{\Delta\nu}\right)^2\right] \qquad (1\text{-}6)$$

where $\Delta\nu$ is the half-power bandwidth. It follows from this equation that the interference term $G(\tau)$ is also a Gaussian shape represented by

$$G(\tau) = \exp\left[-\left(\frac{\pi\Delta\nu\tau}{2\sqrt{\ln 2}}\right)^2\right]\exp(-j2\pi\nu_0\tau) \qquad (1\text{-}7)$$

Thus, for the interferometer in free space, the coherence length of the partially coherent source $L_C$ can be obtained as

$$L_C = \frac{2c\ln 2}{\pi}\cdot\frac{1}{\Delta\nu} = \frac{2\ln 2}{\pi}\cdot\frac{\lambda_0^2}{\Delta\lambda} \approx 0.44\times\frac{\lambda_0^2}{\Delta\lambda} \qquad (1\text{-}8)$$

where $\Delta\lambda$ is the full-width of the coherence function at half-maximum (FWHM) in wavelength units and $\lambda_0$ is the center wavelength.

## 1.3 Depth limit

The transverse resolution of optical coherence tomography imaging is determined by the size of the focusing spot inside the sample. This is the same as in conventional optical microscopy. The smaller the beam focusing spot size is, the higher lateral resolution the OCT system will reach. However, the minimum spot size to which an optical beam can be focused is linked to the coherence length of the source.

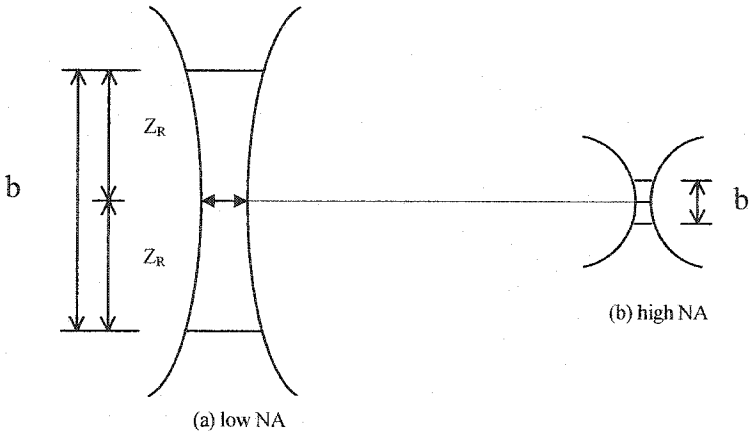


**Figure 1.2** A focusing beam shape by low and high numerical aperture (NA)

Fig.1.2 is a focusing beam shape created by low and high numerical aperture (NA) microscope objectives. The focused spot size of a beam is inversely proportional to the numerical aperture of the focusing lens, as well as the depth of focus [5].

$$\Delta x = \frac{4\lambda}{\pi}\left(\frac{f}{d}\right) \qquad (1\text{-}9)$$

where d is the spot size on the focusing lens, Δx is the focal spot size, and f is the focal

length. Large numerical aperture results in a high resolution or a small focal spot. The depth of focus is defined by two times of Rayleigh range of the focused beam, which is expressed as:

$$b = 2Z_R = \frac{\pi \Delta x^2}{2\lambda} \qquad (1\text{-}10)$$

this means the depth of focus decreases when the focal spot is small or a large numerical aperture is employed. Once the depth of focus is close to the coherence length of the source, the axial resolution of the system will not be related to the coherence length of the source any more. This means that the minimum focusing spot size of the sample beam is limited by the coherence length of the light source.

In fact, most OCT systems employ low numerical aperture scanning optics to enlarge its Rayleigh range rather than using high NA optics to narrow down the axial scanning range. High depth of focus is obtained at the expense of reduced transverse resolution.

## 1.4 Applications of Optical Coherence Tomography

OCT is a new imaging technology that produces high-resolution cross-sectional images of the internal microstructure of living tissue without the need to excise a specimen from it. It has many advantages including [5]:

(1). Imaging can be performed in situ (*in vivo*) and nondestructively.

(2). High longitudinal resolutions are possible with typical image resolutions of 10-15 μm and ultrahigh resolutions of down to 1 μm.

(3). High-speed real-time imaging is possible.

(4). OCT can be interfaced with a wide range of imaging delivery systems and imaging probes.

(5). OCT technology can be based on fiber optics and uses components developed for the telecommunications industry.

(6). Image information is generated in electronic form that is amenable to image processing and analysis as well as electronic transmission, storage, and retrieval.

(7). OCT systems can be engineered to be compact and low cost, suitable for research, manufacturing, or clinical applications.

The first OCT image of clinical usage was that of a human retina in 1991[6]. The first *in vivo* tomograms of the human optic disk and macula were demonstrated in 1993[7]. Because OCT has an extremely high sensitivity, it allows extremely small backscattering signals to be recognized even if the retina is almost transparent at the wavelength used. Indeed, OCT provides a cross-sectional view of the retina with a high resolution and allows detailed structures to be differentiated. Some materials, such as the retinal pigment epithelium and the choroid, are well recognized as highly scattering structures in the OCT image. The OCT image of the eye also has higher depth resolution than that can be obtained with clinical ultrasound systems. It provides a new technique to obtain a more detailed information on the contour and thickness of retinal structures that can be used as a new clinical diagnostic procedure. Optical coherence tomography, so far, has been used for the detection of some eye diseases, including macular edema, macular holes, central serous chorioretinopathy, age-related macular degeneration and choroidal neovascularization, and epiretinal membranes.

With recent research advances, OCT imaging can be done even in traditionally nontransparent tissues by the utilization of longer wavelength light. In most tissues, image penetration depths of 2-3 mm can be achieved at 1.3 μm wavelengths. This depth range is large enough to enable a new diagnostic technique, optical biopsy, in some situations where conventional excisional biopsy is not suitable. One example is the OCT imaging of atherosclerotic plaque morphology in the coronary arteries. These plaque morphologies that cause thrombosis and vessel occlusion are difficult to detect by conventional radiological techniques. The ability to identify structural details in the coronary arteries by OCT imaging could lead to significant improvements in patient outcome. Recent research uses

OCT imaging as a tool for the detection of early neoplasia. Most early neoplasias have shown the evidence of neoplastic changes by some disruption of the normal glandular organization or architectural morphology of tissues.

The ability to see beneath the surface of tissue in real time also enables OCT to guide surgery near sensitive structures such as vessels or nerves as well as assist in microsurgical procedures. An example of a surgical application is the repair of small vessels and nerves following traumatic injury.

# CHAPTER 2

# THE EXPERIMENTAL SETUP

## 2.1 Introduction

The fundamental principle, which OCT is based on, is imaging by measuring the echo time delay and intensity of backscattered or backreflected light by means of low-coherence interferometry technology. An interferometer is thus one of the most important components in all OCT setups. Although various kinds of interferometers, such as the Mach-Zehnder interferometer, have been introduced in OCT, the most common interferometer configuration employed in OCT systems so far is still the Michelson interferometer.

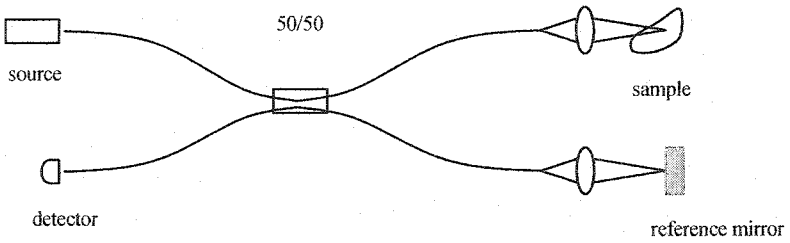


(a). Fiber-optic interferometer

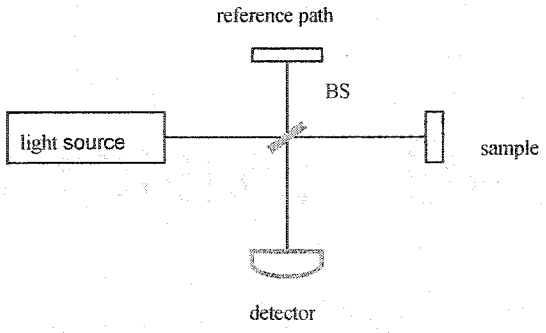


(b)Free-space interferometer

**Figure 2.1** Schematic diagram of two kinds of Michelson interferometers

Two popular kinds of Michelson interferometers (fiber-optic and free-space) are shown in Fig. 2.1 As illustrated in Fig.2.1 (a), a broadband light source is coupled into a single-mode fiber and directed through the fiber to a 50/50 coupler where half of the optical power is extracted by another single-mode fiber that conducts the light to the reference mirror. The other half of the optical power enters the sample through a single-mode fiber also. Reflected beams from the reference mirror and the sample are recombined at the coupler and the output is detected by the photodiode. Longitudinal scanning is performed by translating the reference mirror. The interference signal can be detected by the photo-detector when the reference and sample arm delays are matched within the coherence length of the source. By translating the lateral position of the sample after each longitudinal scan, a 2-D and 3-D cross-sectional tomographic image of the internal microstructure of the sample can be obtained.

OCT is a development based on the optical coherence-domain reflectometry (OCDR), normally used in the optical fiber system to locate faults in fiber-optic cables. A common interferometer configuration applied in OCT is optical-fiber based as illustrated in Fig. 2.2. In fact, the first OCT cross-sectional image of the human retina *in vivo* was realized by means of a fiber-optic Michelson interferometer in 1991 [6].

It is quite convenient to introduce fiber optics in the design of an OCT system based on compact fiber-optic components and integrated with a wide range of medical instruments. With optical fiber, one can make OCT probe as flexible miniature devices for internal body imaging. It is also possible to have the probe beam used in conjunction with a standard endoscope or bronchoscope for an *en face* view of the area to be scanned. Using fiber-

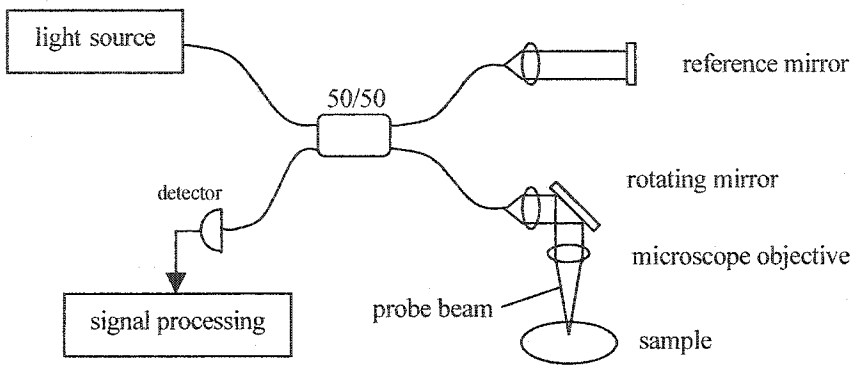


**Figure 2.2** The configuration of a standard fiber-optic Michelson interferometer

optics can simplify mode matching between the interferometer arms and suppress higher order mode backscattering from the sample. Single-mode fiber optics is preferred since it avoids multiple mode propagation inside the fiber which could severely degrade longitudinal resolution due to mode dispersion.

Although the use of fiber optics is convenient, great attention must be paid to some of the drawbacks introduced by the optical fiber. A few examples of these drawbacks are oxyhydrogen (OH) ion absorption in the silica, changes of the polarization of the beam induced by bending the fiber unless polarization maintaining is used and the power loss while coupling the light into and out of the optical fibers. These drawbacks are the reason why a much simpler system, the free-space interferometer illustrated in Fig. 2.1(b), is widely used in laboratories today. The advantage of this configuration is that optical components can be easily added into the arms to modify the optical system. This OCT implementation was chosen for the present work.

## 2.2 The experimental setup

A free-space Michelson interferometer has been built in the Optoelectronics Laboratory. The layout is shown in Fig. 2.3. A power beamsplitter (BS) cube (Newport Optics) is centered in front of a reference mirror which is fixed on a motor system. A microscope objective focuses the sample beam onto the sample and collects the backreflected or backscattered light into the system. Two quarter-wave plates (THORLABS INC.) are placed in the reference and sample arms for changing the polarization state of the optical beams by simple rotation. The source, a superluminescent

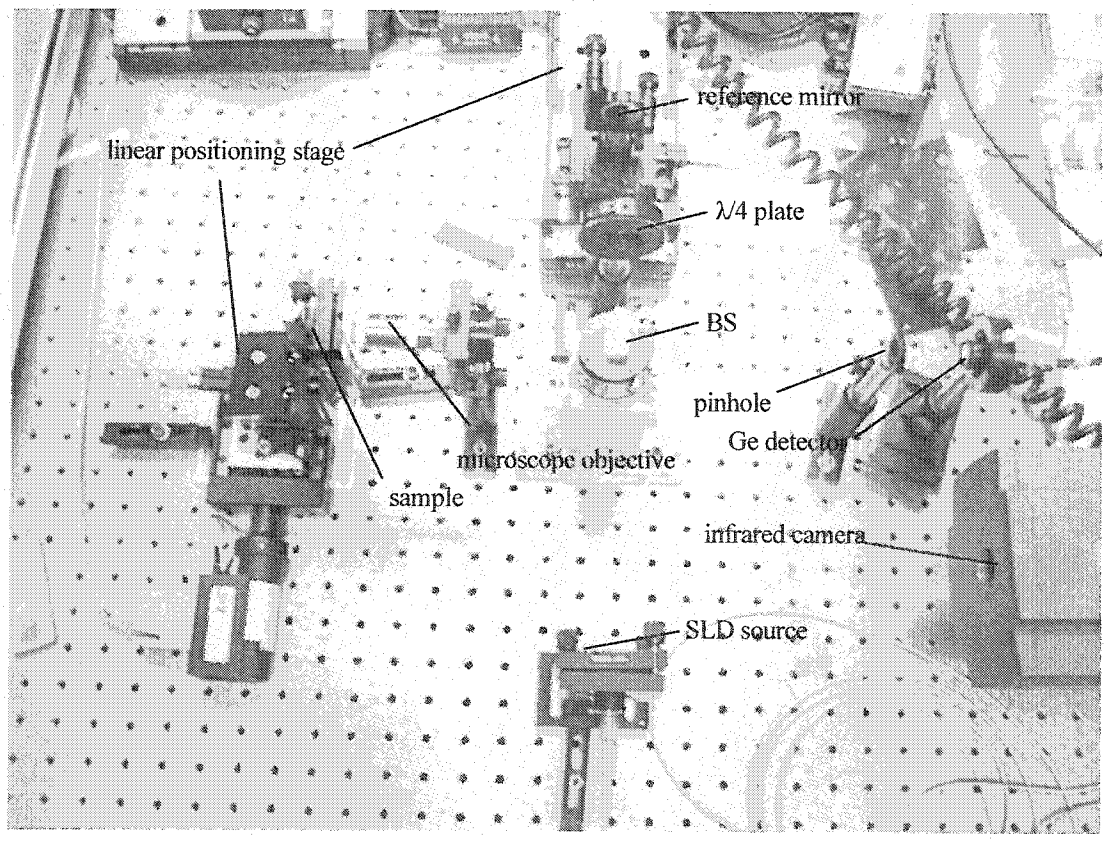


**Figure 2.3** Diagram of the OCT experimental setup

diode (SLD) (JDS Uniphase), emits 37 mW of optical power. The center wavelength of the source is 1545 nm and the full-width at half-maximum (FWHM) spectral bandwidth is 32 nm.

The SLD output light is collimated and divided into two equal intensity beams in the sample and reference arms by the beamsplitter. An infrared camera is used to monitor the interference signal on a TV monitor and a Ge photodetector is used to record the value of this signal. The reference mirror is mounted on a computer-controlled linear positioning stage (PI Physik Instrument) with a 150 mm scanning range at an adjustable moving speed which can be set from 0 to 1.5 mm/s.

The computer controls the two linear positioning stages by means of a data acquisition and scanning control program. This program allows 1-D or 2-D scanning of the sample and allows the user to set the scanning range and speed. A data logger (Agilent) was used to record the intensity modulation data read from the detector, at a rate of 60 frames per second. Every frame related to one point inside the recorded interference trace and a typical image size contains 50 x 5000 points.

The interference data is saved in Matlab files which consist of the position and intensity information of the internal structure of the sample. An envelope detection algorithm and a low-pass filter are needed to obtain the information and produce a 2-D contour map. The contrast and the resolution of the map can be adjusted by choosing different orders of the filter and the cutoff parameter.

## 2.3 The quality test of the OCT setup

When the experimental setup has been well aligned, a quality check needs to be done. We used a high reflectivity mirror as the sample for the test and measured the detection sensitivity and the longitudinal resolution of the OCT system. The light source was the SLD from JDS Uniphase. The calculated coherence length of this SLD source, according to (1-8), is:

$$L_c = 0.44 \times \frac{\lambda_0^2}{\Delta\lambda} = 0.44 \times \frac{1545^2}{32} = 32.8\mu m$$

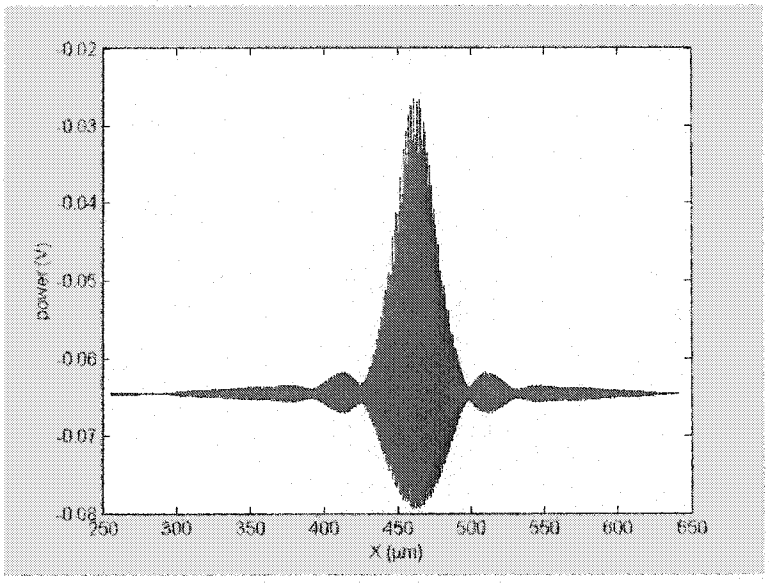


**Figure 2.4** The interferometric trace received for the quality test of the OCT setup

The movement of the reference mirror was fixed at 1000 counts/s, corresponding to a moving speed of 8.5 μm/s. Because the mirror reflected almost all the incident light with a quasi-perfect flat surface, it should provide the best interference trace of the system when the path delays between the sample and the reference beams are matched.

The test results are shown in Fig. 2.4. The interferometric signal had a main peak of 41.3 dB above the noise floor. The two symmetric echoes next to the main one are caused by the reflections from the diode output facets. In real tissue measurements, these echoes will not be seen since the reflected light from the tissue is weak. From the plot, the longitudinal resolution is the FWHM bandwidth of the interferometric signal trace

$$L_c = 3800 \times 0.0085 = 32.3 \mu m$$

It indicates that the real longitudinal resolution is 0.5 μm smaller than the theoretical coherence length. The theoretical analysis is based on a Gaussian spectrum shape of the source. However, the real spectrum of the source is not perfectly Gaussian.

# CHAPTER 3

# SOURCES

## 3.1 Introduction

The properties of the light source have a great impact on the image quality. For instance, the longitudinal resolution or the axial resolution of the OCT system is mostly based on the coherence length of the light source and does not depend on the focusing lenses. To date, the state-of-the-art axial resolution of OCT has reached 1 μm by means of a Ti:Sapphire modelocking pulse laser which generates a pulse duration of 5 fs with a bandwidth of over 300 nm [2]. The coherence length of this laser is calculated to be 1 μm based on its spectrum center wavelength and bandwidth. Another potential good quality source for OCT is visible light, with a spectrum bandwidth between 380 - 760 nm. The coherence length of this white light would be ~ 0.4 μm according to calculations. However, although it is clear that, in principle, a white light beam would be an excellent source for OCT imaging, a good white light with a high power density in its fundamental-transverse-mode is difficult to obtain. White light generation by high power femtosecond laser pulse is a possibility.

There are four primary properties for evaluating an OCT light source. These include the wavelength ($\lambda$), the bandwidth ($\Delta\lambda$), the single–transverse-mode power (P), and its stability. Other considerations include portability, ease of use, and general compatibility with the application environment. Some researchers prefer the near infrared range as the

first choice for the source since the typical tissue constituents, such as water and blood, have minimum light absorption in this spectral region. This is the reason why the ultra-short Ti:Sapphire mode-locked pulse laser, with the wavelength centered at about 800 nm, has been widely used as a source for experiments in OCT.

As part of the OCT project, an existing Ti:Sapphire femtosecond pulse laser in the Optoelectronics Laboratory has been refurbished and the obtained pulse duration was 71 fs with a spectrum bandwidth of ~ 46 nm. Its characteristics are described next.

### 3.2 The components of the laser cavity

The schematic diagram of the Ti:Sapphire laser cavity is shown in Fig. 3.1. An all-line argon-ion laser (Spectra-Physics 2030) is used as the pump beam. This beam also functions as the main axis of the cavity. It is very important for this laser beam to be aligned parallel with the table from the beginning of the alignment procedure. The half-wavelength plate and the cube polarizer are used for adjusting the polarization of the beam to be perpendicular with the table. The mode-matching lens (L) (12.5-mm fl) focuses the pump beam onto the center of the crystal. A small rotation of the lens, by ~5° with respect to the normal, will slightly improve the overlap of the pump beam with the cavity mode. The Brewster cut, 4.75 mm path length Ti:Sapphire crystal (Union Carbide C & P Co. Inc.) is in the center between two 10-cm radii of curvature mirrors which have a high reflection at 800 nm, and a high transmission at 488-514 nm. A single-stack, flat, high-reflection at 800 nm mirror and an output coupler mirror are employed on each end of the cavity. The Ti:Sapphire laser rod is surrounded with indium foil and is tightly clamped between two copper holders. It is maintained at an appropriate temperature by circulating chilled water.

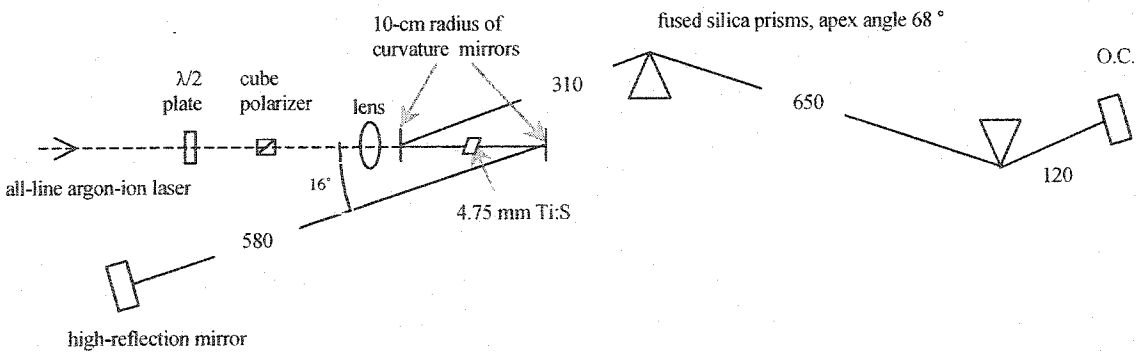


**Figure 3.1** The schematic diagram of the Ti:Sapphire laser cavity. The lengths are in mm

### 3.3 Astigmatism free design

Fig. 3.2 shows the main elements of the laser cavity. This type of resonator allows for a tightly focused beam waist at the center of the crystal and results in a low-threshold of lasing. The pump beam is incident on the crystal surface at the Brewster angle for minimum reflection power loss. However, an inclined interface causes astigmatism in the incident beam as it passes through the crystal. On the other hand, the pump beam is also incident onto the two 10 cm radii focusing mirrors at a certain angle and the focus points are off their optical axes; this also introduces astigmatism into the cavity. Astigmatism will distort the laser mode and reduce the stability of the laser. Fortunately, it has been found that the astigmatism introduced by the tilted mirrors is opposite to that introduced by the Brewster-angled Ti:Sapphire crystal rod. Astigmatism can then be compensated if the correct angle of incidence on the mirror ($\theta$) is chosen.

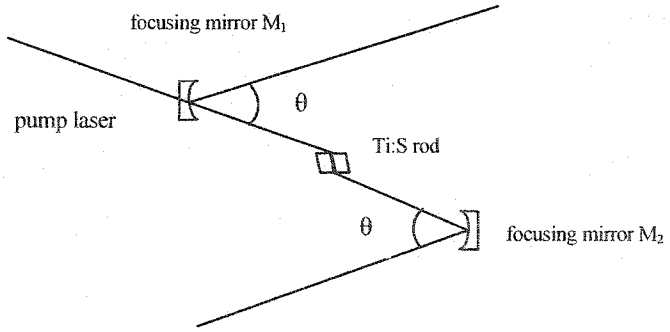


**Figure 3.2** The main parts of the laser cavity

For the case shown in Fig. 3.2, astigmatism compensation occurs when $\theta$ satisfies [8]:

$$n^{-4}h(n^2-1)\sqrt{n^2+1}-R\sin(\frac{\theta}{2})\tan(\frac{\theta}{2})=0 \qquad (3\text{-}1)$$

where h and n are the optical path length and the index of refractive of the crystal, R is the radius of curvature of the mirrors.

For our laser, the parameters are h = 4.75 mm, n = 1.7601, R = 100 mm then

$$1.7601^{-4}\times 4.75\times(1.7601^2-1)\sqrt{1.7601^2+1}-100\sin(\frac{\theta}{2})\tan(\frac{\theta}{2})=0$$

We get $\cos(\theta/2) = 0.9896$, so, $\theta = 16.5°$

### 3.4 Self mode locking

In a laser, ultra-short pulses are obtained by the interference effect between the longitudinal cavity modes within the laser resonator. For the Ti:Sapphire resonator, thousands of modes exist, ranging from 700 nm to more than 1000 nm in wavelength. If a phase relationship between all these modes can be fixed or locked, there will be only a few points inside the cavity where interference can be generated and this results in a single circulating pulse. The more modes that are phase locked, the shorter the pulse duration that will be produced. A pulse duration as short as 1 fs can be obtained if all the laser modes within the Ti:Sapphire laser are locked.

In a Ti:Sapphire crystal, phase locking of the modes occurs spontaneously by an effect known as the Kerr-lens effect. Therefore, it is also named self-mode locking. The refractive index of the crystal is nonlinear and intensity-dependent [9],

$$n(\omega,t) = n_0 + n_2 \mathrm{I}(\omega,t) \qquad (3\text{-}2)$$

where I is the intensity of the propagating beam. The index $n_2$ is the nonlinear index of refraction and is determined by the Kerr-lens effect. The Gaussian TEM00 modes propagate through the crystal and induce a graded–index lens due to the intensity distribution. This provides the self-focusing. Since the laser pulse has a much higher intensity compared with the CW beam, it is focused more strongly and closer to the center and is more collimated than the other lasing modes. Thus the pulse circulating in the cavity will receive a higher gain whence mode-locked operation [10-12].

### 3.5 Group–velocity dispersion compensation

Dispersion is an extremely important factor for the femtosecond lasers. The laser pulses can be broadened by the dispersion induced by the Ti:Sapphire rod. Adjusting the bandwidth and the pulse duration of the short pulse laser becomes possible using the negative dispersion provided by a prism pair.

The roundtrip time for light in the laser cavity can be expressed as a Taylor series [13][14]:

$$T(\omega)=\frac{\partial\phi}{\partial\omega}=\phi'(\omega_0)+\phi''(\omega_0)\Delta\omega+\frac{1}{2}\phi'''(\omega_0)\Delta\omega^2+\frac{1}{6}\phi''''(\omega_0)\Delta\omega^3+\cdots \qquad (3\text{-}3)$$

where $\phi$ is the total phase shift of light after one cavity round-trip, and $\phi'$ , $\phi''$ … are the derivatives of the phase. Inside the formula, the second item is called the group velocity dispersion (GVD) which leads to linear chirp. The third term, proportional to $\phi'''$, is called the third-order dispersion (TOD).

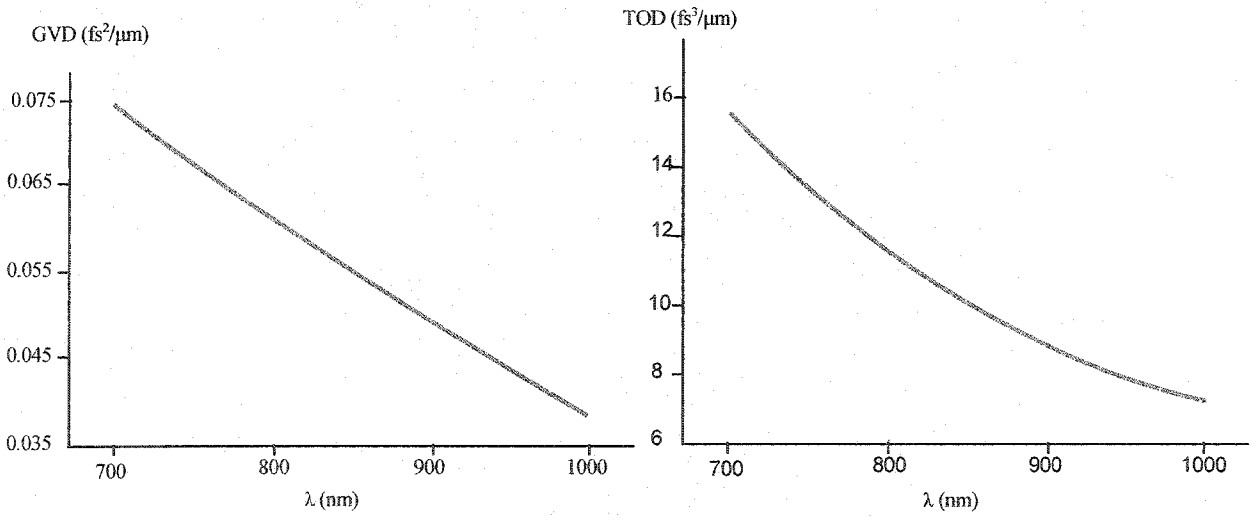


**Figure 3.3** The Ti:Sapphire GVD and TOD as a function of the wavelength [8]

Fig. 3.3 depicts the Ti:Sapphire GVD and TOD as a function of the wavelength. It indicates that the cavity GVD and TOD are both positive and inversely proportional to the wavelength. In general, ultra-short pulses of femtosecond duration cannot be obtained unless the dispersion in the laser cavity has been reduced near to zero. The prism pair is thus introduced into the cavity for the purpose of dispersion compensation. The second order dispersion or group velocity dispersion of the prism pair is calculated using the derivatives of the phase with respect to frequency [11][15-17]:

$$\phi'' = \frac{d^2\phi}{d\omega^2} = \frac{\lambda^3}{2\pi^2 c^2}\frac{d^2P}{d\lambda^2} \tag{3-4}$$

and the third-order dispersion is given by:

$$\phi''' = \frac{d^3\phi}{d\omega^3} = \frac{-\lambda^4}{4\pi^2 c^3}(3\times\frac{d^2P}{d\lambda^2} + \lambda\frac{d^3P}{d\lambda^3}) \tag{3-5}$$

where P is the path length in the prism pair, and c is the velocity of light. The derivatives of P with respect to λ are given by:

$$\frac{d^2P}{d\lambda^2} = 4\left[\frac{d^2n}{d\lambda^2} + (2n - n^{-3})(\frac{dn}{d\lambda})^2\right] l_p \sin\beta - 8(\frac{dn}{d\lambda})^2 l_p \cos\beta \tag{3-6}$$

$$\frac{d^3P}{d\lambda^3} = 4\frac{d^3n}{d\lambda^3} l_p \sin\beta - 24\frac{dn}{d\lambda}\frac{d^2n}{d\lambda^2} l_p \cos\beta \tag{3-7}$$

where $l_p$ is the distance between the prism apexes, n is the refractive index of the prism

material and β is an angle of the optical path with respect to the reference line as indicated in Fig. 3.4. Parameters such as n, $dn/d\lambda$, $d^2n/d\lambda^2$, and $d^3n/d\lambda^3$ can be found from optical glass reference books.

Generally, the angle β is very small, so sin β << cos β. The value of GVD and TOD will become negative when $l_p$ gets bigger. So, there is an optimal position where the total GVD of the cavity is near zero. TOD can be minimized by using a shorter crystal rod and choosing an appropriate prism material [18]. The prism material for our laser is fused silica which has a very low TOD value. We performed the dispersion compensation of the cavity by expanding the prism apexes distance $l_p$ by 20 mm each time, while comparing the modelocking properties of the received laser pulse. Finally, we fixed the length $l_p$ =650 mm when we obtained a 71 fs pulse laser.

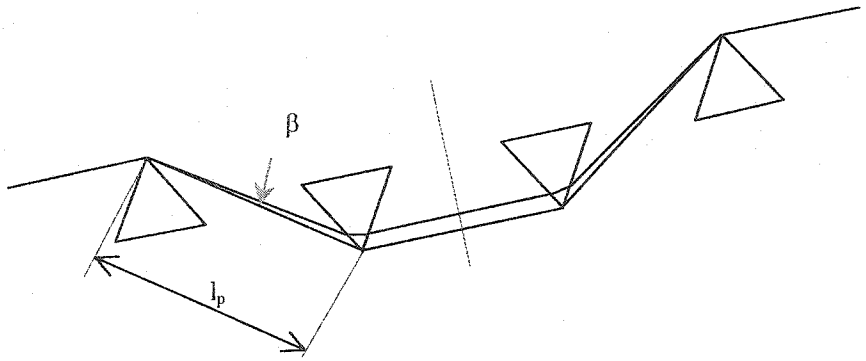


**Figure 3.4** Position of the prism pair

# CHAPTER 4

# INTERFERENCE SIGNAL

## 4.1 Introduction

Unlike a traditional imaging technique, the principle of OCT is based on the interference with partial coherence light source in a Michelson (or other) interferometer. An optical beam backreflected or backscattered from inside a biological tissue at a certain depth will contain time-of-flight information, which in turn yields spatial information about its microstructure. Two kinds of Michelson interferometers are popular in recent OCT setups; the fiber-optic type is already used for clinical applications whereas the free-space type is mostly used in laboratories for research.

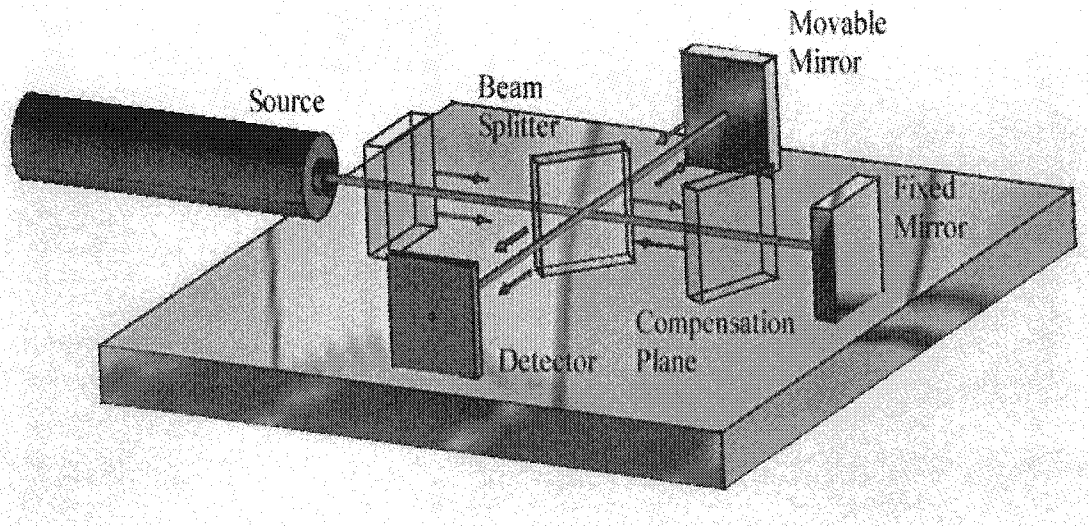


**Figure 4.1** A schematic diagram of a free-space Michelson interferometer

## 4.2 Interference of temporal coherence sources

For simplicity, assume that there are two harmonic waves propagating along the x-axis with electromagnetic field along y-axis as can be seen in Fig.4.2. These waves can be expressed as [1]:

$$Y_1 = A_1 \sin(\omega t+\phi_1) \qquad (4\text{-}1)$$

$$Y_2 = A_2 \sin(\omega t+\phi_2) \qquad (4\text{-}2)$$

where $A_1$ and $A_2$ are the amplitudes of the waves, $\phi_1$ and $\phi_2$ are the phases. Because the two waves have the same frequency and speed, when they overlap in space, the recombination wave will be the linear superposition of these two waves. Thus we have:

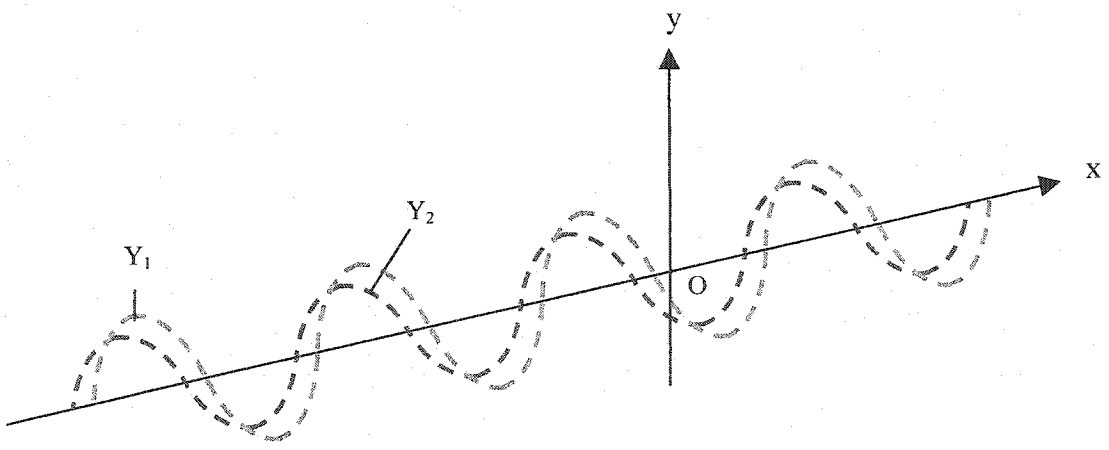


**Figure 4.2** Superposition of two harmonic waves $Y_1$ and $Y_2$

$$Y = Y_1 + Y_2 = A_1 \sin(\omega t+\phi_1) + A_2 \sin(\omega t+\phi_2)$$

$$= A_1 \sin\omega t\cos\phi_1 + A_1 \cos\omega t\sin\phi_1 + A_2 \sin\omega t\cos\phi_2 + A_2 \cos\omega t\sin\phi_2$$

$$= (A_1 \sin\phi_1 + A_2\sin\phi_2) \cos\omega t + (A_1 \cos\phi_1 + A_2 \cos\phi_2) \sin\omega t$$

$$= A \sin\phi \cos\omega t + A \cos\phi \sin \omega t$$

$$= A \sin (\omega t + \phi) \qquad (4\text{-}3)$$

This equation means the composite wave of those two harmonic waves is also harmonic with the same frequency as the two components waves, but its amplitude and phase may be different. To get the equation (4-3), we have used:

$$A \sin\phi = A_1 \sin\phi_1 + A_2\sin\phi_2 \qquad (4\text{-}4)$$

$$A \cos\phi = A_1 \cos\phi_1 + A_2 \cos\phi_2$$

Hence

$$A^2 = A_1^2 + A_2^2 + 2\, A_1A_2 \cos(\phi_2 - \phi_1) \qquad (4\text{-}5)$$

Or

$$I = I_1 + I_2 + 2\sqrt{I_1 I_2}\cos(\phi_2 - \phi_1) \qquad (4\text{-}6)$$

The factor $2\sqrt{I_1 I_2}\cos(\phi_2 - \phi_1)$ in this equation is known as the interference term, which determines the properties of the fringes. The difference in phase of the two waves is:

$$\delta = \phi_2 - \phi_1 = \frac{2\pi}{\lambda}\Delta \qquad (4\text{-}7)$$

where $\Delta$ is the difference of the optical path length between the two waves. Fig. 4.3 illustrates the superposition of two harmonic waves $Y_1$ and $Y_2$.

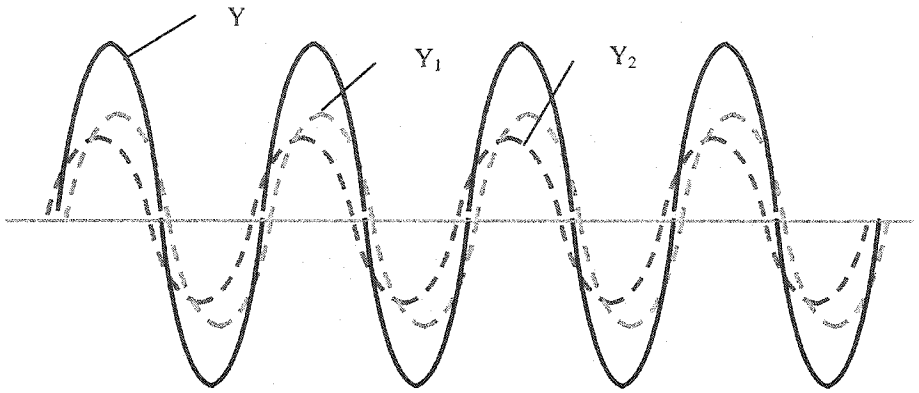


**Figure 4.3** Superposition of two harmonic waves $Y_1$ and $Y_2$

### 4.3 Temporal and spatial coherence

Atoms or molecules emit light in a finite time duration Δt. At each emitting time, one wave train is created with a finite length. A light wave is composed of a huge number of wave trains as illustrated in Fig.4.4.

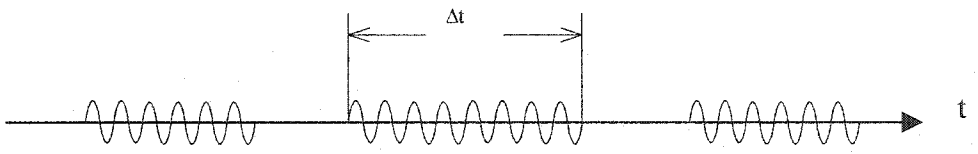


**Figure 4.4** A wave consists of wave trains

The time duration Δt during which the average constituent wave exists is known as the coherence time. It is the inverse of the frequency bandwidth Δν: $\Delta t \Delta \nu \approx 1$. The coherence length of the wave Δx is defined as:

$$\Delta x = c\, \Delta t$$

It is the length of a wave train within which a fixed phase relation can be obtained. An interference cannot occur in principle between different wave trains because the fixed phase relation is lost. For the same wave train, there exists two basic coherence effects known as temporal and spatial coherence.

The optical bandwidth determines the coherence length of a source. The light wave

with a narrow bandwidth will have a long coherence length. For instance, most lasers can have a coherence length as long as tens of kilometers. However, most light sources have a relatively large bandwidth $\Delta\lambda$ that result in a short coherence length. These sources are partially coherent sources.

### 4.4 Interference of partially coherent light

First, we consider the interference between two light waves at wavelengths at $\lambda_1$ and $\lambda_2$. Fig.4.5 illustrates two laser beams incident onto a Michelson interferometer. Each of them will form its own interference pattern system.

$$I(\lambda_1) = 2 \times I_0(\lambda_1) \times [1 + \cos(\frac{2\pi}{\lambda_1}\Delta)] \quad (4\text{-}8)$$

$$I(\lambda_2) = 2 \times I_0(\lambda_2) \times [1 + \cos(\frac{2\pi}{\lambda_2}\Delta)] \quad (4\text{-}9)$$

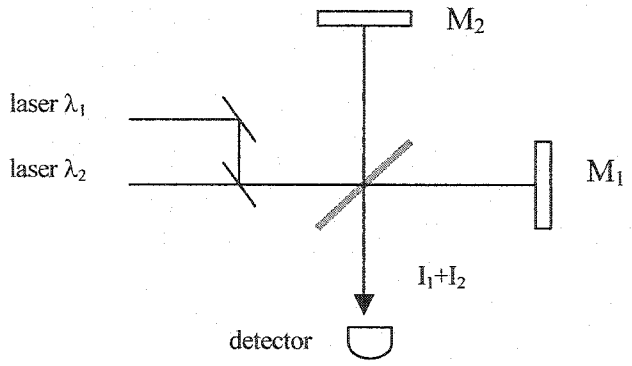


**Figure 4.5** Interference between two lights with different wavelengths

The superposition of the two interference patterns results in a new interference pattern. The brightness of the new pattern changes periodically according to the optical path length difference between the two waves. At zero path difference, both of them will reach their maximum intensity so that a total maximum intensity will be observed. However, when the

optical path difference Δ becomes larger, the bright fringes of one pattern will mix with the dark fringes of the other pattern system. As a result, the combined fringe pattern loses contrast. This phenomenon is shown on Fig.4.6.

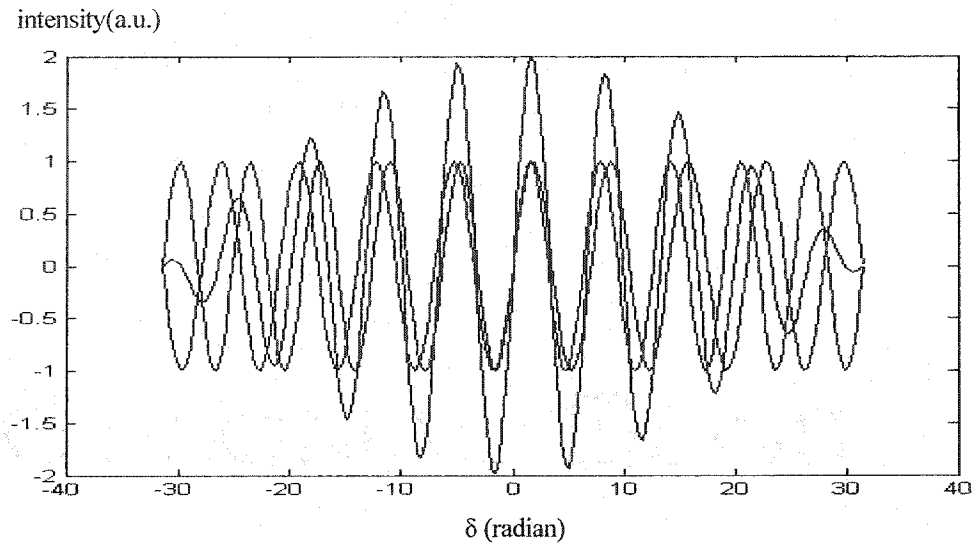


**Figure 4.6** The interference pattern of two waves

Next, if we consider the interference of more than two wavelengths of light, the interference intensities will be:

$$I\ (\lambda_1) = 2 \times I_0(\lambda_1) \times [1 + \cos(\frac{2\pi}{\lambda_1}\Delta)]$$

$$I\ (\lambda_2) = 2 \times I_0(\lambda_2) \times [1 + \cos(\frac{2\pi}{\lambda_2}\Delta)]$$

$$I\ (\lambda_3) = 2 \times I_0(\lambda_3) \times [1 + \cos(\frac{2\pi}{\lambda_3}\Delta)]$$

$$I\ (\lambda_m) = 2 \times I_0(\lambda_m) \times [1 + \cos(\frac{2\pi}{\lambda_m}\Delta)]$$

Such that

$$\sum I(\lambda_1, \lambda_2, ...\lambda_m) = 2 \times \sum_{1}^{m} I_0(\lambda_i) \times [1 + \cos(\frac{2\pi}{\lambda_i}\Delta)] \qquad (4\text{-}10)$$

This phenomenon is shown on Fig.4.7.

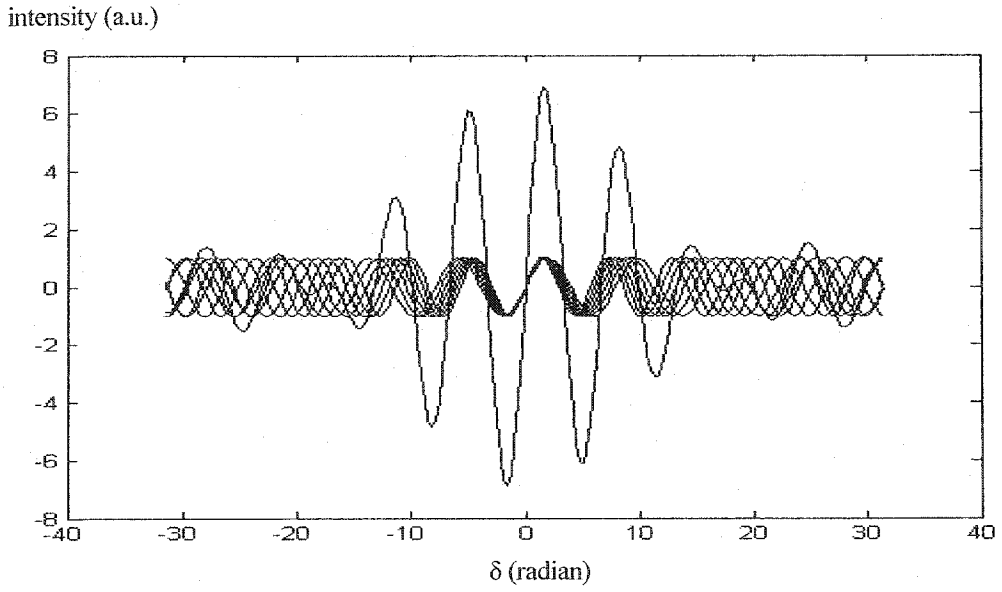


**Figure 4.7** The interference pattern of seven waves

Now, consider a broadband source with a continuous spectrum. The interference intensity then becomes [19][20]:

$$I(\Delta) \approx 2I_0 \int_0^{\infty} S(\nu)\cos(2\pi\Delta\nu)d\nu \qquad (4\text{-}11)$$

where $S(\nu)$ is the spectral density of the source.

We see that there is a Fourier transform relationship between the spectral density of a continuous spectrum light source and the interference intensity distribution produced by the source. If the spectral density of a light source is a Gaussian distribution function,

$$S(\nu) \propto e^{-4\ln 2(\frac{\nu-\nu_0}{\Delta\nu})^2}, \tag{4-12}$$

where $\Delta\nu$ is the FWHM bandwidth of the source as illustrated in Fig 4.8 (a), the interference intensity can be written as:

$$\begin{aligned} I(\Delta) &\approx 2I_0 \int_0^\infty S(\nu)\cos(2\pi\Delta\nu)d\nu \\ &\propto e^{-4\ln 2(\frac{\Delta}{L_c})^2}\cos(2\pi\Delta\nu) \end{aligned} \tag{4-13}$$

where

$$L_c = \frac{2\ln 2}{\pi}(\frac{\lambda_0^{\,2}}{\Delta\lambda}) = 0.44\times\frac{\lambda_0^{\,2}}{\Delta\lambda} \tag{4-14}$$

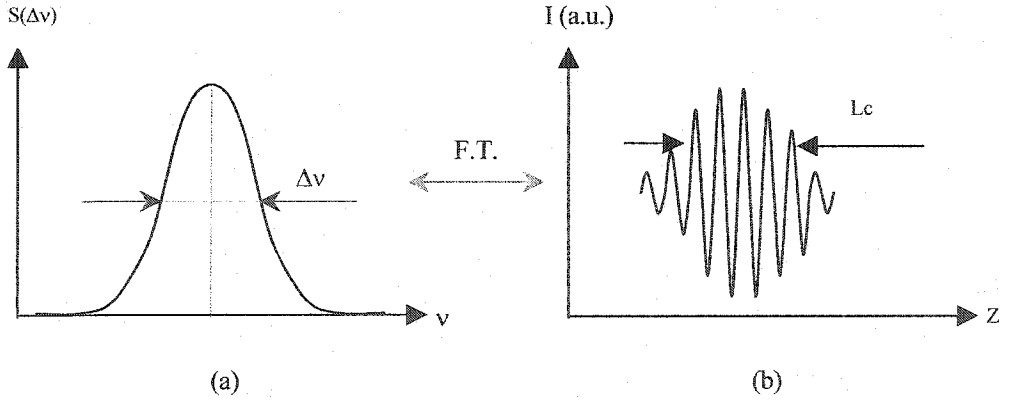


**Figure 4.8** The Fourier transformation (F.T.) relationship between the spectral density of a continuous spectrum source and the interference trace

$L_c$ is called the coherence length of the partially coherent light source. $\lambda_0$ is the center wavelength of the source and $\Delta\lambda$ is the FWHM bandwidth of the source. Fig 4.8 (b) illustrates that the interference fringes can be observed only when the optical path length difference is less than the coherence length of the source $L_c$. The broader the spectral density of the light source, the narrower the interference intensity pattern will be. Narrow interference intensity also means that less interference fringes can be observed.

If the light source is white-light, an extremely short coherence length will be obtained due to the broad spectrum range of the source. Only a few colored fringes will be seen surrounding the zeroth order fringe at zero path difference. This is because all the wavelengths produce their own interference pattern system with the same zeroth order position for all. When the path difference increases, some maximum of one order will overlap with the minimum of another one, and the fringes will wash out.

### 4.5 Two SLD examples for OCT

With the free-space Michelson interferometer as shown in Fig. 2.2, two SLD sources were used for OCT experiments.

The first one was obtained by AR coating in-house a semiconductor laser whose spectrum is shown in Fig 4.9 (a). The center wavelength is 1479.3 nm, and the FWHM bandwidth is 18.6 nm. So, the coherence length of this source is (1-8):

$$L_c = 0.44 \times \frac{1479.3^2}{18.6} = 51.77 \mu m$$

a Ge photodetertor was used to detect the interference signal. The interference pattern of this source is shown in Fig 4.9 (b).

The second SLD is a commercial broadband source from JDS Uniphase and spectrum is shown in Fig 4.10 (a). Its center wavelength is 1545 nm, and the FWHM bandwidth is 32 nm. For this broadband light source, the coherence length is:

$$L_c = 0.44 \times \frac{1545^2}{32} = 32.8 \mu m$$

and the received interference signal pattern is shown in Fig 4.10 (b).

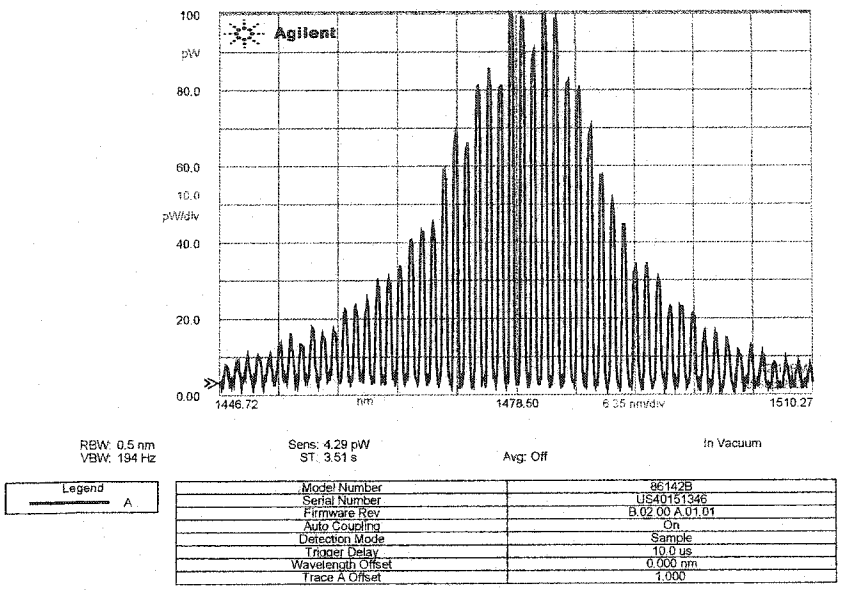


(a)

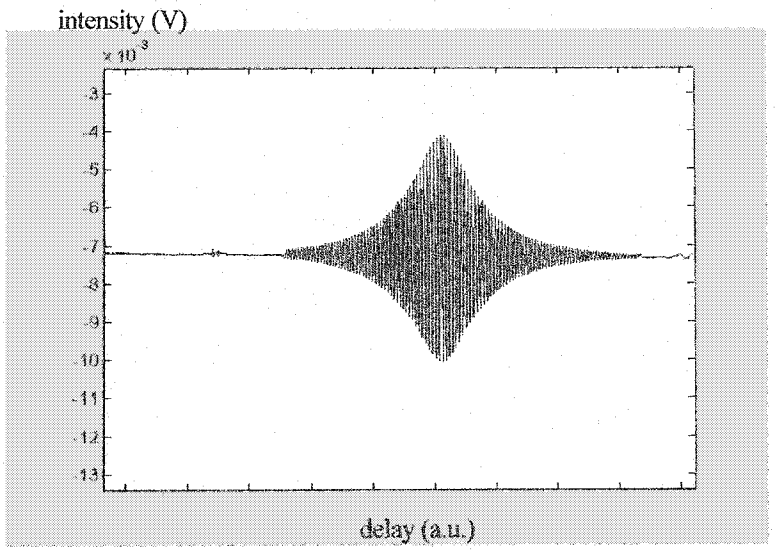


(b)

**Figure 4.9** The spectrum of the SLD source and its interference trace

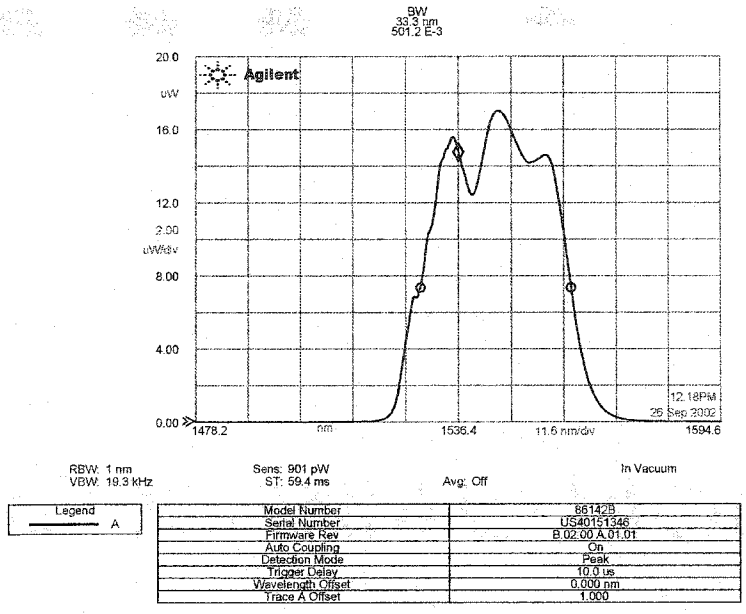


(a)

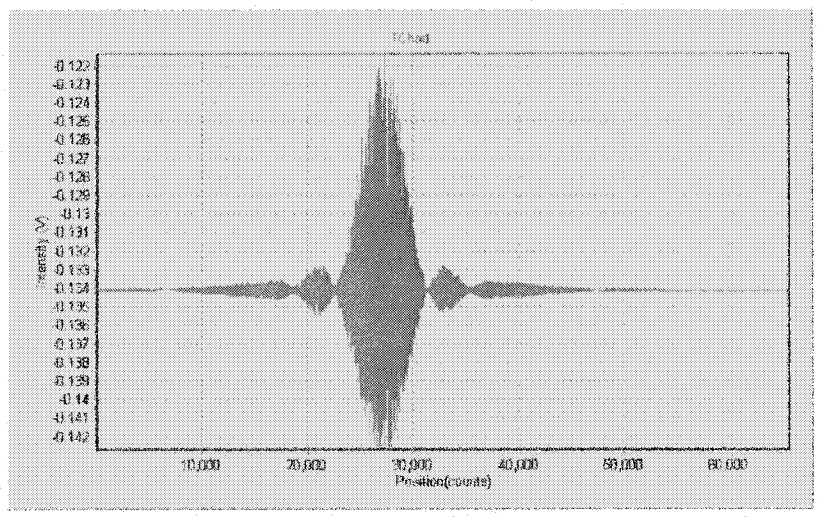


(b)

**Figure 4.10** The spectrum of the second SLD source and its interference trace (8.5 nm/count)

# CHAPTER 5

# THE ELECTRICAL SYSTEM OF OUR OCT SETUP

## 5.1 Introduction

An OCT setup consists of two main parts. One is the optical setup described in previous chapters, and the other one is theelectrical setup which will be described in this section.

OCT takes cross-sectional images of an object by gathering a series of interference patterns between the reference light and the backreflected or backscattered light from the various constituents of the object. Two computer-controlled linear positioners are used. One for the longitudinal scan of the reference mirror and the other for the lateral scan of the object. A computer is also in charge of data acquisition and stores and displays the intensity modulation data provided by the photodetector. This program allows 1-D or 2-D scanning of the sample and allows the user to set the scanning range and speed. The program can also display the results on the screen.

The acquired data is stored in a Matlab file which consists of the position and intensity information of the internal structure of the sample. This information is obtained by an envelope detection algorithm and a low-pass filter. The filtered information is then displayed as a 2-D contour map.

## 5.2 Data acquisition and scanning control system

Fig. 5.1 illustrates the block diagram of the data acquisition and scanning control system. The computer controls the two motors (PI Physik Instrumente) for the longitudinal and lateral scanning. The moving speed of the motors can be set up to 1.5 mm/s, and the moving range of the motors are 25 mm for the lateral scan (x-axis) and 100 mm for the longitudinal scanning (z-axis).

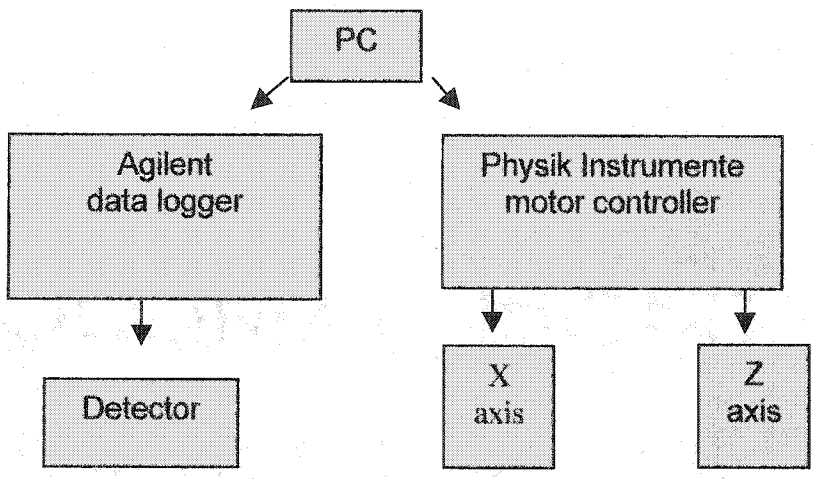


**Figure 5.1** The block diagram of the data acquisition and scanning control system.

A data logger (Agilent ) was used to record the intensity modulation data, coming from the detector, at a rate of 60 frames per second. Every frame relates to one point inside the recorded interference trace and a typical image is defined by 50 x 5000 points. The 50 means that an image can consist of up to 50 lateral scanning lines with each line corresponding to a longitudinal scan of 5000 points. However, the distance between every

two scan lines is determined by the lateral resolution of the experimental setup, which is equal to the size of the focal spot of the sample beam. When a longitudinal scan is finished, the motor moves the sample to its next position along x-axis. In the mean time, the reference mirror returns back to its starting position and begins the next longitudinal scan.

If the motor speed is increased, the longitudinal scan will be performed more quickly, but it will lose more detailed interference information and will result in a lower longitudinal resolution. This effect could be compensated by an increased data acquisition rate, but 60 samples/s is the limit of the data logger.

The data acquisition and scanning control processes are accessed by a menu shown in Fig. 5.2. The biggest window at the right bottom shows the scanning results. The horizontal axis is the position value in units of counts (8.5 nm/ count) used internally by the motor controller, and the vertical axis is the intensity value in the unit of volts from the amplified photocurrent. In the top right window, the moving position of the reference mirror and the point number of the longitudinal scan is displayed.

The left window has three selection buttons identified by range finder, 1-D, and 2-D scan. Here, we can set the start, and stop position of the two scans and their moving speeds. The save button can save the recorded data to a Matlab file.

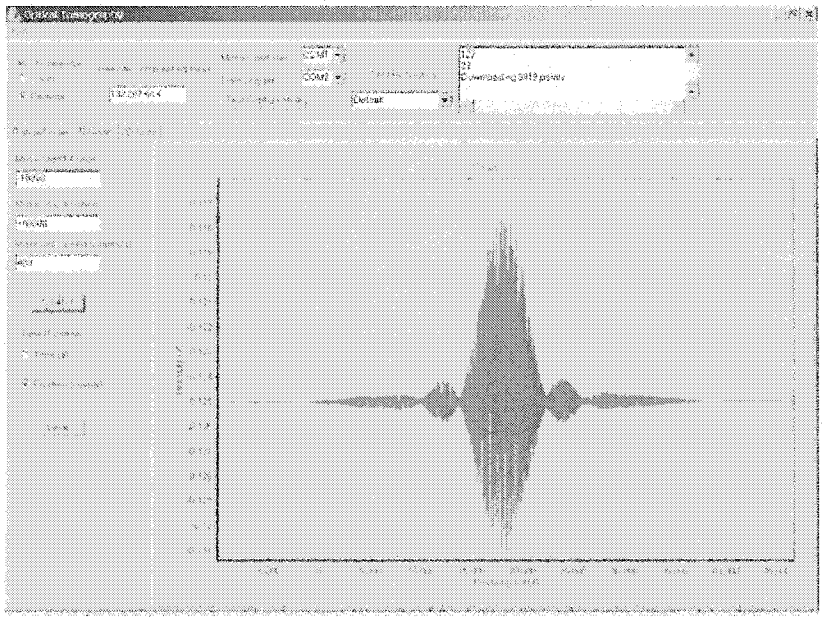

**Figure 5.2** Menu window of the data acquisition and scanning control program

### 5.3 The envelope detection algorithm (Matlab) and contour of the final image

The saved interference data in the Matlab files consist of the position and intensity information of the internal struture of the sample. An envelope detection algorithm and a low-pass filter is needed to process that information and produce a 2-D contour map. Fig. 5.3 illustrates the block diagram of this data processing system.

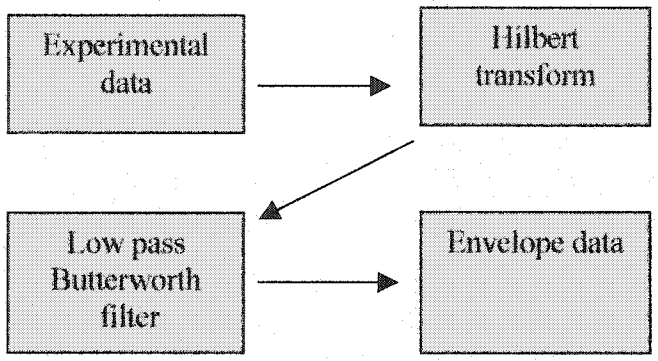


**Figure 5.3** Block diagram of the final data processing system

In Matlab, the data is processed by a function named filter_oct(). This function includes a low pass Butterworth filter and a Hilbert transform to obtain the enveloppe of the input data. The order of the filter and the cutoff value can be selected.

An example showing how the order of the filter and the cutoff influence the envelope of the signal is displayed in Fig. 5.4. In this plot, (a) shows the saved data of a longitudinal scan. (b) is the envelope of this interference trace with a filter order of 7 and cutoff order of 0.03. We can see that these parameters give an envelope which is very close to the base

signal. Because there are so many peaks, the final OCT image will have a lower contrast. (c) shows the result when the filter order and the cutoff order are 1 and 0.001 respectively. In this case, there is only one peak which results in a very good contrast value of the final image, but the resolution of the image will be much lower than the last one.

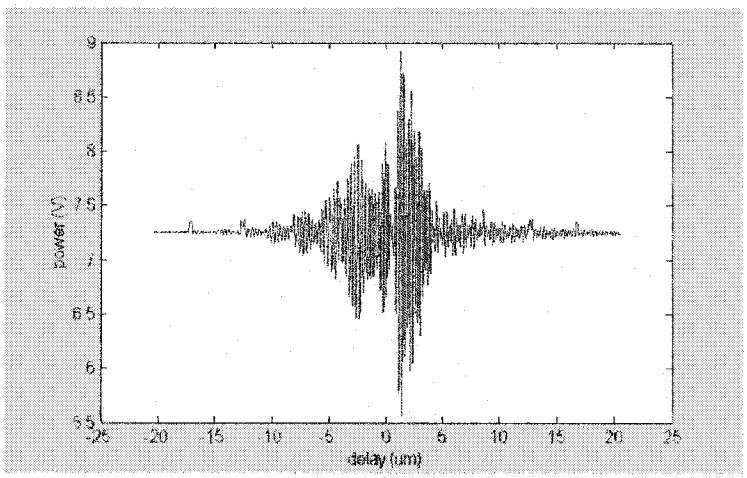


(a)

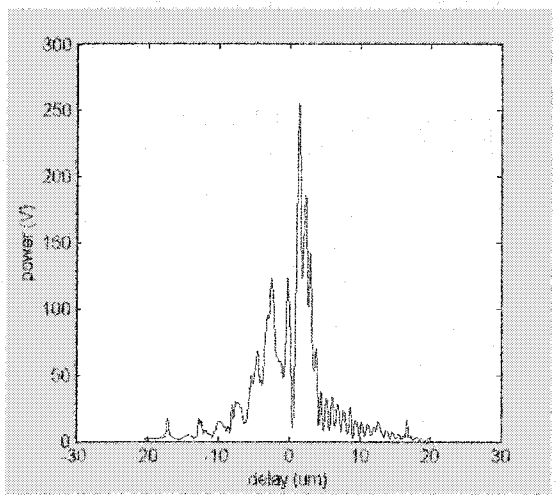


(b)

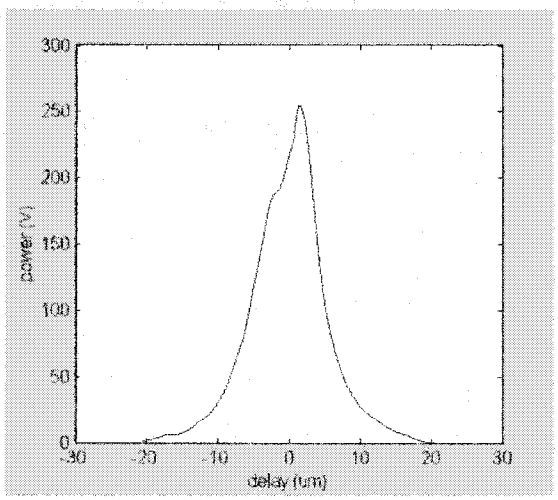


(c)

**Figure 5.4** The effect on the envelop curve with different filters and cutoff orders

Each envelope of the interference trace provides the microstructure of the sample in the scanning axis by counting the positions and the intensities of the peaks. The built-in Matlab function contour() is used to combine all of the scanning data to form a cross-sectional image of the sample by revealing the peaks at appropriate positions.

# CHAPTER 6

# EXPERIMENTAL RESULTS

## 6.1 Introduction

Three steps are needed in order to get a final image of the sample. The first step is to sweep the reference mirror to measure the interference signal along a longitudinal axis which contains the information of the sample. Second, the envelope of the interference signal pattern, consisting of the position and intensity information of the internal structure, is obtained through data processing. This provides the image of a certain longitudinal axis inside the sample. Finally, a two-dimensional map of reflection sites is created by gathering a series of longitudinal scans at different lateral locations.

The separation between two longitudinal scans is determined by the focusing spot size. This provides the lateral resolution of the OCT system. The longitudinal resolution of OCT is determined by the coherence length of the source and has not much to do with the optical components of the system. The key point of the OCT technique is the performance of each single longitudinal scan.

As illustrated by Fig. 2.2 in Chapter 2, the OCT experimental setup which is based on a free-space Michelson interferometer has been built in our laboratory. In one implementation, a SLD (JDS Uniphase) is employed to be the source which emits the broadband light at the center wavelength of 1545 nm with a FWHM bandwidth of 32 nm.

The coherence length is around 32.8 μm. A NA=0.25 microscope objective (Edmund Optics) is employed to focus the beam onto the sample. This microscope objective focuses the beam into a spot with a minimum spot size of ~10 μm and an axial scanning range of 850 μm. The reference mirror and the sample stage are mounted on the linear positioning stages (PI Physik Instrumente) that have the maximum movement range of 150 mm at the adjustable moving speed from 0 to 1.5 mm/s. An infrared camera is used to monitor the fringe pattern on TV when it is available, which provides a convenient way for fine alignment of the system.

Four different samples for tests of longitudinal axis scanning have been used with this setup. Among these, a specially made grating has been designed to fit the parameters of the setup. As an example of natural material, a piece of onion has been selected to be one of the samples.

## 6.2 A glass plate sample for OCT

The initial alignment of the experimental setup is carried out using a mirror instead of a real sample. The mirror provides a strong reflection in the sample arm that simplifies the alignment process since the interference signal is very strong and easy to obtain. By monitoring the fringe pattern on a TV screen, further fine alignments can be easily performed. This mirror is a one surface reflecting object.

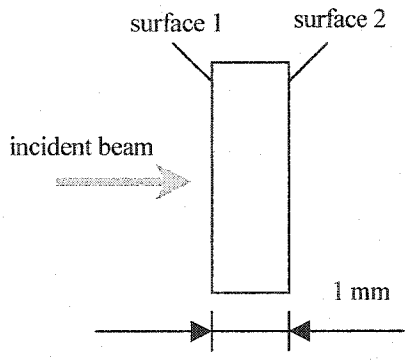


**Figure 6.1** The sample of a piece of glass plate

However, real samples do not have the reflecting surface with such a high reflecting power. To test if this setup is ready for imaging a real sample, a two surface reflecting object - a piece of glass plate - is introduced as shown in Fig.6.1. Because this glass plate is transparent to the source beam, the reflected intensities from the two surfaces are weak and lead to a dim interference signal. Fine alignment of the system must be made to make sure these two interfaces are within the scanning range of the microscope objective and that the plate just retro-reflects the incident beam. These alignments yield a clear fringe pattern with

the field of view overlapping the center of the pattern. The interference fringe pattern is shown in Fig.6.2. By moving the reference mirror back and forth, the fringes will be seen moving in and out of the center of the pattern. By moving the sample stage horizontally, the movement of the fringes are very slowly because the surface of the plate is not perfectly flat.

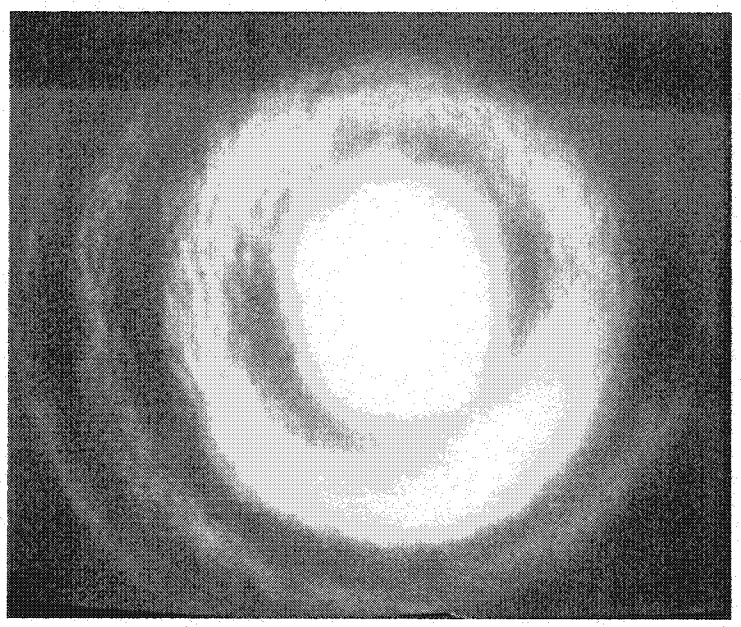

**Figure 6.2** The received interference fringe pattern

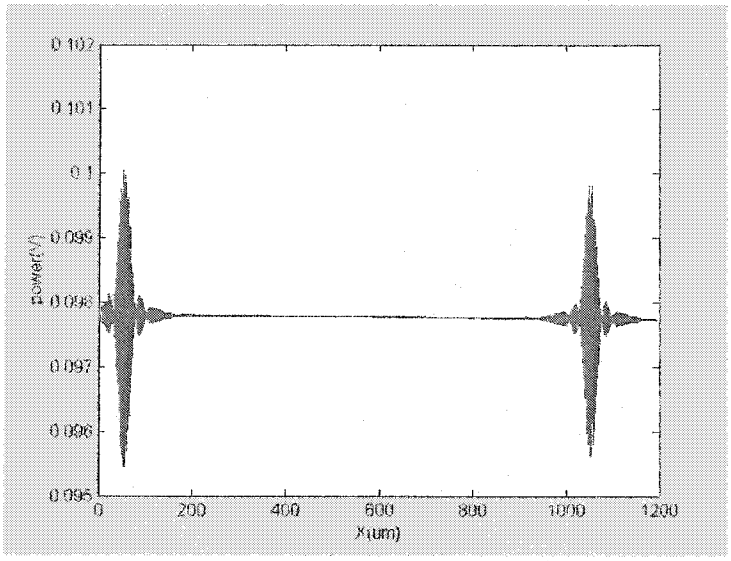


**Figure 6.3** An interference signal produced by a longitudinal scan

Fig.6.3 shows an interference signal obtained by a longitudinal scan of the reference mirror. This interference pattern gives the exact positions of the interfaces that coincide with the maximum intensities. The reflected intensity of surface 2 is slightly weaker than that of surface 1 due to the extra reflection and absorption inside the glass. The envelope of this interference signal is shown on Fig. 6.4.

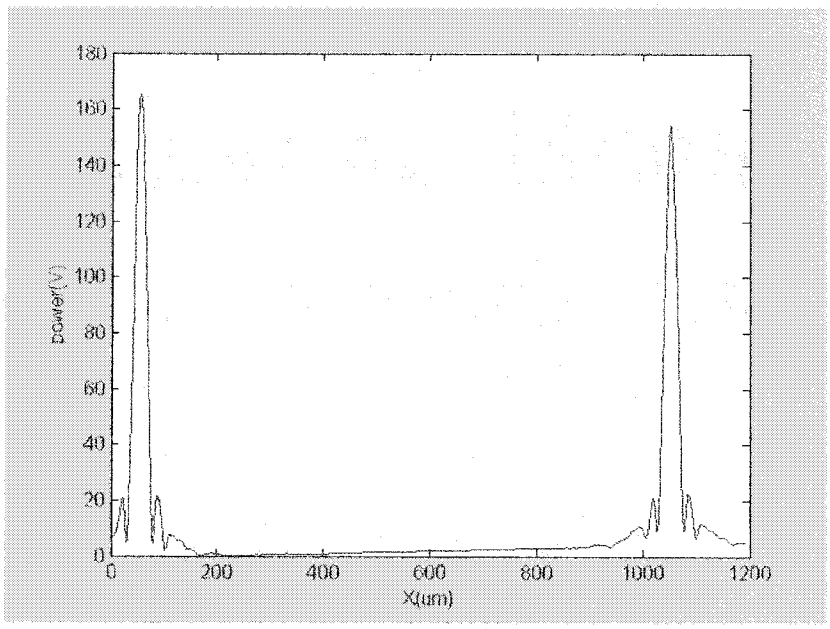


**Figure 6.4** The contour of the interference signal

### 6.3 A three layer sample for OCT

A further experiment was performed with a three layer sample as shown in Fig.6.5. A mirror was added behind the glass plate. This time, the reflected intensity from the mirror became the highest one although this reflected beam gets reduced when passing through the glass, as indicated in Fig.6.6. This high intensity yields a brighter point along the axis. The distance between the mirror and the plate is measured to be 0.153 mm from the data.

From the Figure, we find that two reflecting layers can be distinguished from each other when the distance is equal to or larger than 30 μm. These results confirm that the procedure is correct and that a longitudinal trace of the sample can be obtained.

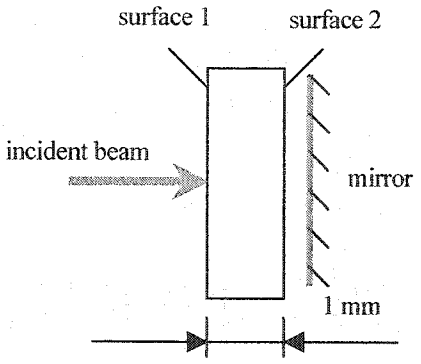


**Figure 6.5** The three layer sample

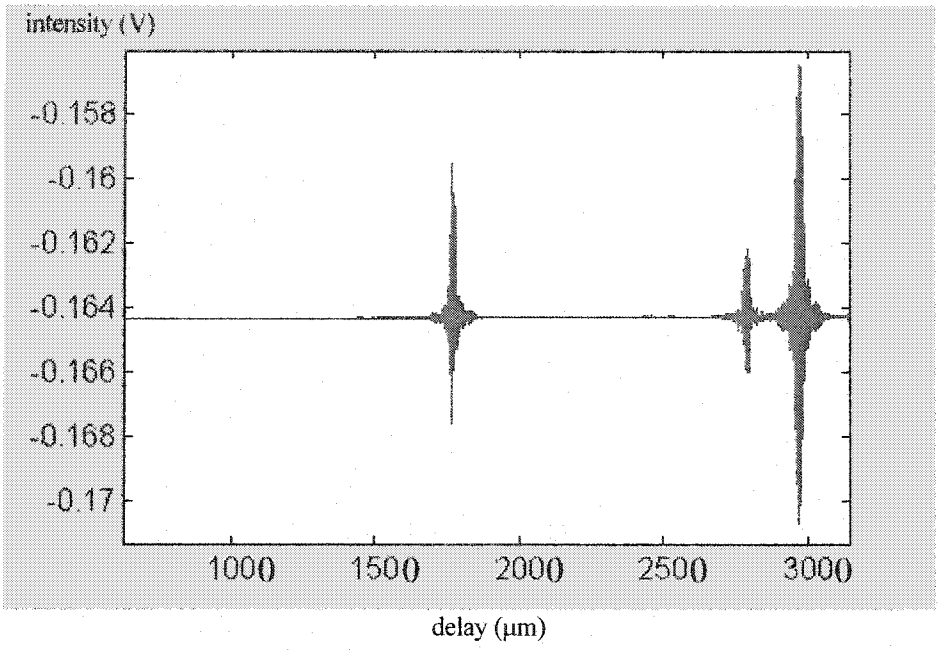


**Figure 6.6** An interference signal of three layer sample

### 6.4 A man-made grating sample for OCT

In the previous section, the quality of the longitudinal scan of the OCT system has been tested by means of multiple, by multiplying reflecting layers placed at different distances. In this section, the quality of the lateral scan of the system will be considered.

Since the images are composition of longitudinal and lateral scans, the scanning path of the reference mirror must be aligned along the optical axis of the reference arm. And also, the scanning path of the sample must be perpendicular to the optical axis of the sample arm. Otherwise, the received signal will be distorted after scanning a certain distance.

Because the lateral resolution of the OCT system is determined by the focusing spot size of the incident beam focused by the microscope objective, the spot size becomes an important parameter. For measuring the focusing spot size of this system, an experiment has been performed as illustrated by Fig.6.7.

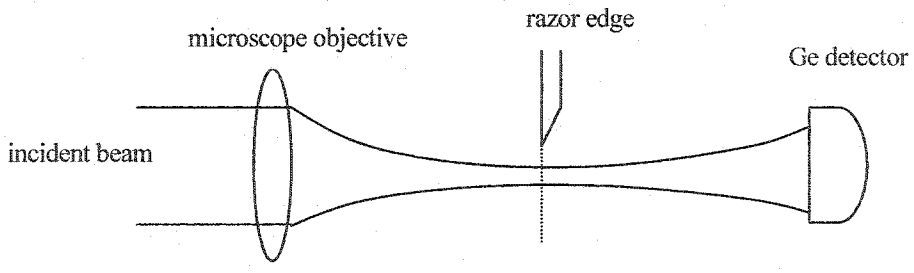


**Figure 6.7** A setup for measuring the spot size of the sample beam

A Ge detector was put in front of the sample beam to measure its intensity. A razor edge was fixed on a moving stage just next to the beam. The razor edge was moved into the beam at a certain speed while recording the intensity changes as a function of the movement of the blade using the BenchLink software. The position of the maximum and the minimum level of intensity were recorded. The distance between these two points was chosen as the diameter of the beam. Moving the razor edge along the axis of the sample arm, the shape of the sample beam could be determined and the waist of the beam was considered to be the focusing spot. In our experimental setup, A NA=0.25 microscope objective (Edmund Optics) was employed which produced a minimum focusing spot size of about 10 μm in diameter and an axial scanning range around 850 μm. Therefore, the transverse resolution of our system is about 10 μm, that is not very high, but good enough for performing the internal imaging of some large biological cells and other samples, such as gratings, etc.

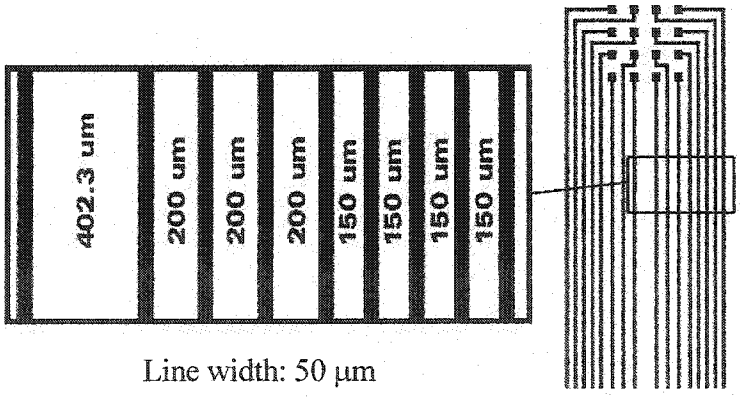


**Figure 6.8** The structure of a grating target for OCT

A grating target was designed and fabricated for testing the lateral scanning properties of the system. Fig.6.8 shows the structure of this target. This sample is based on a piece of glass plate with 9 thin metal bars deposited on one side. The deposited material had a higher reflection coefficient than glass. This sample was prepared using micro-fabrication techniques.

The received interference signals produced by the longitudinal scan of the sample are shown in Fig.6.9. They refer to each interface of the sample in one longitudinal scan. Fig.6.9 (a) corresponds to the situation when there is no metal bar on the back surface of the sample. The interference pattern is the same as that of a standard glass plate. The distance between the two signals is equal to the optical path length of the glass plate, that is the thickness of the glass plate multipled by the index of refraction of glass. Fig.6.9 (b) indicates the reflected signal from the back metallized surface which is stronger than that from the front surface.

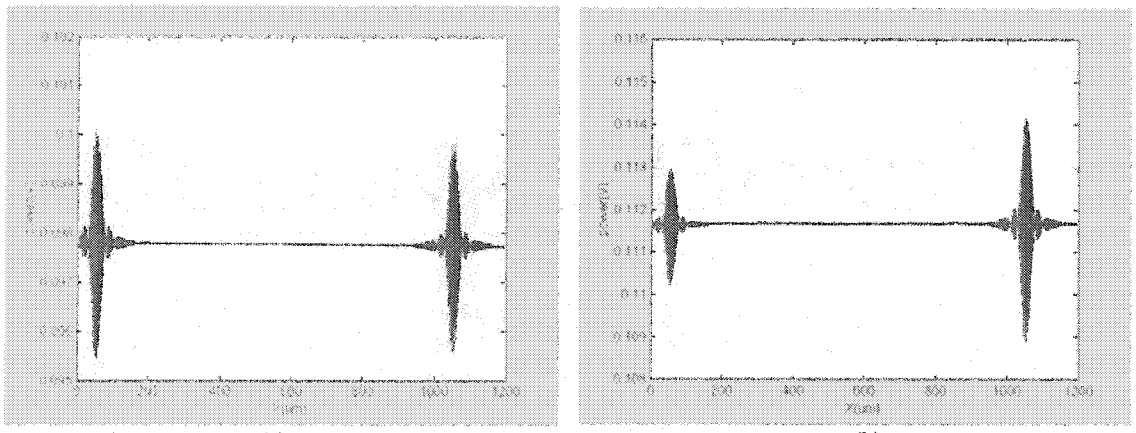

(a) (b)

**Figure 6.9** The interference signals of a longitudinal scan of the grating sample

The next longitudinal scan was taken after a 10 μm lateral translation. After completing 92 longitudinal scans, which amounts to a lateral distance of 0.92 mm, a two-dimensional image is obtained as shown on Fig. 6.10. This image matches the target object very well.

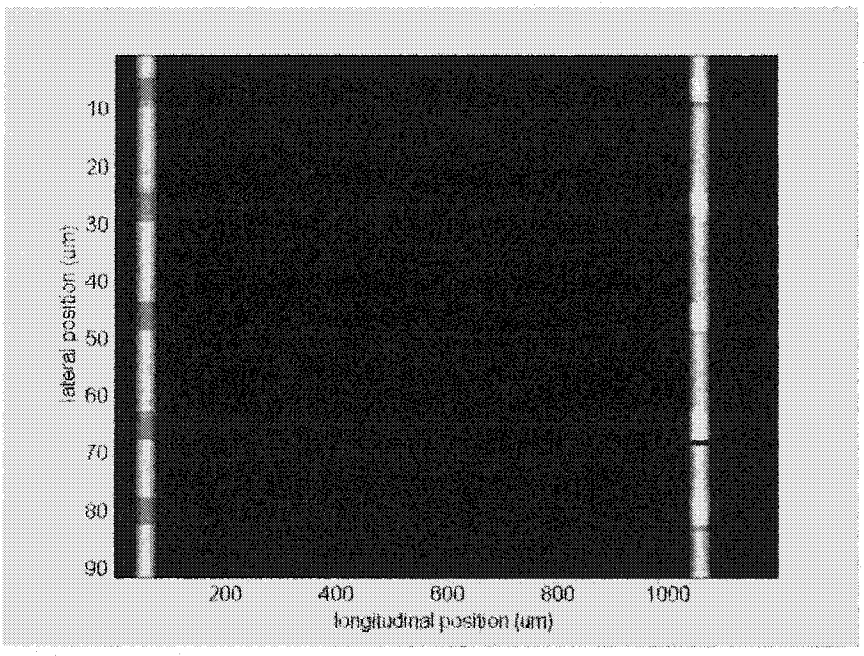


**Figure 6.10** The two-dimension OCT imaging of a grating-like sample

### 6.5 Onion, a natural sample for OCT

The main usage of the OCT technique is to perform non-invasive diagnostic images of biological tissues. Since our source is a SLD with a coherence length of 32.8 μm, we chose a piece of onion as a natural sample with cells size of around 60 μm. Fig.6.11 (a) and Fig.6.11 (b) display the cross-section images of a piece of onion. Fig.6.11 (c) and Fig.6.11 (d) show the results of one longitudinal scan of each of them. The received interference signals are very strong which indicating the images can be believable.

Because the axial resolution of the SLD is 32.8 μm which is close to the size of the onion cells, the precise structures of the cells cannot be imaged very clear. The cell walls along the lateral direction are imaged well while those along the longitudinal direction are missing. This is because the thickness of the cell wall is about 5 μm, much smaller than the lateral resolution of the OCT system. More than three layers of the cells can be distinguished from the images and the size of the cells can be measured in the range of 50 – 70 μm.

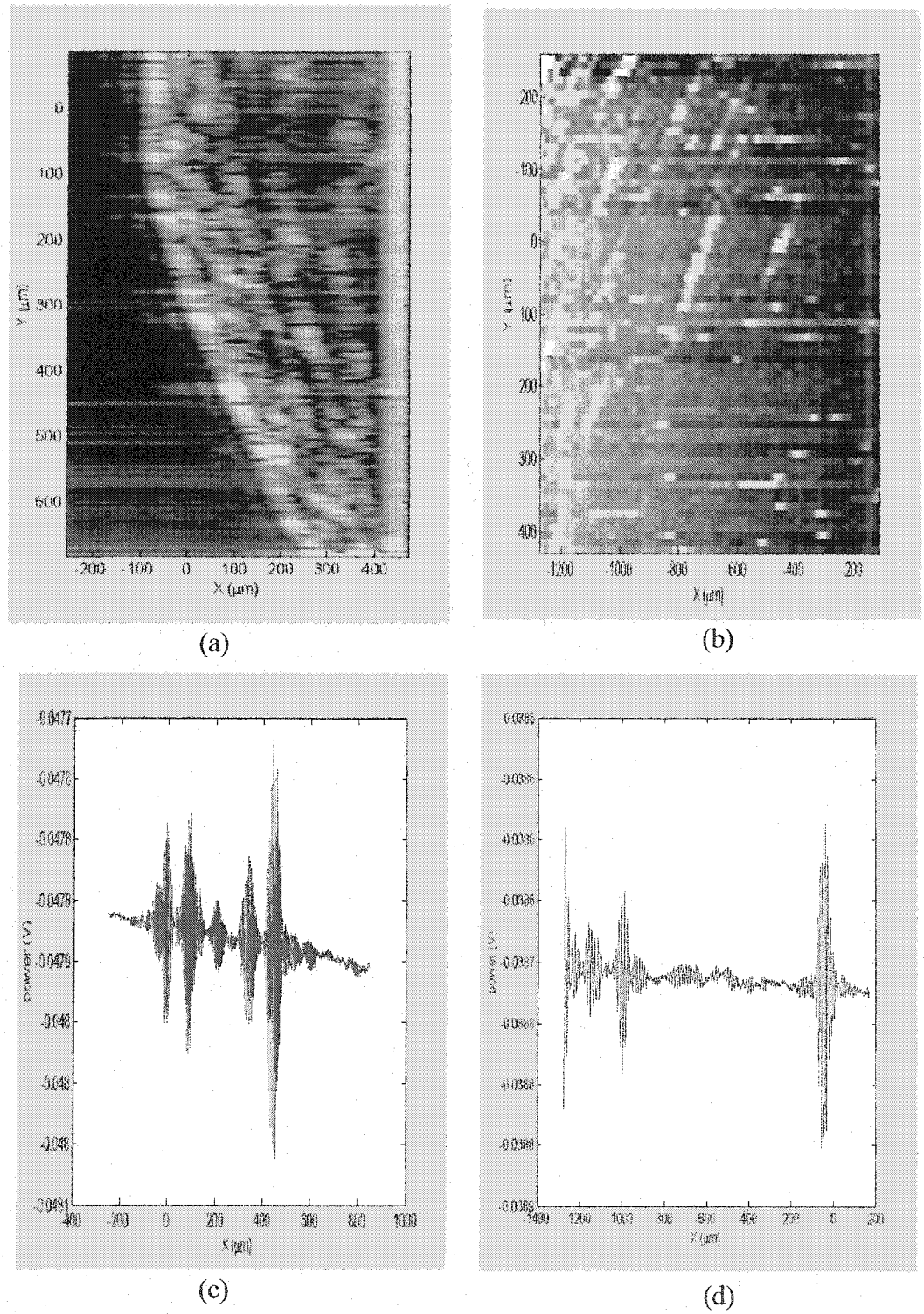


**Figure 6.11** The OCT images of onion

# CHAPTER 7

# EXPERIMENTS OF OCT WITH A WHITE LED

## 7.1 Introduction

White sources have many advantages for OCT because of the inherent broad spectrum. Some groups tried to use halogen lamps as a white source for OCT [23] but the temperature fluctuation of the lamp reduces the quality of the image since it induces fluctuations in the intensity and in the spectra. Therefore, the super bright white light-emitting diode (LED) becomes a promising alternative as a new source for OCT experiments. This chapter reports on the results obtained with this novel approach to OCT.

The selected white LED is a model RL5-W10015 Super-White LED (GaN/InGaN) (Red Line Inc.) which emits an intensity of 10000 mcd, as well as a long lifetime of 100,000 hours when operated under its designed working conditions. Its very low price makes it the cheapest source used for OCT in the world. With this source placed into a specially designed Michelson interferometer, we have undertaken some tomography experiments, including experimental design, characterization of the source, and OCT performances of some real objects.

## 7.2 Fundamental properties of the white source

A light-emitting diode (LED) is essentially a PN junction semiconductor diode that emits light when current is applied. It is therefore very reliable when the current is well controlled. Its measured power output is approximately 1 mw within an illuminating cone of 15°. This measurement was done by fixing the white LED on a rotating stage and detecting the emitted power through a narrow slit at a certain distance. The experimental emission pattern is shown in Fig.7.1.

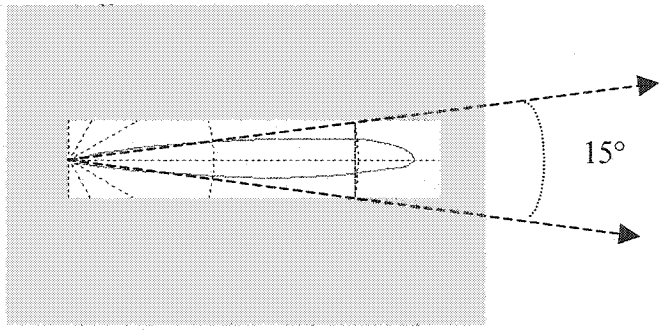


**Figure 7.1** Illuminating cone of a white LED

The working voltage of the white LED was well controlled at 3.54 V as well as the current at 30 mA. Under these conditions, its power dissipation was approximately 100 mW. Its spectrum bandwidth was measured by focusing the beam into a monochromator connected to a computer. The received spectrum obtained with Labview is shown on Fig.7.2. Its spectrum bandwidth ranges between 430 and 800 nm with two peaks at 460 nm and 660 nm. Taken separately, the first and second peaks yield a coherence length of 4.76 μm and 4.26 μm respectively. The combined coherence length should be less than 4 μm. Indeed, we obtained a mean coherence length of about 2 μm. This result will be discussed later.

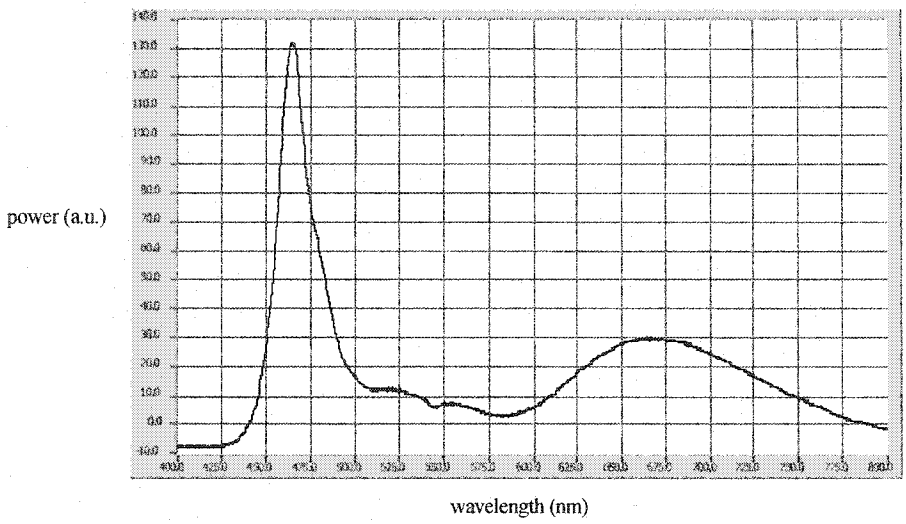


**Figure 7.2** Spectrum bandwidth of white LED

### 7.3 Basic interference characteristics of the white LED

Fig. 7.3 is a schematic diagram of the white LED Michelson interferometer. The white light beam is directed into the interferometer after being collimated. A silicon detector is used to record the interference signals.

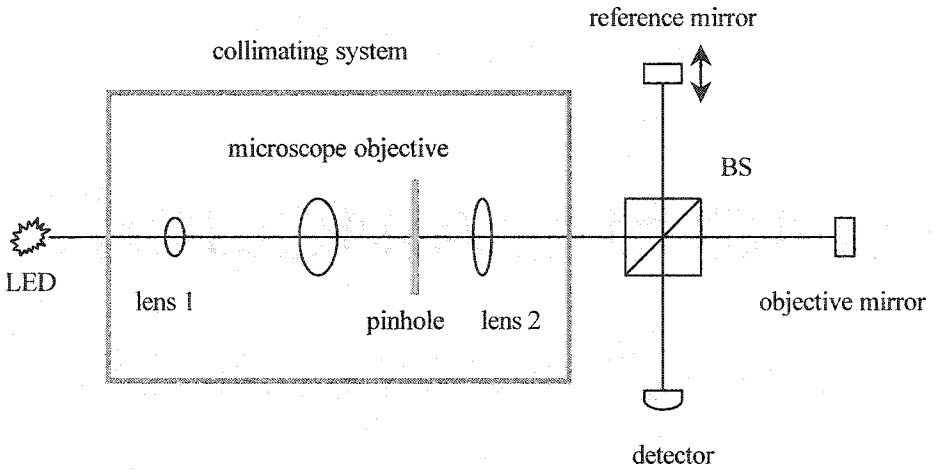


**Figure 7.3** Schematic diagram of the white LED Michelson interferometer

Because the coherence length of the white LED is very small (less than 4 μm), the interferometer must be well aligned at the position where the reference beam and the objective beam are matched. Otherwise, the interference signal will not appear. To simplify the alignment procedure, a Helium-Neon laser beam is used as the optical axis of the system and all other components are aligned related to this optical axis, including the white LED beam. When the alignment of the system is done, the initial interference signal can be observed directly by the naked eye while scanning the reference mirror. Normally, the initial interference fringes appear as colorful, dim parallel lines. At that time, a fine alignment has to be done carefully until the zeroth order fringes are received. Unlike the

infrared source whose zeroth order fringes are just a succession of dark and bright fringes when the reference mirror is displaced, the zeroth order of the white LED is colored. This phenomenon is due to the dispersion induced by the beamsplitter. By dispersion compensation between the two arms, the bright fringe will become white again.

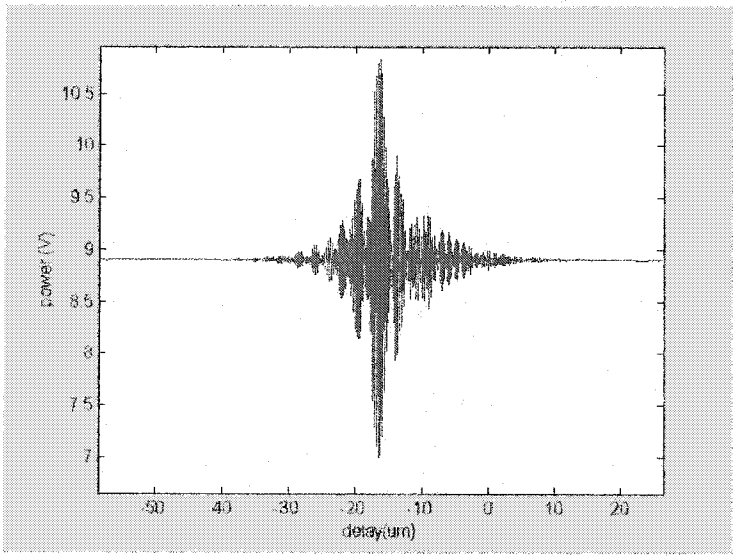


**Figure 7.4** Recorded basic interference signal of the white LED source

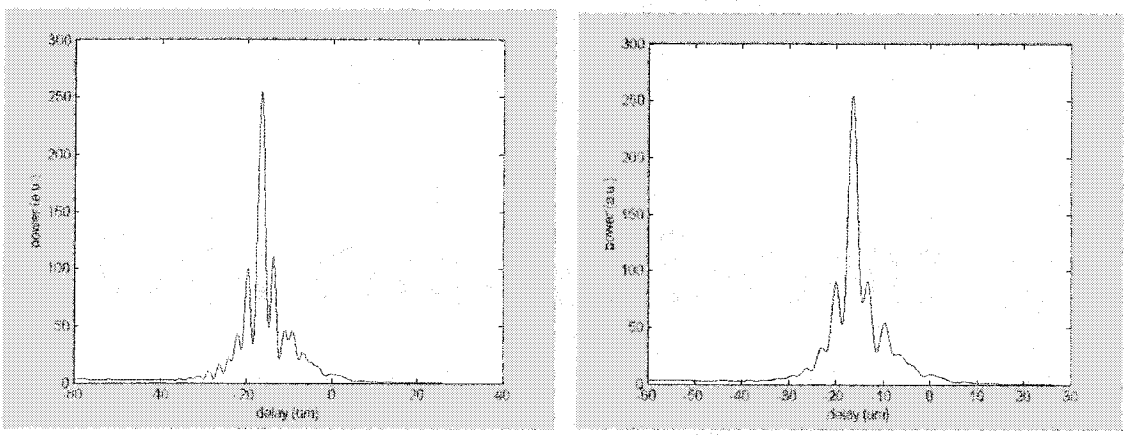

(a) (b)

**Figure 7.5** The envelop of the interference signal after filtering and cutoff

Fig.7.4 shows the recorded interference signal. Its signal-to-noise ratio is 29.8 dB. The useful information of this signal for OCT is the peak intensity of the envelope and the position of the peak. We get this information by filtering and cutting off the signal by software. Fig. 7.5 indicates how it works. Fig. 7.5 (a) shows a filter order of 7 while the cutoff factor is 0.03. The envelop is very close to the original signal and has a coherence length of 2.1 μm. Fig. 7.5 (b) shows a filter order of 7 with a cutoff factor of 0.02. In this case, the main peak becomes larger while the wings decrease resulting in a better contrast image, but its coherence length becomes wider, 2.6 μm.

As a comparison, a halogen lamp was used for the interference experiment with the same experimental setup. The results are shown in Fig. 7.6. We can see that although the spectrum bandwidth of this lamp source is broader than that of the white LED source, the received interference signal is much worse because of the unstability of the lamp.

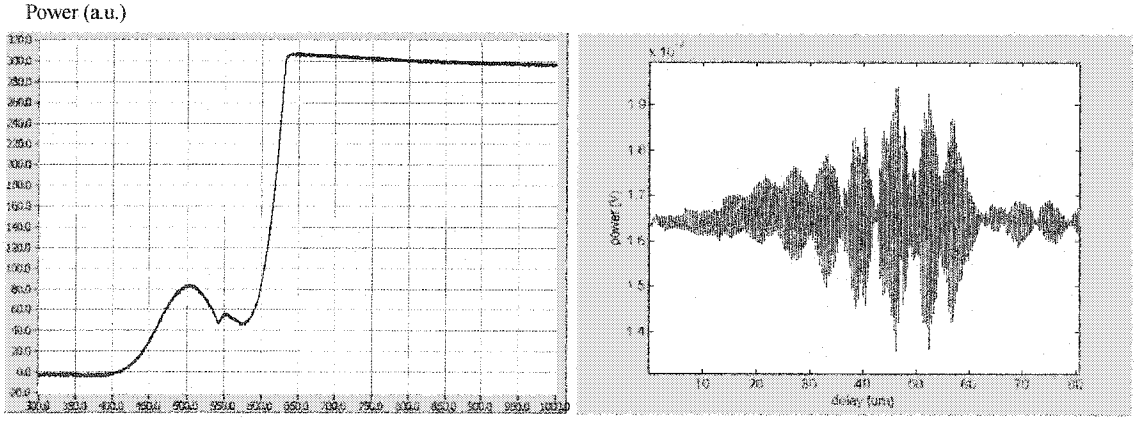


**Figure 7.6** Spectrum and interference signal of a halogen lamp

## 7.4 Experimental setup for OCT with white LED

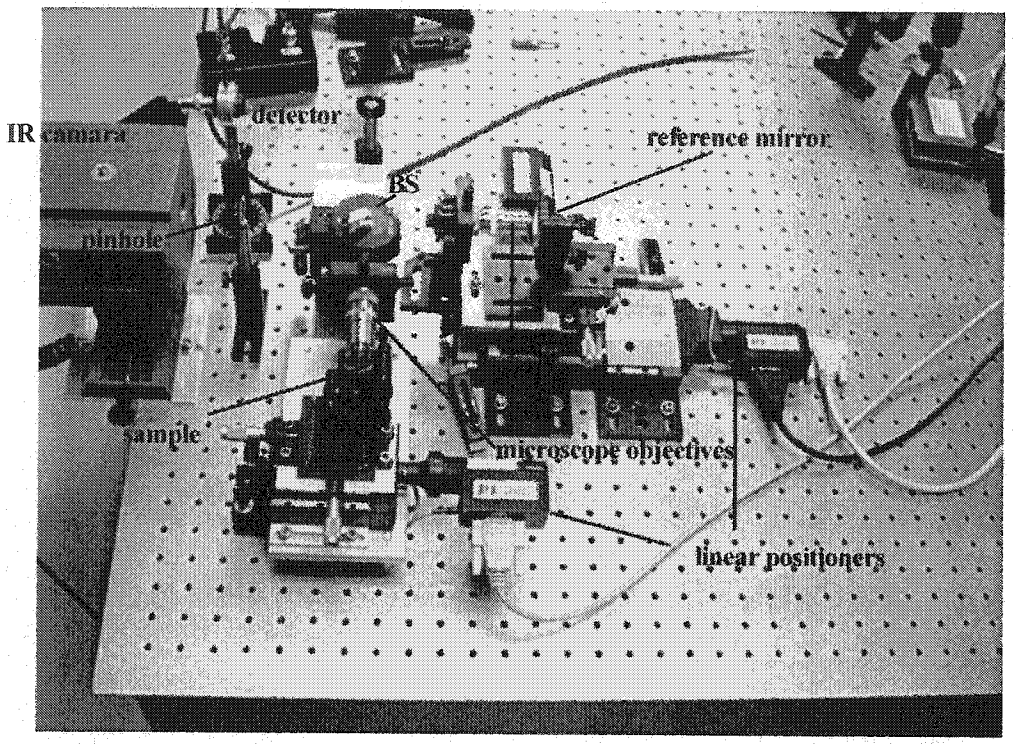


**Figure 7.7** Experimental setup of the OCT with white LED

A power beamsplitter (BS) cube (Newport Optics) is centered in front of a reference mirror which is fixed on a computer controlled linear positioner. An objective mirror is also fixed on another linear positioner for the lateral scanning. Two microscope objectives are placed in each arm to focus these two beams on the mirrors' surfaces and collect the backreflected or backscattered lights back for the interference. The collimated white LED beam is directed onto the beamsplitter where it is divided into two equal intensity beams in the sample and reference arms. A small screen is used to monitor the interference signal that can be watched by eye through a magnifying lens and a silicon photodetector is used to record the interference signal. The computer-controlled linear positioning stage (PI Physik

Instrumente) can move at a very stable speed which is adjustable between 0 and 1.5 mm/s.

The mean difference that distinguishes an OCT setup from a conventional Michelson interferometer is that the sample beam must be focused to a small spot in order to receive the structure information of the sample spot by spot through the longitudinal scanning of the reference mirror. The size of the focal spot determines the lateral resolution of the system. The initial interference signal of the white LED was obtained in the Michelson interferometer configuration, that is without adding the two microscope objectives. In this case, the optical path difference between the two arms is just the linear distance difference from each mirror to the BS. Thus, the zeroth order interference fringe can be observed clearly.

### 7.5 Interference characteristics of OCT system with white LED

To perform optical coherence tomography of a given object, the sample beam must be focused as small as possible, based on the coherence length of the source. Fig. 7.8 illustrates the situation of the sample arm after introducing a microscope objective. In the plot, $f_L$ is the focal length of the objective, and θ is the incidence angle of light on the sample.

The optical path difference between the two arms is:

$$\Delta = \frac{f_L}{\cos\theta} - f_L \tag{7-1}$$

The first order fringe appears when the optical path difference is equal to half the wavelength:

$$\Delta = \frac{f_L}{\cos\theta} - f_L = \frac{\lambda_0}{2} \tag{7-2}$$

for the case of the white LED, the center wavelength is at 560 nm and the focal length of the objective $f_L$ is 4 mm. We obtain:

$$\frac{4\times10^6}{\cos\theta} - 4\times10^6 = \frac{560}{2} = 280(nm)$$

Thus,

$$\cos\theta = 0.99993$$

$$\theta = 0.68^\circ$$

Then, the radius of the zeroth order fringe is:

$$r = f_L \times \tan\theta = 4 \times \tan(0.68^\circ) = 0.047(mm)$$

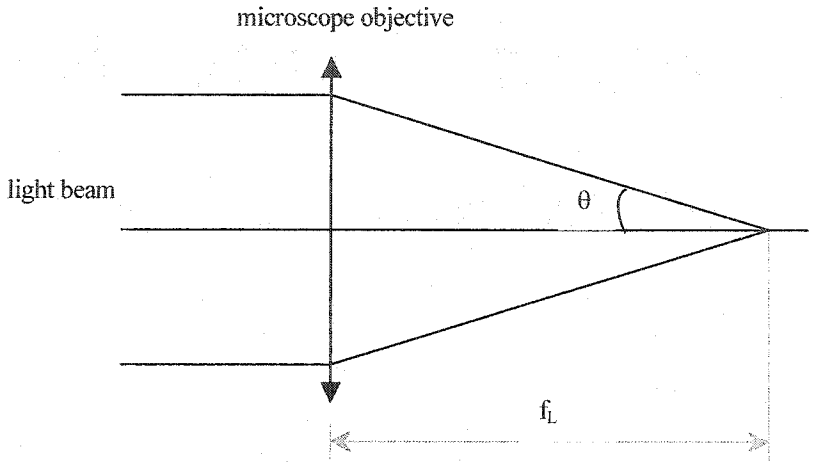


**Figure 7.8** Optical path of the sample arm

This means that the size of the zeroth order fringe is less than 0.1 mm. For white light interference, only the lower order fringes can be seen because the dispersion inside the system can expand the size of the higher order fringes. Then, in the higher order fringe region, the fringes of different wavelengths will mix together and wash each other out. In this situation, the visibility of the lower order fringes is limited to the vicinity of the center of the focal spot. It is impossible to see them due to their small size and dimness.

To solve this problem, another identical microscope objective must be added into the reference arm for optical path compensation. This way, the influence of the factor θ on the optical path difference is canceled. As a consequence, the optical path difference only depends on the linear distance, and the zeroth order interference fringe has the same size as the light beam.

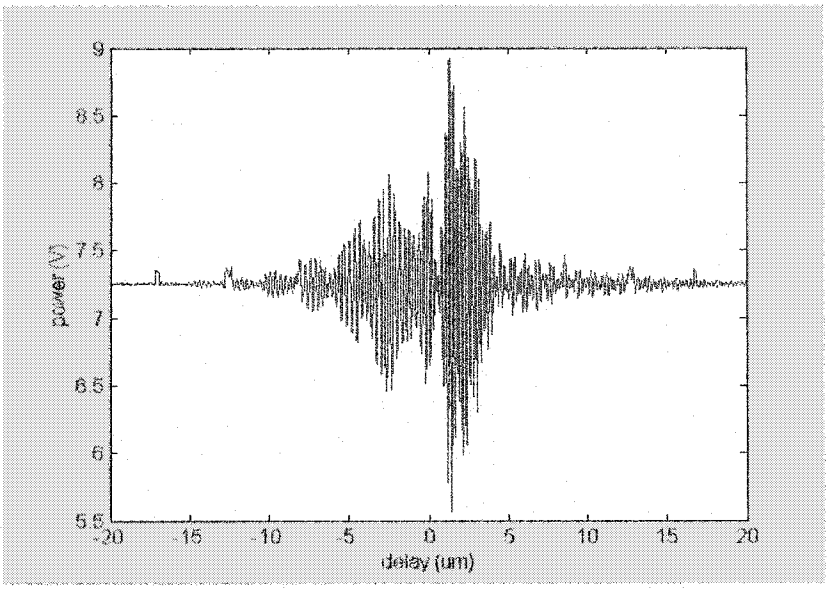


**Figure 7.9** Interference signal detected after putting two microscope objectives in position

Fig. 7.9 shows the interference signal detected after putting the two microscope objectives in position. The signal-to-noise ratio is 27.4 dB. The signal after filtering and cutoff processing is shown in Fig. 8.10. In this plot, (a) shows a filter order of 7 while the cutoff factor is 0.01. The envelope is very close to the original signal and has a coherence length of 2.1 μm. Fig. 8.10 (b) shows a filter order of 3 with the same cutoff factor: the mean peak becomes sharper, and its coherent length becomes 2.2 μm. Fig. 8.10 (c) shows a filter order of 1 with the same cutoff factor. It combines all the peaks into one and gives out the best contrast for the final image. Its coherence length is much larger (9.3 μm), though, which results in a lower resolution.

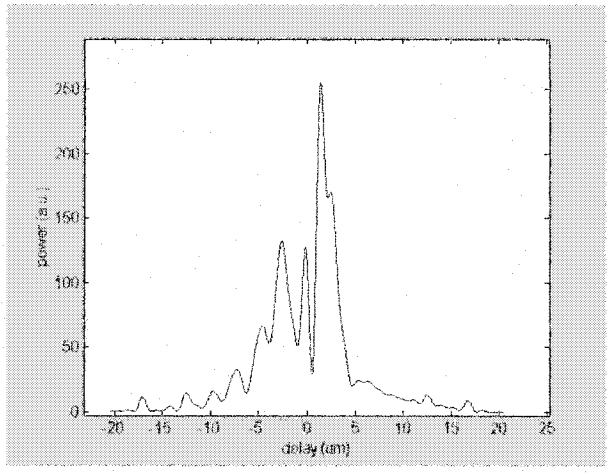


(a)

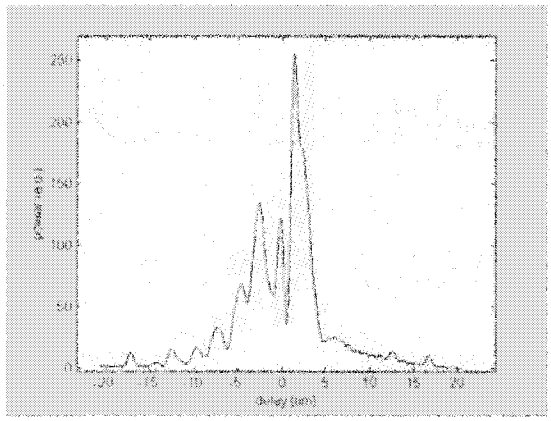

(b)

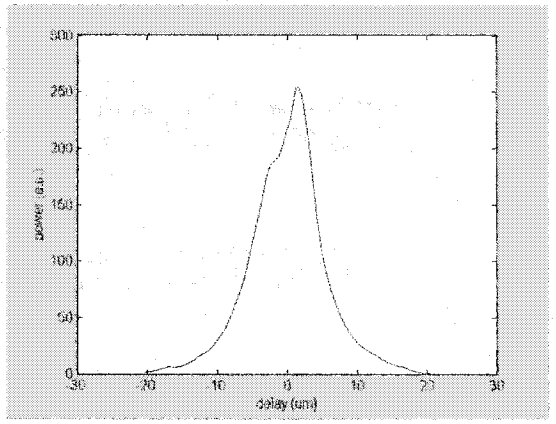


(c)

**Figure 7.10** The envelope of the interference signal with different filter orders and cutoff factors

## 7.6 Measurement of the scanning range

The intensity of the beam will drop down after passing through a microscope objective. This energy drop depends on the numerical aperture value of the objective. Fig. 8.11 shows the intensity as a function of the numerical aperture (NA). The numerical aperture of our setup is chosen to be 0.4.

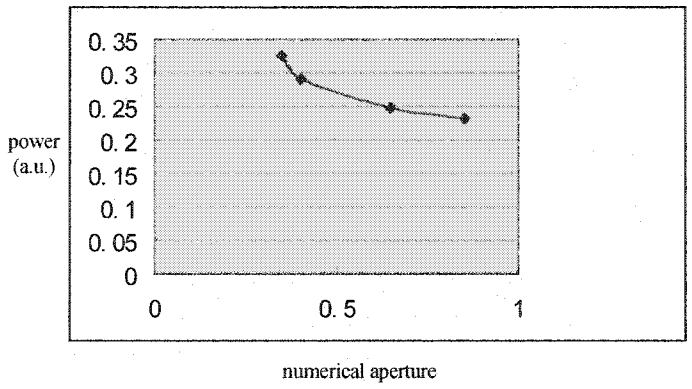


**Figure 7.11** The focal spot intensity vs the NA value of the microscope objective

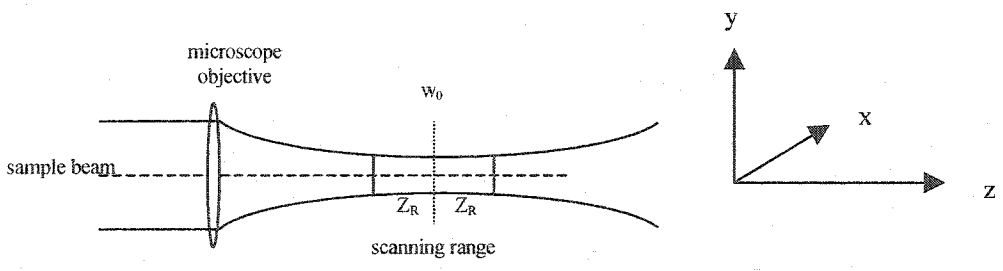


**Figure 7.12** Scanning range of the sample beam

Fig. 7.12 shows the objective arm of the OCT setup. The beam is focused with the microscope objective. The Rayleigh range is the distance between the waist position and the position where the radius of the beam is $\sqrt{2}$ that of the waist. The microscope objective (NA=0.4) can focus the light beam collimated from a white LED to a small spot. The axial scanning range is defined by two Rayleigh ranges on each side of the waist.

In order to measure the axial scanning range, two knife edges were set to obtain a narrow slit which can move in the x direction via a computer controlled positioner and also in the z direction manually. A silicon detector was centered on the focusing spot to record the intensity of the transmitted part of the beam. Fig. 7.13 shows one of these recordings. By measuring the FWHM intensity, we obtained the size $\Delta S$ of the focal spot:

$$\Delta S = S_2 - S_1$$

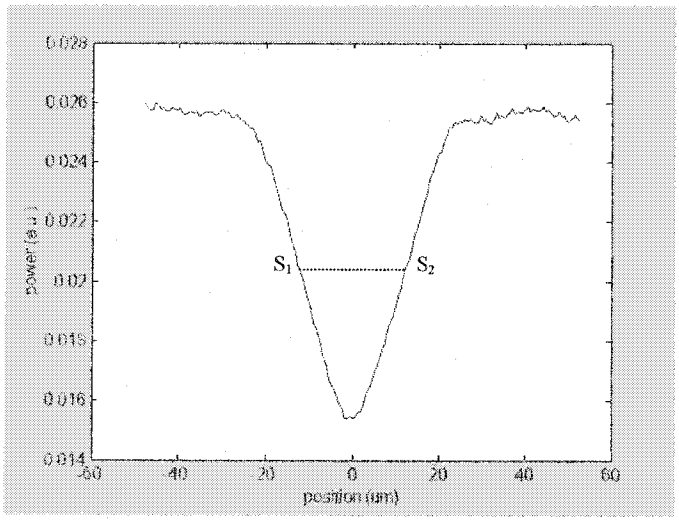


**Figure 7.13** Recorded one focal spot size

By collecting several traces at different positions along the z-axis, the final shape of the focusing beam can be obtained as shown on Fig. 7.14. In this figure, the waist of the beam is 28.5 μm, and the axial scanning range is 145 μm.

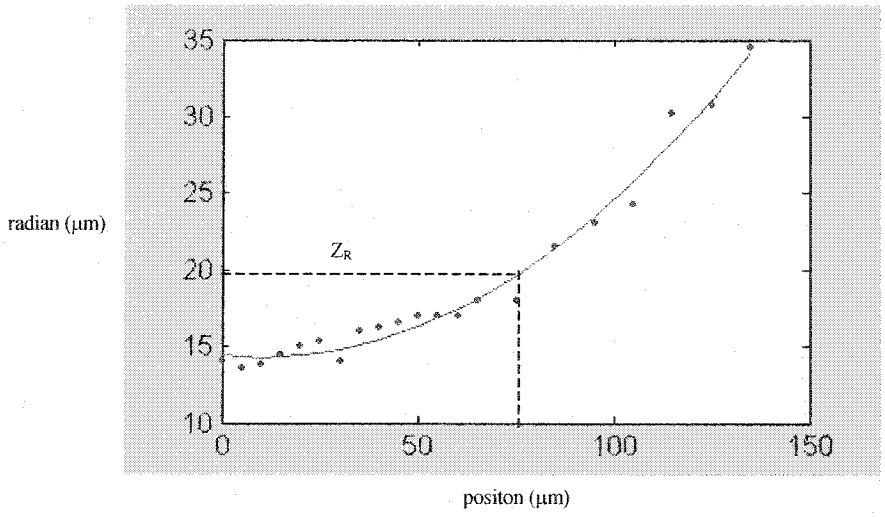


**Figure 7.14** Final shape of the focusing beam – The center of the beam is given by the horizontal axis

### 7.7 Measurement of the actual scanning range of the objective beam

As mentioned in chapter 1, the transverse resolution of an optical coherence tomography image is determined by the size of the focusing spot inside the sample. However, the focusing spot size is inversely proportional to the depth of field of an OCT system. This means that a small focusing spot created by a high numerical aperture (NA) microscope objective will induce a short scanning range. A good OCT setup should have a small enough focusing spot size which leads to a high transverse resolution and also a long scanning range which allows the system to show the details inside the sample deeply.

In our setup, we chose a microscope objective with a numerical aperture (NA) of 0.25 which yields a focusing spot size of ~10 μm and a depth of field of 850 μm for the SLD source. However, the quality of the collimated white LED beam is not as good as that of the SLD source which results in a lower transverse resolution and a shorter depth of field of the system. This needs to be improved in the future when a concentrating lens is introduced into the setup.

In the last section we discussed the depth of field of the white LED OCT setup by calculating the Rayleigh range of the focusing beam. In fact, the actual axial scanning range of an OCT setup is usually not the same as that given by the Rayleigh range of the beam. Therefore, we need to measure the actual scanning range of this system since it is a very important parameter that determines the choice of the samples. This has been done by recording the interference signals while moving the objective mirror along the z-axis as shown in Fig. 7.15. The zero position is the place where the two interference beams have

their optical paths matched and give an interference signal with the maximum amplitude. We moved the sample mirror back and forth around the null position along the longitudinal axis while recording the interference traces. The results show that the amplitudes of the interference signals decrease in both sides of the null position. This indicates that our setup has a maximal scanning range of 120 μm in air.

This short range is primarily determined by the NA of the microscope objective and the choice of a small spot size for higher lateral resolution. Various tradeoffs could be made. A longer scanning range OCT system will be studied by careful choice of the microscope objective and improvement of the collimating quality of the white LED beam.

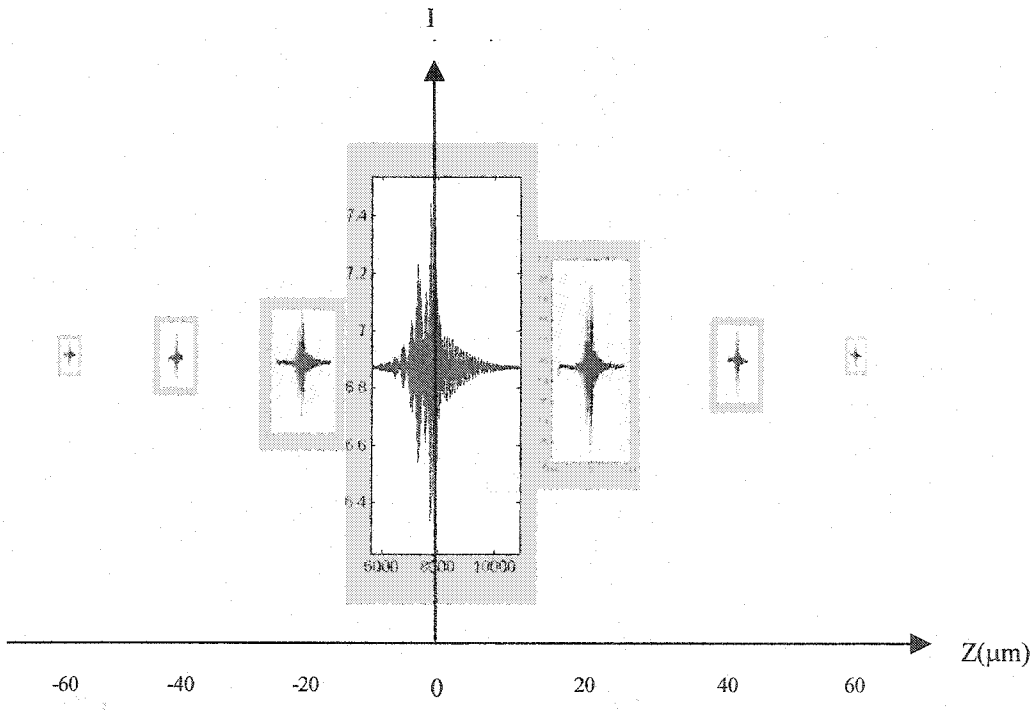


**Figure 7.15** Real scanning range of the OCT setup

## 7.8 OCT experimental results with the white LED on some real samples

So far, all of the experimental results showed above have been obtained with a mirror fixed at the end of the sample arm instead of a real object. This is necessary at the beginning of the alignment of the setup since the reflection coefficient of the mirror is almost 100 percent. This produces an interference signal that is much stronger than the noise floor. This signal can be read by the detector even when the system is not very well aligned. This initial interference signal is very important for the fine alignment of the system. When it is aligned, the mirror can be replaced by a sample.

(1) Sample 1 – a small piece of plastic tip

We have found that the scanning range of this OCT system is only about 120 μm in air. It is better to make the sample thinner than this range. The first sample we used was a piece of plastic tip with many cut lines on its rear surface as indicated on Fig. 7.16.

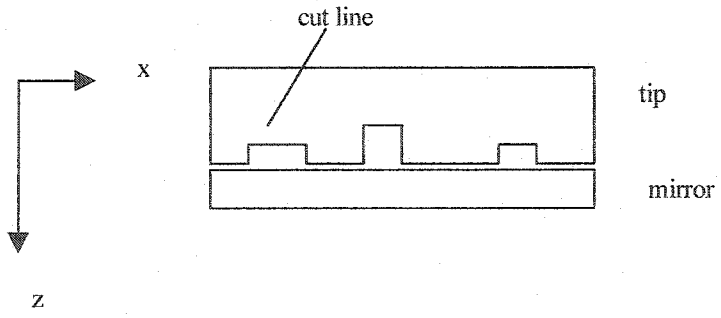


**Figure 7.16** Structure of the first sample

The longitudinal scanning range of the reference mirror was set from 9000 to 25000 counts which represents 136 μm, and the scanning speed was set at 1.7 μm/s. The lateral scan consisted of 50 steps of 10 μm each. Fig. 7.17 shows the results for this sample. Fig. 7.17 (a) shows the cross-sectional structure of the sample. The left bright line is the tip surface, and the second is the mirror. Between the twos, there are some cut lines close to the mirror. The thickness of the tip is 58 μm. Fig. 7.17 (b) shows a single longitudinal scan displaying a longitudinal resolution of about 7.3 μm.

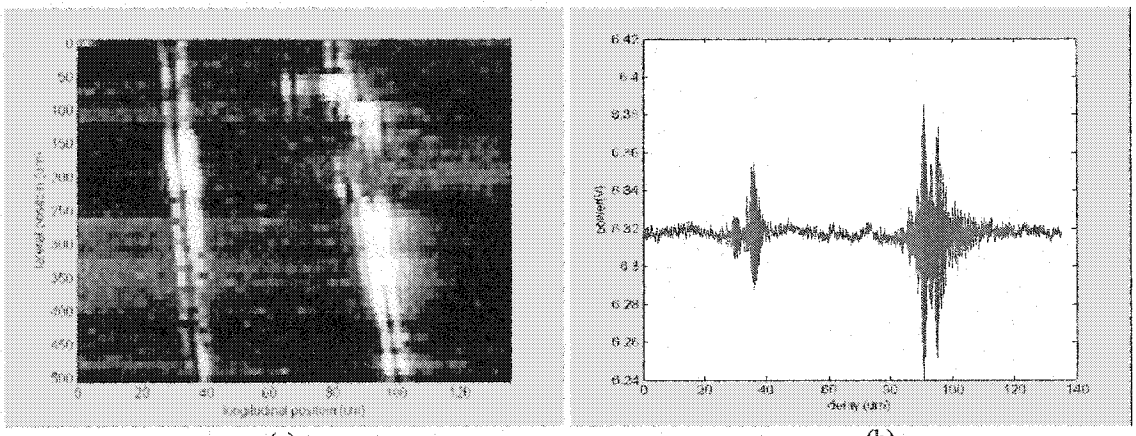

(a) (b)

**Figure 7.17** Results of the OCT scanning of the first sample

(2) Sample 2 – A small piece of plastic film with paint marks

The second sample we investigated was a piece of plastic film with some painted lines on its surface. This time, the cross-sectional image shows the mirror surface, the film surface, and the paint layer. We can clearly separate the paint layer from the film. The longitudinal scan of the reference mirror was set from 2000 to 12000 counts which amounts to 85 μm, and the scanning speed was set at 1.7 μm/s. The lateral scan was 50

steps of 10 μm each. Fig. 7.18 (a) shows the cross-section of the sample. The bright line on the left is the film surface with the paint on, and the second is the mirror. The thickness of the film is 30 μm. The thickness of the paint layer is 4.8 μm. Fig. 7.18 (b) shows a single longitudinal scan indicating that the longitudinal resolution is about 3.7 μm.

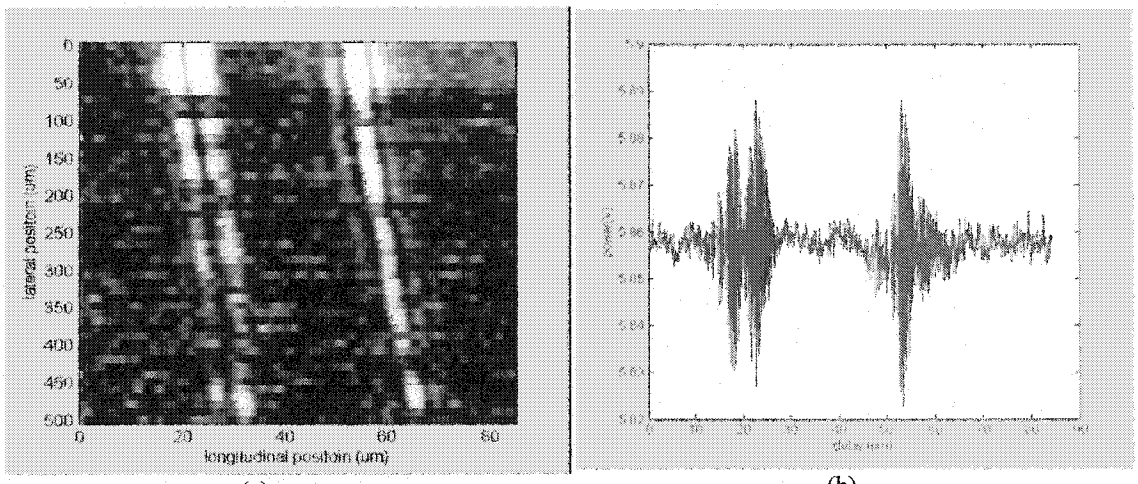


(a) (b)

**Figure 7.18** The results of the OCT scanning of the second sample

(3) Sample 3 – A laboratory made multi-layer sample

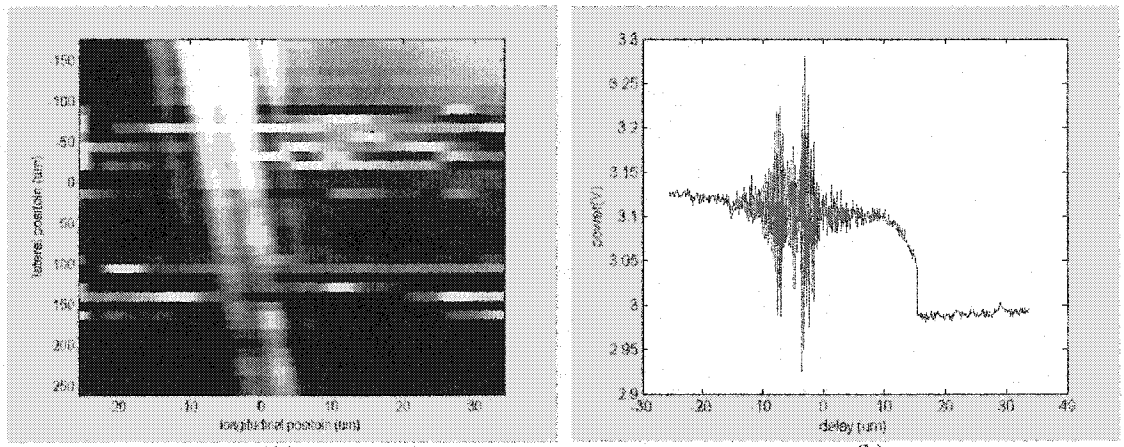


(a) (b)

**Figure 7.19** Results of the OCT scanning of the four layer sample

A four layer (photoresist) sample was made specially for the OCT imaging. The first layer at the bottom is a 10 μm thick SPR 220 followed by a second layer of 5 μm thick LOR10A material. The third layer is another 10 μm thick SPR220, and on the top, there is another 5 μm thick LOR10A. Unlike the two plastic samples which are transparent to visible light, this sample is yellow in color, and its index of refraction is higher. In Fig. 7.19, two layers clearly appear. The distance between these two layers is 5.3 μm. This result is in good agreement with the thickness of the top layer, and the longitudinal resolution is about 3.7 μm. The second interference signal is produced by the reflection from the layer below, which is a 10 μm thick SPR 220. However, the interference signal produced by the deeper layers is missing. This is due to two reasons. First, the reflection coefficient of the material is so low that the signal-to-noise ratio is poor; second, the attenuation and the absorption of the photoresist materials decrease the intensity of the reflected light that the interference becomes too weak to be detected.

(4) Sample 4 – Mica

Mica ($KAl_2(AlSi_3O_{10})(OH)_2$) is a transparent mineral which consists of many thin layers in the range of 0.5 to 24 μm [24]. These layers partly reflect incident light so that interference signals can be obtained. OCT can therefore be a good way to detect the internal structure of mica.

OCT images of a piece of mica have been obtained in the Lab with two sources. The first one is the infrared SLD source which emits a broadband spectrum at a center wavelength of 1545 nm with a FWHM bandwidth of 32 nm (as mentioned in Chapter 6).

This source shows the internal structure of the mica sample in the hundred micron scale since its axial resolution is around 32.8 μm. We were not able to distinguish within a distance of less than 32 μm. However, the well-collimated and much powerful light beam resulted in a longer depth of field, 800 μm, such that various constituents of the sample on that scale could be observed.

The second source was the white LED introduced earlier. This source revealed the internal structure of the mica sample in the tens of microns scale since it has a much higher axial resolution. The limitation is that the scanning range of this source is due to the collimating quality of the beam and the selection of the microscope objective as we have explained before (see 7.7).

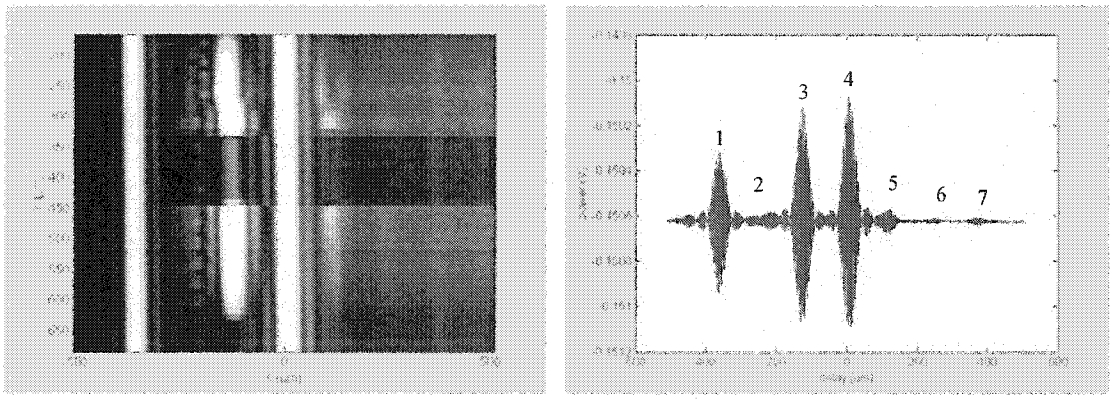


(a) (b)

**Figure 7.20** Experimental results of the mica sample by the SLD source

Fig. 7.20 shows the experimental results of the mica sample by the SLD source. The longitudinal scanning range of the reference mirror was set from -60000 to 60000 counts which represents 1 mm, and the scanning speed was 1.7 μm/s. The lateral scan consists of 50 steps of 10 μm each. Fig. 7.20 (a) shows the cross-section image of the sample. Fig. 7.20 (b) shows a single longitudinal scan which indicates its axial resolution is about 38.7 μm.

There are seven layers have been illustrated in Fig. 7.20 (b). The distances between two of them range from 98.5 to 142.6 μm, but only three layers can be seen clearly in the OCT image. The thickness of each layer is about 54 μm. We can see that from 280 to 450 μm on the lateral direction in Fig. 7.20 (a), after a ~ 10 μm small shift, the middle layer becomes weaker. This indicates that in this region, the surface of the layer is not as flat as its neighbours and that the scattered light reduces the intensity of the reflection light.

In fact, the layers shown in this image can be resolved into many thinner layers if the axial resolution of the source is increased. The first layer in this image has been resolved into six layers using the white LED source, as shown in Fig. 7.21.

This time, the longitudinal scanning range of the reference mirror was within 100 μm, with a scanning speed of 1.7 μm/s also. The lateral scan consists of 150 steps of 10 μm each. Fig. 7.21 (a) shows the cross-section image of the sample. Fig. 7.21 (b) shows the result of a single longitudinal scan showing that its axial resolution is about 1.6 μm. Six layers can be resolved in the image with a thickness for each of about 4.5 μm. This demonstrates that the white LED source is capable of detecting the internal structures much

better. By increasing the depth of field of this source, many detailed structures can be displayed clearly and deep inside the sample.

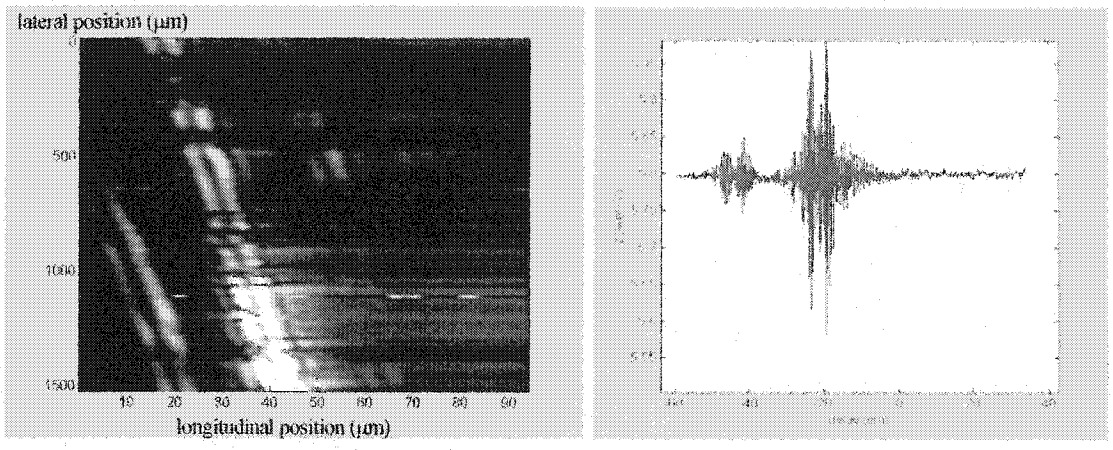


(a) (b)

**Figure 7.21** Experimental results of the mica sample by the white LED source

# CHAPTER 8

# SHORT PULSE OCT

## 8.1 Introduction

Many groups are working towards the development of new OCT systems that have much higher resolution and longer depth of field in order to display the internal structure of the tissues much more clearly and deeply. The primary properties for the suitability of a light source for OCT are wavelength, coherence length, brightness, and intensity stability. SLD sources are popular since they are capable of providing sub-20-μm resolution imaging at several wavelengths, but are limited to optical powers of a few milliwatts. The ultra-short pulse mode-locked Ti:Sapphire laser is also a strong candidate as a source for future developments in OCT because this laser has many advantages, such as high resolution, large depth of field, high signal-to-noise ratio, and easy coupling into the optical fiber. In our laboratory, a sub-10 fs Ti:Sappire laser will soon be available. A new OCT setup based on a fiber-optic Michelson interferometer will be designed and built in the near future.

An important problem for ultra-short pulse lasers is that they have very high peak power and can burn living tissue easily. Therefore, ultra-short pulse induced ablation of tissue needs to be studied.

In this chapter, some research results on this topic are being reviewed. The threshold of the optical breakdown has been found to depend on pulse duration, object properties, number of shots, laser power, and so on. This information is essential for the use of ultra-

short pulse lasers on biological tissue.

## 8.2 High resolution OCT imaging using ultra-short pulse laser

As a laser, the ultra-short pulse laser can easily provide high peak power output, up to many hundreds of killowatts. This property enables the Ti:Sapphire ultra-short pulse lasers to take OCT images of the internal microstructure of biological tissues much deeper than the SLD sources. High irradiance can also provide an interference signal with a very high dynamic range. For Ti:Sapphire ultra-short pulse lasers, the signal-to-noise ratio exceeding 90 dB is easy to get.

The second important property of the Ti:Sapphire ultra-short pulse laser is that it can provide the OCT system with a very high resolution. The Ti:Sapphire ultra-short pulse laser in our laboratory emits pulses at a center wavelength of 800 nm with a FWHM spectral bandwidth of 46 nm. The coherence length of this laser pulse is then (1-8)

$$L_c = 0.44 \times \frac{\lambda_0^{\,2}}{\Delta\lambda} = 0.44 \times \frac{800 \times 800}{46} = 6.1\mu m$$

This coherence length value is much lower than that of the SLD source at 32.8 μm.

The third advantage of a Ti:Sapphire ultra-short pulse laser is that the pulses can travel for a long distance without losing much power and that it is much easier to couple light into a single-mode optical fiber compared to an SLD.

As said before, OCT performs high resolution images with interferometric traces obtained with low coherence sources. The lower the coherence of the source, the higher the resolution. For a low coherence Ti:Sapphire ultra-short pulse laser, efforts must be spent to

broaden its bandwidth to an order of 100 nm or more, which translates into a pulse duration of 10 femtoseconds or less. One solution consists in using a shorter Ti:Sapphire crystal and introducing chirped mirrors. At the present time, this is not available in the laboratory but will be in the near future.

The Ti:Sapphire laser produces ultra-short laser pulses by the Kerr-lens effect inside the crystal itself. It is then known as self-mode locking. This effect fixes the phase relationship between the existing modes propagating inside the laser cavity in order to create an ultra-short pulse. However, dispersion inside the cavity broadens the laser pulse during its round-trip. The main dispersion comes from the crystal itself so that we need to include second order, third order, fourth order dispersion and so on. These dispersion are proportional to the crystal length. A shorter crystal can produce shorter laser pulses but at the expense of power. To achieve a sub-10 femtosecond ultra-short laser pulse, a 2-mm-long crystal rod is necessary [13][21].

The dispersion in the laser cavity must be well compensated for producing an ultra-short pulse. A prism pair is needed to compensate the second order dispersion provided by the crystal rod since it has a negative second order dispersion. However, this prism pair also introduces high order dispersion that broadens the pulse duration. So, the prism material must be selected to compensate the second order dispersion and at the same time introduce as low as possible high order dispersion into the cavity. Jiangping Zhou et al. [21] developed a 8.5 fs pulse Ti:Sapphire laser by operating it near the zero second- and third-order dispersion condition, such that, only the fourth-order dispersion affected the pulse duration. They used a 2-mm-long Ti:Sapphire crystal rod (0.23% doped) and a pair of

fused-silica prisms. The corresponding spectrum had a bandwidth of 151 nm, centered at 856 nm. The calculated coherence length Lc is (1-8)

$$L_c = 0.44 \times \frac{\lambda_0^{\ 2}}{\Delta\lambda} = 0.44 \times \frac{856 \times 856}{151} = 2.1 \mu m$$

Double-chirped mirrors are another device for compensating the high order dispersion of the prism pair that is the most important limitation for ultra-short pulse generation. I. D. Jung et al. proposed a self-starting 6.5-fs pulse Ti:Sapphire laser [10]. They used a 2.3-mm-long Ti:Sapphire crystal rod (0.25% doped), a pair of fused-silica prisms in combination with double-chirped mirrors. The double-chirped mirrors were highly reflective with the potential for dispersion compensation over the spectral range of the reflection. The corresponding spectrum had a bandwidth of 140 nm, centered at 795 nm. The calculated coherence length $L_c$ is

$$L_c = 0.44 \times \frac{\lambda_0^{\ 2}}{\Delta\lambda} = 0.44 \times \frac{795 \times 0795}{140} = 1.99 \mu m$$

Consequently, sub-2 μm OCT system is possible by using a sub-10 fs Ti:Sapphire ultra-short pulse laser as the source. A laser source also allows to probe biological tissues much deeper than a normal SLD.

### 8.3 The principle of ultra-short pulse laser ablation on tissues

Ultra-short pulse lasers are capable of delivering optical energy within a very limited time duration. Ablation of tissue can easily happen because the ultra-short pulse may cause a plasma-mediated optical breakdown inside the tissue. This plasma-mediated optical breakdown is very powerful with the potential for minimal damage to the tissues, high ablation precision and efficiency. Therefore, ultra-short pulse laser has been considered to be a powerful tool for the tissue ablation. Research on this topic including both theoretical and experimental work has been carried out such that the principle of laser induced optical breakdown (LIOB) is understood much better than before. This section provides an overview of the results.

Ultra-short pulse laser ablation is performed by focusing the laser beam onto the surface of the tissue that is being excised. The power density of the ultra-short pulse can reach a very high value in the focal point of the beam resulting in the ionization of atoms and molecules. This effect provides the initial electrons for the optical breakdown in tissue. These electrons or free charge carriers absorb energy from the radiation field in order to provide a high enough density of conduction electrons and then, by collision ionization, the microplasmas that are formed lead to the avalanche breakdown when the critical plasma density is reached.

The expansion of the generated microplasmas launches a stress wave, the shock wave, into the surroundings. The propagation of the shock wave inside the tissue is an important factor for the determination of the precision of the optical ablation. Research results indicate that the shock wave can cause cell damage of the surrounding tissue during the

process of plasma-mediated tissue ablation. The shock-wave range was observed and recorded in some experiments indicating that the initial shock-wave pressure was very high. However, the pressure decayed very rapidly while the shock-wave propagated through the medium at a high velocity. The shock-wave pressure generated by a femtosecond pulse decays faster resulting in a considerably smaller shock-wave radius. For instance, a femtosecond pulse provides a 20 μm shock-wave radius instead of a 200 μm radius for the picosecond pulse. The volume of the surrounding tissue affected by a picosecond pulse is approximately 1000 times bigger than that affected by a femtosecond pulse [25].

Another important secondary effect, the creation of the cavitation bubble, occurs during the further expansion of the microplasmas. The final size of the cavitation bubble determines the characteristics of laser spots within the tissue and the degree of the contiguous effects. The cavitation bubble is another main reason that causes the cell damage and limits the accuracy of the ablation. The femtosecond pulse induced cavitation bubble effect is found to be much smaller than that of a picosecond pulse. The maximal cavitation bubble diameter, provided by a 100 fs laser pulse in the human corneal tissue, was about 45 μm compared to a 260 μm diameter caused by a 60 ps laser pulse [25].

For plasma-mediated tissue ablation, the shock-wave and the cavitation bubbles may be considered as the main collateral tissue effects that were found as the parameters to limit the precision of the ablation. The range affected by the ultra-short pulse is proportional to its pulse duration.

**8.4 The theoretical analysis of ultra-short pulse laser ablation on tissues**

A theoretical analysis which describer the dependence of the LIOB threshold on the pulse duration was given by F. H. Loesel et al. [26]. The temporal behavior of the free electron density N(t) is described by:

$$\frac{\partial N}{\partial t} = \overline{\beta} N(t) - \delta N(t) \qquad (8\text{-}1)$$

where, $\overline{\beta}$ is the rate parameter for the reduced avalanche ionization, and δ for the electron diffusion. $\overline{\beta}$ is defined by:

$$\overline{\beta} = \beta - \gamma N(t) \qquad (8\text{-}2)$$

with the rate parameter β for avalanche ionization and γ for inelastic collisions without generation of free electrons. The avalanche parameter β depends primarily on the incident intensity I. Substituting μ (t)= 1/N(t), one gets,

$$\frac{\partial \mu}{\partial t} + (\beta - \delta)\mu(t) - \gamma = 0 \qquad (8\text{-}3)$$

This equation has the following general solution:

$$\mu(t) = c(t)\exp\left[-\int_0^t (\beta - \delta)dt'\right] \qquad (8\text{-}4)$$

The initial condition is written as $\mu$ (0) = $1/N_0$, and $c_0 = 1/N_0$, where $N_0$ is the initial electron density. The general solution is obtained as:

$$N(t) = \frac{\exp \int_0^t (\beta - \delta) dt'}{\frac{1}{N_0} + \gamma \int_0^t \exp \left[ \int_0^t (\beta - \delta) dt'' \right] dt'} \qquad (8\text{-}5)$$

Assume a laser pulse with a duration $\tau$ and a constant intensity $I_0$, the parameter $\beta$ can then be approximated by:

$$\beta = \begin{Bmatrix} \eta I_0 & for \quad 0 \le t \le \tau \\ 0 & elsewhere \end{Bmatrix} \qquad (8\text{-}6)$$

where $\eta$ is called ionization probability and is expressed in units of $(J/cm^2)^{-1}$. By limiting the calculations to the case $0 \le t \le \tau$, the threshold fluence $E_{th}$ of LIOB is finally obtained as:

$$\eta E_{th} = \frac{s}{2} + \sqrt{\left(\frac{s}{2}\right)^2 + \frac{\tau}{2\tau_c}} + \frac{\tau}{\tau_d} \qquad (8\text{-}7)$$

where [27]

$$s = \ln \frac{N_{th}}{N_0} \approx 18$$

with threshold electron density $N_{th}$. The time constant $\tau_c$ for inelastic collision is $1/ N_{th} \gamma$ and $\tau_d$ for diffusion is $1/\delta$. The ionization probability of the biological materials $\eta$ was calculated as 15.7 $cm^2/J$, 10.3 $cm^2/J$ for human teeth and corneal tissue, respectively, and $\eta$ = 9.8 $cm^2/J$ for the bovine brain.

To study the principle of the shock wave decay within the tissue, one can consider the shock waves as discontinuities in pressure, density, particle velocity, and internal energy. If one uses $\Delta p$ to denote the pressure amplitude, $\rho_0$, the density of water, $U_s$, the shock velocity and $U_p$ the particle velocity, the relationship between them is [28]:

$$\Delta p = \rho_0 \cdot U_s \cdot U_p \qquad (8\text{-}8)$$

Rice and Walsh found that the equation of state of water could be used as an approximation for soft tissue, that is:

$$U_s = U_o + 2.11 \times U_p \qquad (8\text{-}9)$$

Where $U_o$ is the sound velocity. Combine them to obtain:

$$\Delta p = \frac{\rho_0}{2.11} \cdot (U_S^{\,2} - U_S \cdot U_0) \qquad (8\text{-}10)$$

However,

$$\Delta p = C/r^2, \tag{8-11}$$

where r is the propagation distance, C represents a parameter of the shock wave strength. Then we can obtain the shock wave decay velocity as a function of the propagation distance:

$$U_S = \frac{U_o}{2} + \sqrt{\left(\frac{U_o}{2}\right)^2 + \frac{2.11 \times C}{\rho_0 r^2}} \tag{8-12}$$

### 8.5 The experimental studies of the ultra-short pulse laser ablation

Many experiments in which the ultra-short laser pulse damage thresholds of some typical hard and soft tissues have been done according to different laser pulse durations, laser repetition rates, laser beam sizes, and the number of laser pulse shots. Three different methods were proposed to find out the value of the laser fluence at the ultra-short pulse damage thresholds. These methods include: observing the surface modification of the experimental materials after the laser irradiation, checking the change in the scattered light from the cavitation bubbles and jets of ablated materials, and looking for the evidence of the shock wave inside the interference fringe patterns by means of a Mach-Zehnder interferometer. The experimental work also addressed the pressure and the radial position of the shock-wave as a function of the time delay, laser pulse duration as well as the propagation distance.

There are three experimental methods for finding the ablation threshold of hard as well as soft tissues. The first method is the most frequently used and direct one. It consists of observing any surface modification of the tissue by using the scanning electron microscope or the optical microscope after the irradiation by the ultra-short laser beams [30-31]. Hard tissue such as human tooth was tested by this method and the results were acceptable. Since the sample surface was finely polished before the test, it is possible to find any evidence of surface modification induced by the laser irradiation directly.

The second method was used for the soft tissues, like human corneas and bovine brain, when the surface modification by the laser irradiation cannot be observed clearly [26]. The ultra-short laser pulse is focused on the tissue surface while a collinear CW probe beam is

also focused to the spot being monitored. The tissue surface is observed with a high-resolution optical microscope. When the measurements begin, the energy of the laser pulses is set above the threshold value and the probe beam is scattered by cavitation bubbles and jets of ablated materials. Then, continuously decrease the laser fluence so that the scattered light becomes lower. The damage threshold is the value observed when the intensity of scattered light sharply decreases due to the lack of inducing cavitation bubbles and ejected materials.

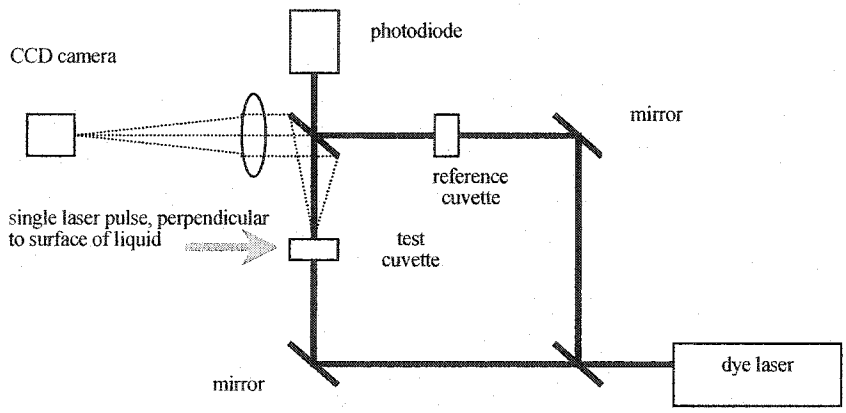


**Figure 8.1** Mach-Zehnder interferometer for shock wave measurement

The third method is much more sensitive than the other two ones. It introduces a Mach-zehnder interferometer that can monitor the shock waves generated by the ultra-short pulse [31]. As a close approximation of soft tissue ablation, water ablation was studied by this method instead of real soft tissue. The experimental setup is shown in Figure 8.1.

The laser source was an 80 MHz pulse train with a maximum 1 mJ/pulse output power

at 800 nm. Its pulse duration could be continuously changed from 130 fs and up. The probe beam is split into two paths using a 50/50 beam splitter. One of the beam paths contains a test cuvette, filled with purified water. Another reference cuvette is placed in the other path of the interferometer to equalize the two beam paths. The two beams are recombined in the other beam splitter to generate fringe patterns. The ultra-short pulse is incident normal to the water surface of the test cuvette. If the laser pulse fluence is below the threshold value, the system will show many parallel-line fringes. Ablation on the water surface occurs when the laser pulse fluence is above the threshold value. Spherical waves will be generated when the pulse energy hits the surface of the water. Then, the stress wave causes the water density to change resulting in fringe shifts on the interferograms. The ablation threshold was defined as the fluence that just creates an observable spherical acoustic wave.

Shock waves are one of the main phenomena in the ablation process. Because the power density of the ultra-short laser pulses is very high, microplasmas are generated during the process of laser-tissue interactions. The fast expansion of the heated plasma launches a stress wave into the surroundings, the shock wave. The propagation of the shock wave inside the tissue is known to be an important effect that determines the precision of the optical ablation. Many experiments have been completed on the characteristics of the shock wave during the ablation process.

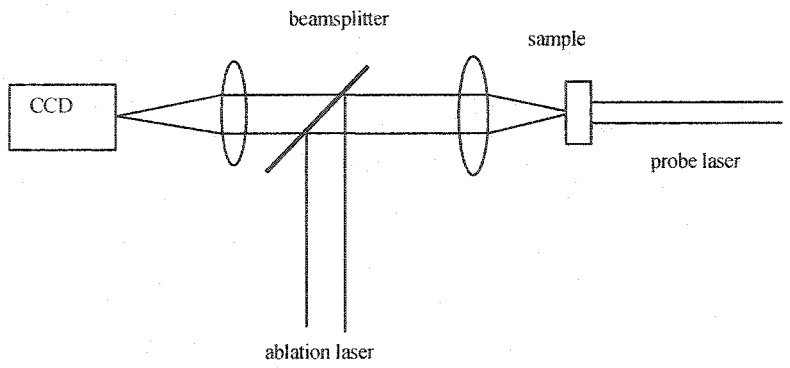


**Figure 8.2** Experimental setup for monitoring the shock wave

J. P. Fischer et al. have taken photographs of shock waves on the corneal tissue surface [28]. Their experimental setup is shown in Fig 8.2. Slices of fresh bovine cornea and brain tissue were used for the experiments. The probe beam is an amplified 30 ps IR pulse laser focused on the sample surface. Another synchronized visible pulse laser illuminates the focal spot on the tissue surface as a "flash light" for the time-resolved photography. A CCD-camera is positioned in the plane conjugate to the optical breakdown plane to take photographs. This way, the propagation of the shock wave in the corneal tissue was recorded. This experimental setup can monitor the shock wave, the ablation channel, the surface wave, and the remaining crater.

Another experiment for observing the characteristics of the shock wave was done by B. M. Kim et al. [31]. Their experimental setup included a Mach-Zehnder interferometer. The ultra-short laser pulse was focused normal to the water surface with its energy above the tissue damage threshold. The stress wave generated on the water surface caused the

water density to change resulting in fringe shifts in the interferograms. This change was recorded with a CCD camera. The experimental results showed that the property of the shock wave varied according to different laser pulse durations.

### 8.6 The biological tissue responses as a function of pulse dose

Femtosecond pulse laser ablation on tissue has been shown to have many advantages, such as high-precision, lower laser fluence, and minimal collateral tissue damage. Ablation threshold of the pulse has been studied and the threshold of optical breakdown has been shown to have an approximately square root dependence on the pulse duration. Other researches focused on how the threshold fluence of the optical breakdown varies with the laser pulse duration, the repetition rate, the beam size and the number of shots.

Fig. 8.3 a-c show the laser fluence at the threshold of LIOB as a function of pulse duration obtained on the surface of human enamel, human corneal tissue, and bovine brain tissue, respectively [26]. The solid and dashed lines in the figures were obtained by a theoretical calculation. The laser fluence at the LOIB threshold decreases as the pulse duration becomes shorter. The laser fluence is defined as the laser beam energy of one beam spot per unit area ($J/cm^2$). Assume two laser pulses with the same fluence, one is in the pulse duration range of fs, the other one is in the range of ps. Because the fs laser pulse can deliver the optical energy within a much shorter period, the tissue has to withstand a much higher optical power during the pulse duration. So, a laser pulse will damage the tissue when the pulse duration is of fs range although it is safe when the pulse duration is in the ps range. That is why the fluence threshold of the ultra-short pulse laser decreases as the laser pulse duration becomes shorter.

The fluence at threshold is calculated using the measured values of single-pulse energies over the size of the focal spot. In this experiment, single-pulse energies were obtained from the average output power of 1-kHz pulse trains. The plotted data represent

mean values of the threshold levels averaged over 3-5 tissue samples.

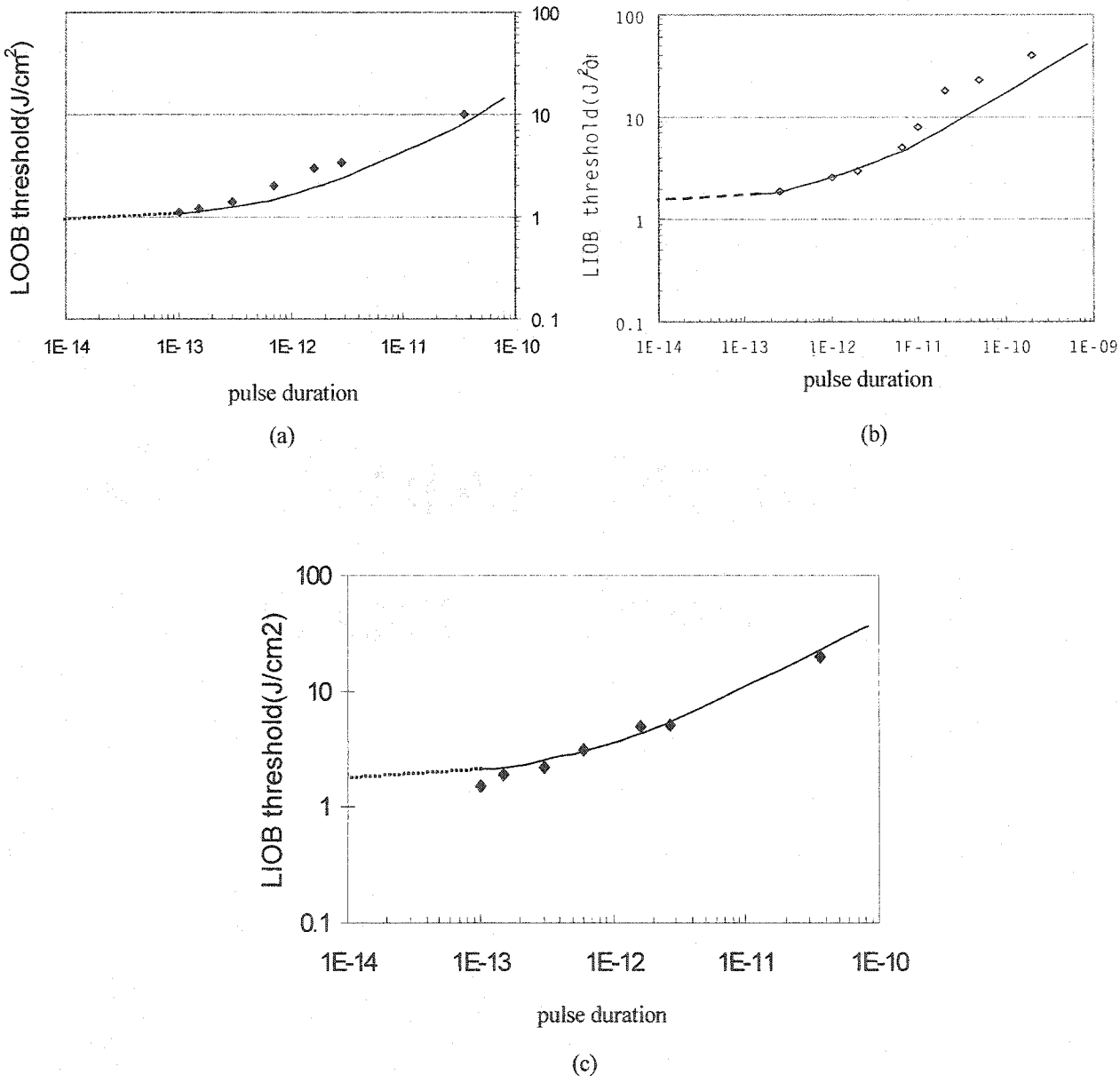


**Figure 8.3** The threshold of LIOB as a function of pulse duration on human enamel, human corneal tissue, and bovine brain tissue

For human enamel, the threshold was found to be about 10 J/cm$^2$ at a pulse duration of 35 ps. At shorter pulse durations, the LIOB threshold decreases. The threshold was measured to be about 1.1 J/ cm$^2$ when the shortest available pulses with a duration of 100 fs were applied to the tissue. For human corneal tissue, the threshold is also decreasing with shorter pulse durations. At pulse widths of 200 ps, an energy density of 40 J/ cm$^2$ is needed for LIOB, whereas the threshold is lowered to about 2.0 J/ cm$^2$ in the case of pulses with 350-fs duration. Decreasing threshold levels are also observed in bovine brain tissue. In this experiment, a fluence of about 20 J/ cm$^2$ at pulse widths of 35 ps was measured for LIOB threshold. For 100-fs pulses, the threshold was found to be about 1.5 J/ cm$^2$. Based on these experimental results, the relationship between the ablation thresholds of the tissue and the laser pulse duration was established. Namely that the ablation threshold increases as the square root of pulse duration for pulses longer than ten picoseconds.

Femtosecond laser-tissue interactions on hard tissue were studied with a 130 fs 800 nm laser using various repetition rates and beam sizes [30]. In these experiments, the effective damage threshold was defined as the laser intensity below which no surface modification could be observed with an optical microscope after 1000 shots. Fig. 8.4 shows the change with the number of shots. Here, the beam size was fixed at 175 μm and the repetition rate was 1 kHz. Threshold values for 10, $10^3$, and $10^4$ shots were measured. The effective damage threshold decreased from about 0.79 to 0.52 J/cm$^2$ as the exposure time became longer. For small beam sizes, the threshold does not seem to be affected by the repetition rate over the range observed. As the beam size becomes larger however, repetition rate effects became stronger and a high rate resulted in a significant lower threshold value. Also, the threshold decreased as the number of shots increased. These results indicate that

effective ultra-short pulse damage thresholds at high repetition rates depend on beam size, repetition rate, and exposure time.

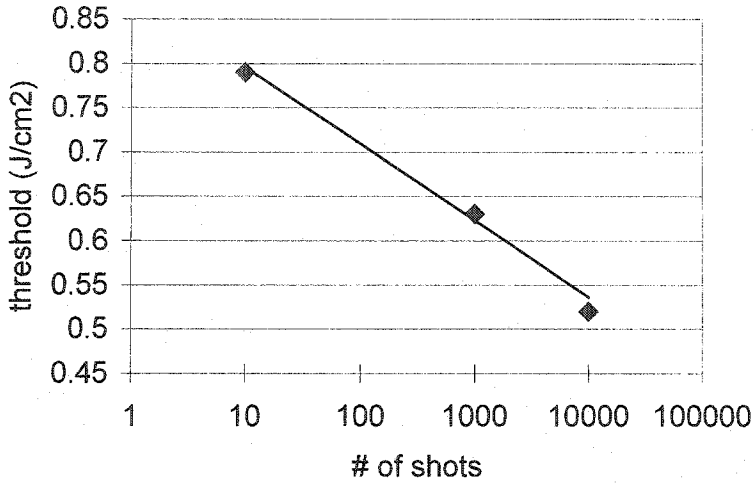


**Figure 8.4** Ablation threshold decreases with number of shots [30]

Ablation craters were created on the dentin surface using fluences at twice the threshold values for 130 fs, 1 ps, and 10 ps pulses [31]. For all pulse durations a limited crater depth was observed. Fig. 8.5 shows the measured depth of the ablation craters as a function of the number of shots for 130 fs - 1ps pulses. It is clear that the final crater depth improves with longer pulse duration. This may be caused by additional thermal ablation associated with longer pulse irradiation, as evidenced by melting at the crater walls and edges.

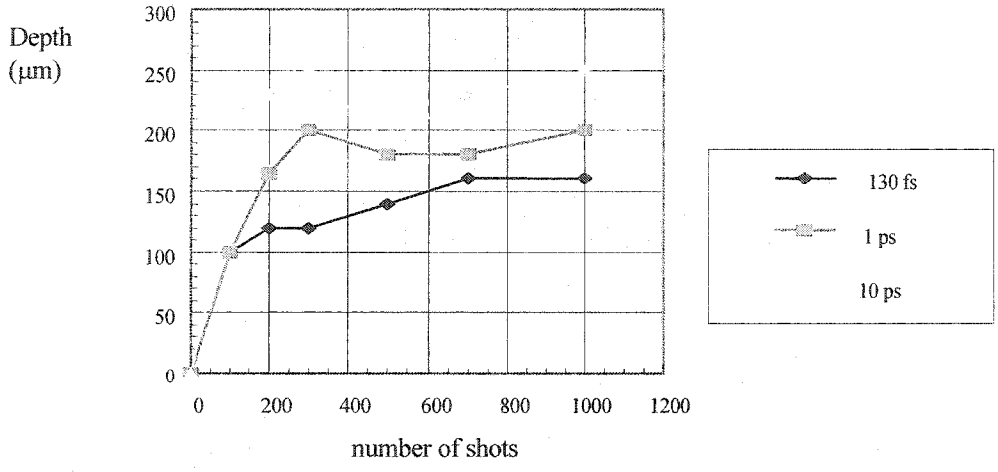


**Figure 8.5** Ablation threshold vs number of shots

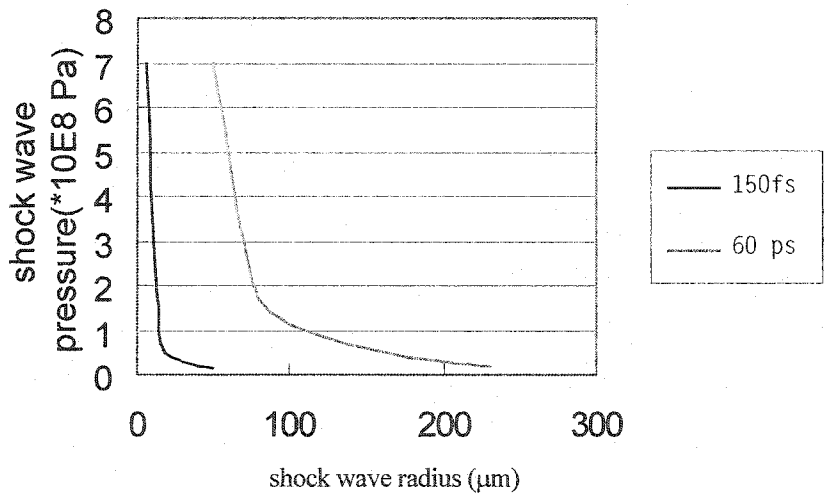


**Figure 8.6** Measured shock-wave pressure vs the shock wave radius

Fig. 8.6 shows the measured shock-wave pressure change as a function of the shock wave radius in water for 150 fs and 60 ps laser pulses [25]. The pressure decreased very rapidly while the shock wave propagated inside the material. Femtosecond laser pulses were found to produce a significant smaller shock-wave effect range compared to picosecond laser pulses. The volume of tissue affected by the shock wave was estimated by means of an assumed isotropic propagation of the shock wave. The range of shock wave was defined as the point when its pressure decreases below $3\times10^{7}$ Pa (at low pressure, the accuracy of this method is limited). For femtosecond optical breakdown, the shock wave affected a volume of approximately $4 \times 10^{-5}\,mm^3$, while for picosecond pulses, the volume was approximately 1000 times longer ($V=4 \times 10^{-2}\,mm^3$).

# CONCLUSION

This work reported on implementations of OCT that performed high resolution cross-sectional tomographic images of various biological and non-biological materials. We have demonstrated a Michelson interferometer OCT system which is suitable for an infrared light source, and another system based on a Linnik microscope which operates with a super bright white LED source. An in-house data acquisition and scanning control program has been developed for signal processing.

A commercial semiconductor broadband source was employed for one set of experiments. The results presented in this thesis showed that the signal-to-noise ratio of the system was in the 41.3 dB range and its longitudinal resolution was measured to be 32.3 μm for an 850 μm axial scanning depth. The lateral resolution was about 10 μm. These characteristics are typical for this kind of configuration. This implementation was necessary as a first step towards higher performance system. Cross-sectional images have been obtained with this setup for many samples including a grating, an onion peel, and mica. They have revealed interfaces inside the samples on the tens of micron scale.

A new higher performance implementation was then developed. A measured 1.6 μm longitudinal resolution has been obtained by introducing a white LED as the source of another OCT system. This is very close to the best result obtained anywhere so far at 1.1 μm. It has provided additional structural information by resolving the monolayers obtained with the infrared SLD source into at least 6 thinner layers. Another interesting phenomenon was evidence for system dispersion induced by the beamsplitter. It was observed clearly as

a rainbow effect in the interference fringes.

Given the success obtained so far, further developments for this research are planned. The limit on the lateral resolution of the white LED OCT system will be improved by collimating the traveling beam even better. A condenser lens will be employed in the future to provide a narrower and more powerful parallel beam that will focus to a much smaller spot while keeping a longer depth of field.

The dispersion of the system will be reduced by introducing dispersion compensation elements. We will examine the possibility of developing an instrument to characterize the dispersion of some materials precisely, such as laser rods and crystals.

A fiber-based interferometer in conjunction with an ultra-short pulse Ti:Sapphire laser will be assembled for even higher resolution cross-sectional tomographic images. We also expect to go much deeper inside biological tissues. A Ti:Sapphire laser will be built using a 2-mm-long crystal with chirped mirrors providing sub-10 femtosecond laser pulses, and hence a bandwidth of the order of 100 nm or more. Pulse dispersion effects and dispersion compensation in the fiber interferometer will be studied and corrected with appropriate optical elements. An important component of future work will be to investigate biological tissue and material responses as a function of source wavelength, pulse duration and pulse dose. Data acquisition and scanning control programs will be developed to acquire three dimensional (3-D) tomographic images and fast scanning approaches will also be investigated. New geometries will be proposed and performance tradeoffs will be evaluated with the aim of obtaining a high performance design. This optical tomography activity

complements nicely the work done in ultrasound and impedance tomography done at École Polytechnique.

## REFERENCES


1. E.Hecht, Optics (1974)
2. Drexler W, Morgner U,Kaertner FX, Pitris C, Boppart SA, Li XD, Ippen EP, Frjimoto JG. In vivo ultrahigh resolution optical coherence tomography. Optical Letters vol. 24, 1221 (1999)
3. Joseph M. Schmitt, Optical coherence tomography (OCT): A review, IEEE Journal of Selected Topics in Quantum Electronics 5, 1205 (1999)
4. J.W.Goodman, Statistical Optics New York, NY: John Wiley Sons: 1985
5. Brett E.Bouma, G.J.Tearney, Handbook of optical coherence tomography, Marcel Dekker, Inc. 2002
6. David Huang et al, Optical Coherence Tomography, Science, vol 254, 1178 (1991)
7. A.F.Fercher, O.K.Hitzenberger, W.Drexler, G.Kamp, and H.Sattmann, In vivo optical coherence tomography, Amer. J. Ophthalmol., vol. 116, 113 (1993)
8. Qishan Wang, Guofu Chen et al, Experimental study on broadband KLM Ti:Sapphire femtosecond laser pulses, ACTA PHOTONICA SINICA, vol. 29 No.3, 204 (2000)
9. Chang Yongmao, Ultra-short optical pulse generation from a $Cr^{4+}$-doped YAG tunable solid-state laser, Ph.D. thesis, Génie Physique Department, École Polttechnique de Montréal, 1999
10. D.E.Spence, P.N.Kean, and W.Sibbett, 60-fsec pulse generation from a self-mode-locked Ti:Sappire Laser, Optics Letters Vol. 16, No. 1, 42 (1991)
11. K.Naganuma and K.Mogi, 50-fs pulse generation directly from a colliding-pulse mode-locked Ti:Sappire laser using an antiresonant ring mirror, Optics Letters Vol. 16, No. 10, 738 (1991)
12. C.Huang, H.C.Kapteyn, J.W.Mcintosh, and M.M.Murnane, Generation of transform-limited 32-fs pulses from a self-mode-locked Ti:Sappire Laser, Optics Letters Vol. 17, No. 2, 139 (1992)
13. A.Rundquist, C.Durfee, Z.Chang, G.Taft, E.Zeek, S.Backus, M.M.Murnane, H.C.Kapteyn, I.Christov, V.Stoev, Ultrafast laser and amplifier sources, Appl.Phys. B 65, 161 (1997)

14. R.L.Fork et al, Compression of optical pulses to six femtoseconds by using cubic phase compensation, Optical Letters 12, 483 (1987)
15. J.P.Gordon and R.L.Fork, Optical resonator with negative dispersion, Optics Letters Vol. 9, No. 5, 153 (1984)
16. B.E.Lemoff and C.P.J.Barty, Cubic-phase-free dispersion compensation in solid-state ultrashort-pulse lasers, Optics Letters Vol. 18, No. 1, 57 (1993)
17. R.L. Fork, O.E. Martinez, and J.P. Gordon, Negative dispersion using pairs of prisms, Optics Letters Vol. 9, No. 5, 150 (1984)
18. M.T.Asaki, C.Huang, D.Garvey, J.Zhou, H.C.Kapteyn, and M.M.Murnane, Generation of 11-fs pulses from a self-mode-locked Ti:Sappire Laser, Optics Letters Vol. 18, No. 12, 977 (1993)
19. A.F.Fercher et al, Optical coherence tomography-principles and applications, Reports on progress in Physics, 66, 239 (2003)
20. Zhongping Chen, Optical Coherence Tomography, University of California, Irvine
21. Jianping Zhou, Greg Taft, et al, Pulse evolution in a broad-bandwidth Ti: Sapphire laser, Optics Letters, vol.19, 1149 (1994)
22. J.D.Jung, F.X.Kartner, et al, Self-starting 6.5-fs pulses from a Ti:Sapphire laser, Optics Letters, vol.22, 1009 (1997)
23. Takao Fuji, Marriko Arakawa, Toshiaki Hattori, and Hiroki Nakatsuka, A white-light Michelson interferometer in the visible and near infrared regions, Review of Scientific Instruments Vol. 69, No. 8, 2854 (1998)
24. P.K.Mukherjee, D.Chakravorty, Growth of silver nanowires using mica structure as a template and ultrahigh dielectric permittivity of the nanocomposite, Indian Association for the Cultivation of Science, 2002
25. T,Juhasz, F.H.Loesel, R.M.Kurtz, C.Horvath, J.F. Bille, and G. Mourou, Corneal refractive surgery with femtosecond lasers, IEEE Journal of Selected Topics in Quantum Electronics, V5(4) 902-908 (1999).
26. F.H.Loesel, M.H.Niemz, J.F.Bille, and T.Juhasz, Laser-induced optical breakdown on hard and soft tissues and its dependence on the pulse duration: experiment and model,

IEEE Journal of Quantum Electronics, V32(10) 1717-1722(1996)

27. N.Bloembergen, Laser-induced electric breakdown in solids, IEEE.J.Quantum Electron, Vol.QE-10, 375 (1974)
28. J.P.Fischer, T.Juhasz, J.F.Bille, Time resolved immaging of the surface ablation of soft tissue with IR picosecond laser pulses, Appl. Phys, A64 181-189(1997)
29. M.H.Rice, J.M.Walsh, J.Chem. Phys. Vol.26, 824 (1957)
30. B.M.Kim, M.D.Feit, A.M.Rubenchik, E.J.Joslin, J.Eichlez, P.C.Stoller and L.B.Dasilva, Effects of high repetition rate and beam size on hard tissue damage sue to subpicosecond laser pulses, Applied Physics Letters V.76 (26) 2000 4001-4003
31. B.M. Kim, M.D.Feit, A.M.Rubenchik, E.J.Joslin, J.Eichlez, P.C.Stoller and L.B.Dasilva. influence of pulse duration on ultrashort laser pulse ablation of biological tissues, Journal of Biomedical Optics 6(3), 332-338 (2001)

# APPENDIX A

## THE LASER CAVITY ALIGNMENT

The following is a basic alignment procedure for the laser cavity. During this alignment procedure, a careful cleaning procedure must be done before each of the optical components is put into position. First of all, place the translation stage along the center of the optical table at about 16° with respect to the table edge. Then direct the pump beam (5 W in the TEM00 mode) along the axis of the stage at a 4-inch beam height. Fine adjustments are required to make sure that the beam is as horizontal as possible and exactly along the centerline of the rail. Then, mark a spot on a far target where the pump beam hits. Next, place the mode-matching lens (L) and the first curved mirror ($M_1$) in their locations one after another, while watching the marked spot to be sure no deviation of the beam occurs during the translation of each of them. The astigmatism correction angle of 8° must be maintained between the pump beam and the normal to $M_1$. Put the Ti:Sapphire crystal in a position such that the pump beam is incident on its center at the Brewster angle for minimum reflection loss. Insert the second 10-cm radius curved mirror ($M_2$) and let the beam hit it just at the center. Let $M_2$ retro-reflect the beam and then, insert the output coupler (O.C.) into position. The O.C. should retro-reflect the residual pump beam exactly. Now, rotate the mirror $M_2$ until it is parallel to the first curved mirror $M_1$. The end high reflector ($M_3$) is then added and aligned to retro-reflect the residual pump beam. At this point, initial CW lasing can be achieved. Fine alignments have to be performed to superimpose the two beam spots on the first curved mirror. Then, slightly adjust each component of the cavity to maximize the output. Once 600 mw CW lasing is obtained, the cavity has been well aligned.

# APPENDIX B

## GENERATION OF THE ULTRA-SHORT PULSE

See appendix A for the laser alignment procedure. Finely adjust the components of the lasing cavity to maximize the round $TEM_{oo}$ mode output power. Insert the first prism (fused silica, apex angle 69.06±0.25°) by grazing a bit of the Ti:Sapphire laser beam off the apex of the prism. Make sure the reflection from and transparent through the prism beams are leveled exactly. Rotate the prism and stop it at the minimum deviation of the beam. Place the O.C. into the beam and retro-reflect the beam for lasing. Optimize the lasing power by moving the curved mirrors and crystal rod, adjusting the end mirrors. Then insert the second prism in location and also make sure it is in the minimum deviation location. Retroreflect this beam with an O.C. mirror until lasing is achieved. Translate the two prisms fully into the beam and optimize power by adjusting the TEM00 mode for maximum output. The following steps will get us the femtosecond pulses. Monitor the spectrum of the laser by means of a spectrum analyzer and an oscilloscope, then detect the output with a fast photodetector. Translate the second curved mirror further from the crystal slowly, stop it at the edge of the stable region where the output power changes very quickly. Slightly move the two prisms out from the beam until many competing spectra appear on the oscilloscope. Now, turn on the 60 Hz vibrator to shake the end flat high-reflect mirror. Move the first prism and the second curved mirror very slowly while watching the changes in the spectra. Mode-locking is obtained when the spectrum becomes broad suddenly and a pulsed signal appears on the scope. Fig. B-1 shows the spectrum of the ultra-short pulse laser when its FWHM bandwidth is 46 nm.

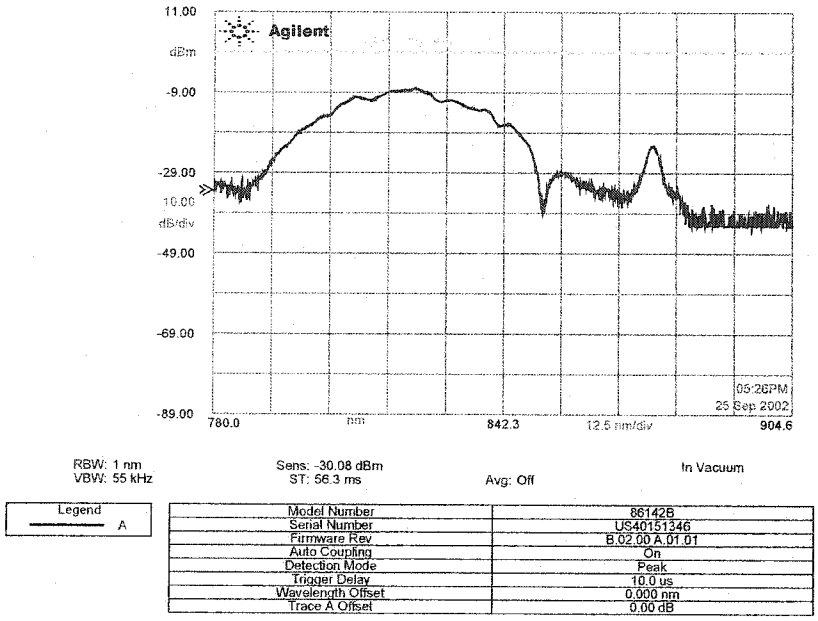


**Figure B-1** The spectrum of the ultra-short pulse laser

# APPENDIX C

## MEASUREMENT OF THE ULTRA-SHORT LASER PULSE

The duration of the laser pulse was measured by means of an autocorrelator (FR-103. Femtochrome). It utilizes a background–free (non-collinear) second harmonic generation (SHG) method for the measurement of the autocorrelation function of a repetitive ultra-short laser pulse. Fig. C-1 is the standard configuration of a Michelson interferometer-based autocorrelator. Direct the ultra-short pulse beam into the entrance. A beamsplitter divides it into two beams with one beam having a certain delay, T. The two beams recombine in a SHG nonlinear crystal where the second harmonic is generated only when the nonlinear crystal gets phase matched by angle tuning. The second harmonic is detected by the PMT. The intensity autocorrelation trace can be displayed via an oscilloscope. The FWHM autocorrelation trace width, t, is 110 fs as shown in Fig. C-2. According to the relationship between the autocorrelation trace width t and the pulse duration $\tau$ for laser pulse, the reduction factor is $\tau/t = 0.648$, assuming $sech^2$ of the pulse shape, the final received FWHM pulse duration $\tau = 71$ fs.

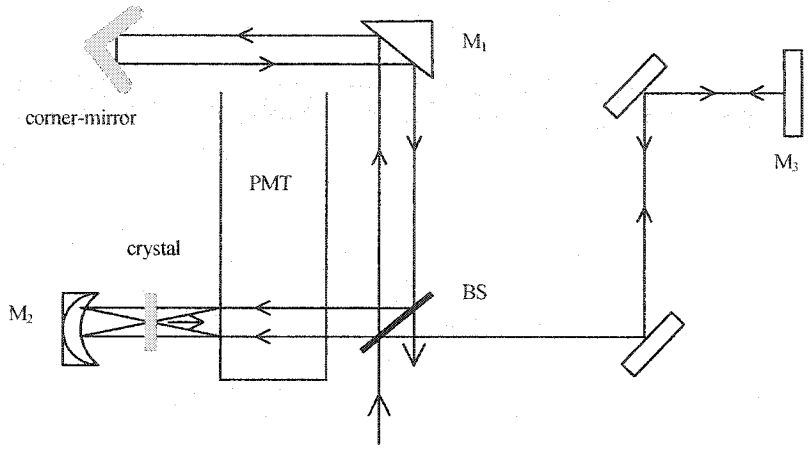


**Figure C-1** The optical schematic of the FR-103 autocorrelator

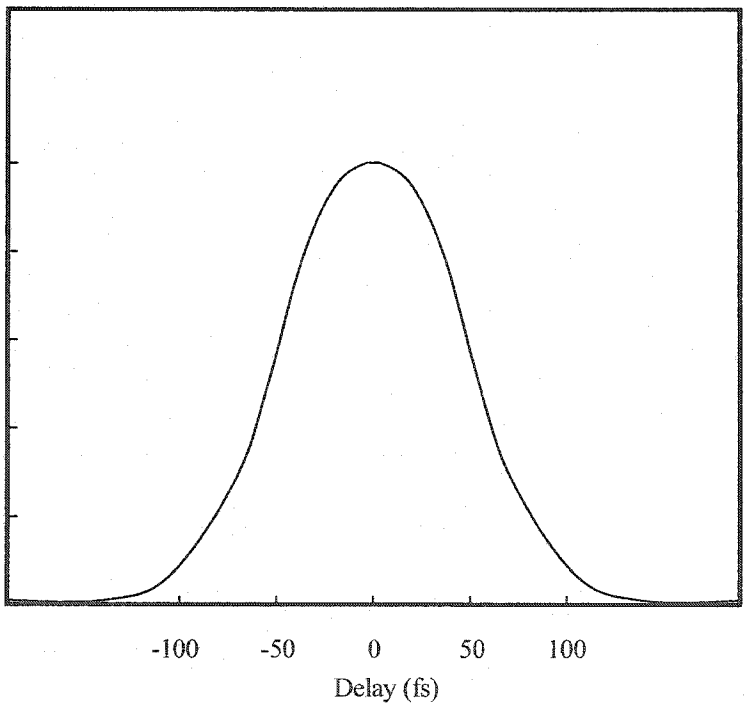


**Figure C-2** The autocorrelation trace of ultra-short pulse laser

# APPENDIX D

## THE ALIGNMENT PROCEDURE OF THE OCT SETUP

The interferometer must be aligned before it can be used. The alignment of an optical system must be done with great care. Moreover, some characteristics of this OCT layout have required special attention.

(1) The output of the SLD is invisible and also so weak that an infrared viewer cannot be used. The infrared detector card becomes the only tool to view the light during the alignment process. However, the light spot on the infrared card is so dim that the exact position of the beam is very difficult to find. This has caused some problems when aligning a reflector to retro-reflect the incident light beam.

(2) The interference signals appear only if the optical path length in each arm is equal to or within the source coherence length. This means that it will be visible only within a very small range (~10's μm), inside the scanning range of the reference mirror. If the system is not well aligned within this small range, there will be no clear evidence of interference no matter how well the system is aligned outside the ~10's μm range.

(3) Fig. D-1 (b) shows the interference fringe pattern received when the axis of the microscope objective is perfectly aligned with the axis of the sample arm. If these two axes are not very well aligned, the fields of view of the two arms will not overlap in their center. As a result, the received interference is no longer circles but curved lines instead, as shown in Fig. D-1 (a). The axes must be perfectly aligned.

To simplify the alignment process, the following alignment procedures are proposed. The first step is to set the collimated SLD output beam parallel to the optical table at the appropriate height. Make sure the beam distribution as Gaussian as possible. It is very helpful to use a red He-Ne laser beam in line with the SLD beam. All the other optical elements are then positioned and centered along the optical axis defined by the He-Ne laser beam.

The second step is to insert the beamsplitter (BS) cube into the path. The He-Ne laser beam goes through the center of the cube and is well retro-reflected by the front surface of the BS cube. The reference mirror and the sample mirror are put into position, and the same alignment procedure is repeated. Then in the detecting arm, block the beam with a white card at the far field and adjust the two reflected spots from the reference and sample arms separately, until they overlap on the card. Circular interference fringes must appear on the card.

The third step is to insert the microscope objective into the sample arm. The circular interference fringes disappear on the card because the sample beam spot position changes. Translate the position of the microscope objective, adjust its height and tilt angle until the circular fringes on the white card reappear. Scan the reference mirror slowly in the right direction while the interference fringes become larger. Adjust the reference mirror at the position where the circles are as large as possible. This position is where the path delay between the sample and reference beams is nearly matched. Fine adjustments of the mirrors and other optical elements are needed to make sure that the system has been perfectly aligned.

The fourth step is to put the photodetector in the center of the reference fringes. Replace the red He-Ne laser beam with the infrared SLD beam. Scan the reference mirror back and forth at a low speed while observing the output signal monitored on television. With a proper alignment, the initial interference signal will be observable.

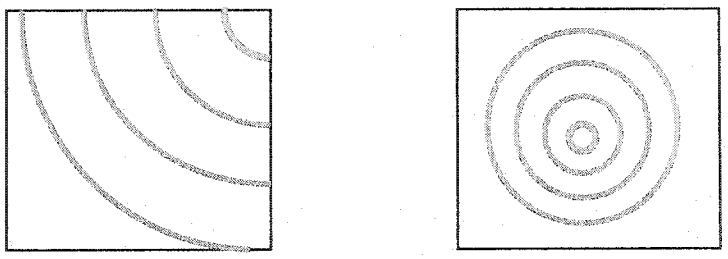

(a) (b)

**Figure D-1** The interference fringes

The fifth step is to align the reference mirror such that the reference signal reaches its maximum value. The photodetector is replaced with the infrared camera to monitor the interference fringes. The fringes can be seen on the screen clearly. Slightly turn the two quarter-wave plates until the fringes achieve maximum contrast.

Often, the initial fringes seen on the screen are not circular because the reference planes are at a slight angle. One must bring the center of the pattern into the center of the field of view. The final reference signal received on the screen should be as shown in Fig. D-1 (b).